UCLouvain

École polytechnique de Louvain

Dam-break over mobile bed: Determination of bed shear stress based on velocity profile measurements

Authors: **Henri GILMARD, Adlane LAC**
Supervisor: **Sandra SOARES FRAZAO**
Readers: **Miltiadis PAPALEXANDRIS, João SARAIVA ESTEVES PACHECO DE ALMEIDA**
Academic year 2019-2020
Civil Engineering

Abstract

Dam breaks are disasters that involve the release of large volumes of water and sediment downstream. Studying these phenomena is important to better predict the risks, the flood risk areas as well as the topographical consequences.
The final objective of this Master's thesis is to try to better characterize the shear stress of water on sediments, based on velocity profiles, which is linked to all these events.

A physical representation of this phenomenon is essential to understand these interactions between water and sediments. Thanks to the hydraulic laboratory (in the LEMSC) at our disposal, we were able to reproduce, on a reduced scale, a dam break on a moving bed made of coarse sand.

These experiments were recorded with a high-speed camera enabling the detection of the different interfaces like the free surface, the interface between clear water and upper limit of the mobile bed, and the interface between the mobile bed and the fixed bed. Once all these images were recorded, we used a non-intrusive technique called "Particle Image Velocimetry" (PIV) thanks to the software DaVis 8 (LaVision) in order to determine the velocity profiles of the flow for each time and at each position of the flume.

Two general methods were then used to calculate the shear stress, and then compared: the Clauser method, using the vertical profile of the horizontal velocity $u(z)$, and the Slope method, using the longitudinal profile of the average horizontal velocity $U(x)$.
The results of the Slope method were also compared with a numerical simulation free of experimental errors.

Following our experimental observations, we determined that a decisive part of the velocity profile in the portion which develops inside the moving sediment layer has a logarithmic shape and that these different methods leads to relevant results that are of the same order of magnitude.

Other prospects and ideas for future research are also proposed.

Remerciements

La réalisation de ce mémoire n'est pas uniquement le fruit du travail de deux personnes. Sans l'aide ni le soutien de certains intervenants, ce travail n'aurait pas été réalisable. Nous voulons donc remercier toutes ces personnes qui, de loin ou de près, y ont contribué.

Tout d'abord, nous tenons à souligner l'importante aide apportée, le temps précieux accordé, les nombreux conseils donnés ainsi que le soutien offert par notre promotrice Madame Sandra Soares-Frazão qui nous a permis de réaliser notre mémoire dans les conditions les plus agréables.

Nous désirons également remercier Samuel Laurent pour l'aide apportée concernant toutes les manipulations réalisées en laboratoire, malgré que celles-ci aient été quelque peu raccourcies suite aux restrictions dues au coronavirus.

Nous souhaitons remercier Robin Meurice pour sa collaboration et son aide sur certains aspects de notre mémoire, en particulier sur les simulations numériques. Nous lui partageons tout notre soutien pour la suite de son doctorat.

Donifan Camacho-Fernandes, Pauline Radelet et Ilaria Fent sont des acteurs indirects de notre travail. Nous aimerions les remercier pour les documents, les pistes à explorer et les données collectées qu'ils nous ont transmis par le biais de leur TFE et thèse réalisés durant les années précédentes.

Pour terminer, nous tenons à remercier nos amis et nos familles qui nous ont soutenus, encouragés et conseillés de manière continue tout au long de ce travail. Nous pensons particulièrement à Frédéric Gilmard et à Timothée Deschuyteneer qui nous ont tous les deux donné de précieux conseils.

List of symbols

A	Wet cross section area of a channel	[m^2]
B	Integral constant for the logarithmic profile of the velocity	[-]
B_r	Integral constant for rough boundaries	[-]
B_s	Integral constant for smooth boundaries	[-]
c_0	Dam-break wave celerity	[m/s]
c_b	Sediment concentration in the bed	[-]
d	Sediment diameter	[m]
D	Tube diameter of the flow	[m]
d_{50}	Median sediment diameter	[m]
d_x	Sediment diameter for which x is the percentage of finer grains	[m]
d_*	Sedimentological diameter	[-]
e	Relative gap between the local and the depth-averaged velocity	[-]
F_x	x-component of the force vector used in Newton's second law	[N]
Fr	Froude Number	[-]
g	Gravity acceleration in z-direction	[m/s^2]
h	Flow depth	[m]
H	Piezometric head	[m]
$\mathcal{H}$	Total head	[m]
h_0	Initial water depth upstream the gate	[m]
h^{ND}	Nondimensional water depth	[-]
k	Permeability	[m/s]
k_s	Equivalent bed roughness	[m]
m	Mass of a particle	[kg]
n	Manning coefficient	$[s/m^{1/3}]$
P	Wet perimeter	[m]
q	Discharge per unit width	[m^3/s/m]
R	Hydraulic radius	[m]
R_b	Bed hydraulic radius	[m]
Re	Reynolds number	[-]
Re_*	Sedimentological Reynolds number	[-]
s	Relative density	[-]
S_0	Bed slope	[-]
S_f	Friction slope	[-]
$S_{f,MOM}$	Friction slope calculated with the momentum equation	[-]
$S_{f,SG}$	Friction slope calculated with the Song and Graf equation	[-]
$S_{f,ML}$	Friction slope calculated with the ML model	[-]
$S_{f,SS}$	Friction slope calculated with the steep slope model	[-]
$S_{f,CH}$	Friction slope calculated with the Boussinesq's equation	[-]

$S_{f,Exp}$	Friction slope calculated with the experimental values	[-]
t	Time	[s]
t^{ND}	Nondimensional time	[-]
u	x-component of the velocity vector	[m/s]
U	Depth-averaged velocity in x-direction	[m/s]
u_*	Shear velocity	[m/s]
u'	Longitudinal velocity fluctuation in turbulent flow	[m/s]
$\bar{u}$	Time-average velocity in turbulent flow	[m/s]
u^{ND}	Nondimensional horizontal velocity	[-]
v	y-component of the velocity vector	[m/s]
V	Velocity vector	[m/s]
V_x	x-component of the velocity vector used in Newton's second law	[m/s]
w	z-component of the velocity vector	[m/s]
W	Wet density	[N/m^3]
w'	Vertical velocity fluctuation in turbulent flow	[m/s]
x	Longitudinal coordinate	[m]
x^{ND}	Nondimensional longitudinal coordinate	[-]
z	Vertical coordinate	[m]
z_0	Reference level	[m]
z_b	Bed elevation (generally corresponding to $z_{b,up}$)	[m]
$z_{b,low}$	Bed elevation of the non-moving sediments	[m]
$z_{b,up}$	Bed elevation of the upper moving sediments	[m]
z^{ND}	Nondimensional vertical coordinate	[-]
z_w	Water level	[m]
α	Coriolis coefficient	[-]
α_k	Empirical coefficient in the calculation of the bed roughness	[-]
Δz	Theoretical level from the fixed bed towards which the velocity logarithmic law goes asymptotically	[m]
δ	Thickness of the sheet flow layer	[m]
γ	Specific weight	[N/m^3]
γ_s	Sediment specific weight	[N/m^3]
ε_0	Bed porosity	[-]
$\varepsilon_1, \varepsilon_2$	Parameters in the Boussinesq model	[-]
θ	Shield's parameter	[-]
κ	Von Karman coefficient	[-]
μ	Water dynamic viscosity	[kg/m/s]
ν	Kinematic viscosity	[m^2/s]
ρ	Water density	[kg/m^2]
ρ_m	Depth averaged density of the water-sediment flow mixture	[kg/m^2]
ρ_s	Sediment density	[kg/m^2]
ρ_0	Bed density	[kg/m^2]
τ	Shear stress	[N/m^2]
τ_b	Bed shear stress	[N/m^2]
τ_*	Non-dimensional hear stress	[N/m^2]
φ	Internal angle of friction of the bed material	[°]

Contents

Introduction **7**
Master thesis interest 7
Motivation and goals 7
Overview 8

1 Theoretical Background **9**
1.1 Steady and unsteady flows 9
1.2 Depth-averaged equations for steady free surface flows 10
1.3 Influence of the bed heterogeneity 13
1.4 Laminar and turbulent flows 14
1.5 Sediment transport 17
1.6 Shallow-water equations coupled with Exner equation 20
1.7 Different ways to calculate τ 21
1.7.1 Clauser method 21
1.7.2 Slope method 22
1.7.3 Reynolds stress method 25

2 State of the art **27**
2.1 Velocity distribution in steady uniform flow over fixed bed 27
2.2 Velocity distribution in unsteady flow over fixed bed 29
2.3 Velocity distribution in steady flow over mobile bed 30
2.4 Velocity distribution in unsteady flow over mobile bed 33
2.5 Analytical velocity distribution for the dam-break over frictionless and fixed bed 33
2.6 Velocity distribution for the dam-break over mobile bed 37
2.6.1 Conclusion of the thesis of Ilaria Fent 37
2.6.2 Conclusion of the Master's thesis of Donifan Camacho & Pauline Radelet 40

3 Dam break experiment **43**
3.1 Experimental set-up 43

3.2 Instantaneous gate opening 48

4 Experimental data processing **50**
4.1 Detection of velocity by PIV 50
4.1.1 Principle 51
4.1.2 Calibration 52
4.1.3 Overlap 53
4.1.4 Calculation example 54
4.2 Determination of the water and bed surfaces 56
4.3 Repeatability of the experiments 58
4.4 Moving average 60

5 Results and analyses **62**
5.1 Investigation of the velocity profile found by Sumer et al. (1996) . . 62
5.2 Clauser method (using the $\Delta z - u_*$ relation proposed by Sumer et al.) 66
5.3 Clauser method (using parametric optimization) 69
5.4 Slope method 75
5.4.1 Determination of the hydraulic radius R 75
5.4.2 Experimental analysis of the friction slope S_f 76
5.4.3 Comparison with Ritter's analytical solution 80
5.4.4 Comparison with numerical simulations 81
5.4.5 Final results of the Slope method 86

Conclusion **89**

References **92**

Annexes **95**
Appendix A 95
Appendix B 97
Appendix C 101
Appendix D 103
Appendix E 105
Appendix F 107

Introduction

Master thesis interest

Dams are built to control the flow of rivers, to supply water and to produce hydropower energy. A dam failure is a pretty rare event these days but it is catastrophic as it can lead to the destruction of lands and communities downstream the collapsed structure following severe soil movements. This problem affects all continents: we can evoke the Brumadinho dam failure (Brazil), the Tiware dam breach (India) and the Spencer Dam failure (US) that all three occurred in 2019.

The final objective of our thesis is to improve the comprehension of the consequences of such a rupture. To better predict the morphological changes through the estimation of sediment transport, a preliminary step is to consider the shear stress generated by the velocity gradient in the flow on the sediment bed. This is what we focused on through the measurement of the velocity profile of a dam break flow. Using different methods, we computed the bed shear stress from the velocity profile.

Motivation and goals

Our Master's thesis is the continuation of two other theses: Ilara Fent's thesis "Dam break over mobile bed: Experimental and numerical study" (2018) and Donifan Camacho-Fernandes and Pauline Radelet's Master's thesis "Mesure du profil de vitesses dans un écoulement consécutif à une rupture de barrage sur lit de sédiments" (2019).
Our goal is to explore new ideas to improve the determination of the shear stress. We also wanted to enlarge the database of experiments but the lockdown related to the coronavirus outbreak stopped us but gave us more time for data analyses on the previous experiments. We introduce new analyses that we had the opportunity to test on numerical simulations.

Overview

In the first chapter, we give some theoretical reminders about the concepts that are useful in the case of a dam break and that we take for granted in our work.

In the second chapter, we make the state of the art: we mention the scientists who already worked on this subject or who brought results to experiments close to ours. We also discuss the conclusions brought by the thesis of Ilaria Fent and the Master's thesis of Donifan Camacho and Pauline Radelet.

In the third chapter, we present the dam-break experiment: the set-up, the studied parameters and the equipment.

The fourth chapter presents the way we process the experimental data. It goes from the detection of velocity by the Particle Image Velocity (PIV) to the moving average that we applied on the experimental data to smooth the data when necessary.

The real contribution of this thesis is presented in the fifth chapter, where we show the application of our different methods of analysis and our results. We also compare some of these results with numerical simulations.

We will conclude by taking a step back from our results and also by indicating some ideas for possible successors.

Chapter 1

Theoretical Background

In this chapter, we provide a reminder about some theoretical principles that will allow a better understanding of our master's thesis. This reminder relates to principles such as the comparison between steady and unsteady flows, the general equations for steady free-surface flows, the influence of the bed heterogeneity, the comparison between laminar and turbulent flows, the different kinds of sediment transport processes, the shallow-water equations coupled with the Exner equation and, finally, the different ways to calculate the bed shear stress τ_b.

Some sections of this chapter are largely inspired by the courses LGCIV2051 - Applied hydraulics open-channel flows, LGCIV2053 - Hydraulique Fluviale and LGCIV2054 - Numerical simulation of transient flows taught by Pr. Sandra Soares Frazao. We were also inspired by the Master's thesis made in 2019 by Donifan Camacho-Fernandes and Pauline Radelet and by the thesis made in 2018 by Ilaria Fent for which the topics were similar to the present Master's thesis.

1.1 Steady and unsteady flows

In the everyday life, we can meet steady flows and unsteady flows. A flow is said steady when its properties remain constant with time.

$$\mathbf{V}(x, y, z) = \begin{pmatrix} u \\ v \\ w \end{pmatrix} \neq f(t) \tag{1.1}$$

This concept is important because dam-break flows cause highly unsteady flows (as can be seen on samples of our experiments in figure 1.1) and we studied those by comparing them to better known steady flows.

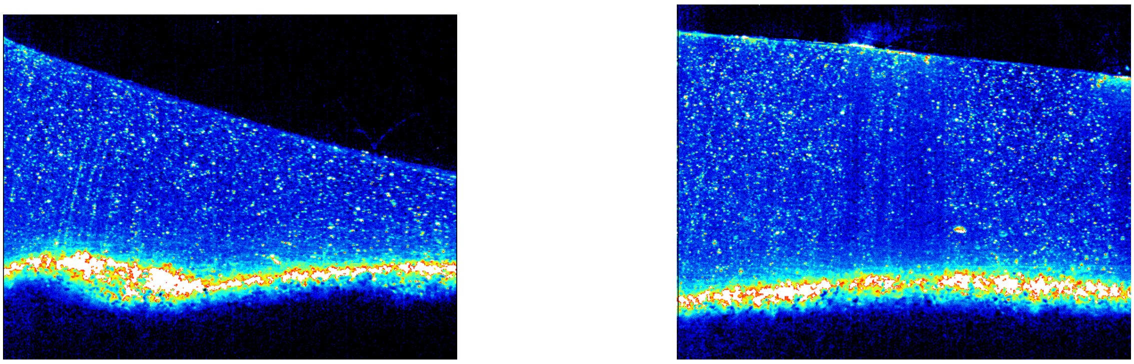

Figure 1.1: Typical pictures of the flow from our experiments at the interval position x = [0.08m 0.32m] - On the left: after 0.5 s - On the right: after 1 s

1.2 Depth-averaged equations for steady free surface flows

Let's introduce the depth-averaged equation for steady free surface flows.
The basic assumptions of steady free surface flows are:

- The flow only varies in one dimension (in the x-direction)
- The discharge does not vary with distance (continuity)
- The flow is parallel. This implies that the stream lines are parallel.

From Bernoulli's principle:

$$\mathcal{H} = \frac{\alpha U^2}{2g} + z + \frac{p}{\gamma} = constant \tag{1.2}$$

where $\mathcal{H}$ is the total head, α is the Coriolis coefficient that takes into account the variation of the velocity $u(z)$ around the depth-averaged velocity U, g is the free-fall acceleration (9.806 m/s^2), z is the elevation, p is the pressure and γ is the specific weight of water. Since the pressure is atmospheric in free surface flows, the pressure term can be omitted. Indeed, the total head $\mathcal{H}$ is not an absolute variable but a relative one because the water level z depends on the reference level. Since what matters to us is the variation of the total head, adding or subtracting a constant is not relevant.

The Coriolis coefficient α can be found using the following equation:

$$\alpha = 1 + \frac{\int (3e^2 + e^3) dA}{A} \tag{1.3}$$

where $e(z) = \frac{u(z)-U}{U}$, is a nondimensional difference between the velocity and the depth-averaged velocity, and A is the cross section of the flume.

Furthermore, the equation 1.2 can be adapted to include a friction term J_{12} that represents, in our case, friction due to the roughness of the bed:

$$\mathcal{H} = z_1 + \frac{\alpha_1 U_1^2}{2g} = z_2 + \frac{\alpha_2 U_2^2}{2g} + J_{12} \tag{1.4}$$

Each of these components is shown in figure 1.2.
Neglecting the losses and considering a steady flow, Bernoulli's principle can be written:

$$\frac{d\mathcal{H}}{dx} = 0 \tag{1.5}$$

Note that an unsteady flow would include an additional term (which was actually neglected in equation 1.5) to consider the transitory effects:

$$\frac{d\mathcal{H}}{dx} = \frac{1}{U}\frac{\partial H}{\partial t} \tag{1.6}$$

where we introduced the piezometric head while dropping the constant pressure term:

$$H = z + \cancel{p/\gamma} = z \tag{1.7}$$

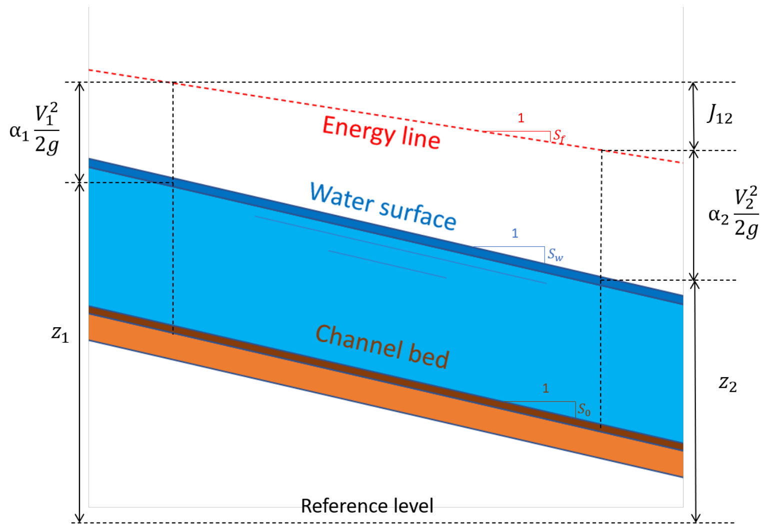

Figure 1.2: Bernoulli's principle in a general free surface channel
Reference: Adapted from LGCIV2051 - Applied hydraulics: open-channel flows

From here on, we will call the slopes of the channel bed, of the water surface and of the energy line respectively S_0, S_w and S_f, as shown in figure 1.2.

If we now imagine the section perpendicular to the direction of the flow, the general cross-section of a channel can be represented as follows:

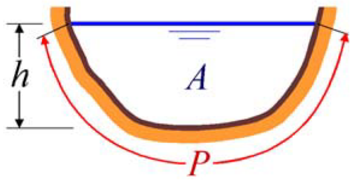

Figure 1.3: General representation of an irregular cross-section
Reference: LGCIV2051 - Applied hydraulics: open-channel flows
.

where A and P are respectively the cross-section area and the wet perimeter.
The hydraulic radius is defined by the relation:

$$R = \frac{A}{P} \tag{1.8}$$

Uniform flow

In the case of a uniform flow:

- The cross-section area of the channel A is constant.
- The water depth h is constant.
- The velocity U is constant.
- $S_0 = S_w = S_f$ (the 3 slopes are parallel)

The equilibrium of forces leads to the Chézy equation

$$U = C\sqrt{RS_0} \tag{1.9}$$

where C is a coefficient taking into account the effects of friction.

Manning suggested another form for this coefficient, directly dependent on the hydraulic radius:

$$C = \frac{1}{n}R^{\frac{1}{6}} \tag{1.10}$$

with n the Manning coefficient.

Combining equations 1.9 and 1.10, the Manning equation for a uniform flow is obtained:

$$U = \frac{1}{n} R^{2/3} S_0^{1/2} \tag{1.11}$$

Gradually varied flows

In other cases, flows are said gradually varied. It means that they are not uniform anymore and that the water depths and the velocities show a progressive evolution, but the velocity vectors of this type of flows can still be considered parallel.

In this situation, the three slopes are not equal anymore:

$$S_0 \neq S_w \neq S_f$$

The fundamental assumption of the gradually varied flow is that its friction loss in a cross-section is the same as the friction loss from a uniform flow with same discharge and depth.

The equation 1.11 can be adapted to this case by replacing the bottom slope S_0 by the friction slope S_f.

$$U = \frac{1}{n} R^{2/3} S_f^{1/2} \tag{1.12}$$

Mathematically speaking, S_f corresponds to opposite of the slope of the Energy line (since the hydraulic slope is expressed as the opposite of the mathematical slope):

$$S_f = -\frac{\partial \mathcal{H}}{\partial x} \tag{1.13}$$

Note that, in the case of unsteady flows:

$$S_f = -\frac{\partial \mathcal{H}}{\partial x} + \frac{1}{U}\frac{\partial H}{\partial t} \tag{1.14}$$

1.3 Influence of the bed heterogeneity

Generally, beds under natural flows are not simple and can be heterogeneous as illustrated in figure 1.4.

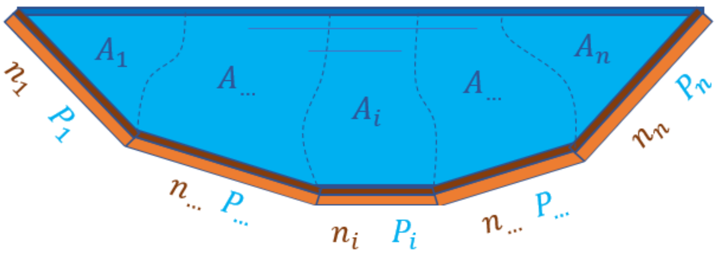

Figure 1.4: Cross section for a bed heterogeneity

If we divide the cross-section in different local fictive portions "i" and make the assumption that the average velocity is the same in each area ($U_1 = U_2 = U_i = U_n = U$), we have:

$$U = U_i = \frac{1}{n} R^{2/3} S_0^{1/2} = \frac{1}{n_i} R_i^{2/3} S_0^{1/2} \tag{1.15}$$

By isolating R_i, we obtain

$$R_i = R \left(\frac{n_i}{n} \right)^{3/2} \tag{1.16}$$

which represents the hydraulic radius specific to a local portion of the bed "i".

If we take the equation 1.15 with the definition $R = A/P$, and put this equation to the power of $3/2$, we have:

$$\frac{A}{n^{3/2} P} = \frac{A_i}{n_i^{3/2} P_i} = \frac{\overbrace{\sum A_i}^{=A}}{\sum n_i^{3/2} P_i} \tag{1.17}$$

By isolating n, we obtain :

$$n = \left(\frac{\sum n_i^{3/2} P_i}{P} \right)^{2/3} \tag{1.18}$$

which represents the equivalent Manning coefficient of the cross-section.

1.4 Laminar and turbulent flows

It's important to distinguish a laminar flow from a turbulent flow. In a laminar flow, adjacent particles at a given time stay adjacent with time. In hydraulic terms, it means that the stream lines are parallels. Particles of this kind of flow follow only one direction: the axis of the channel in which they flow.

The velocity profile of a laminar flow follows a parabolic distribution as we can see in figure 1.5, and the shear stress profile follows a linear law.

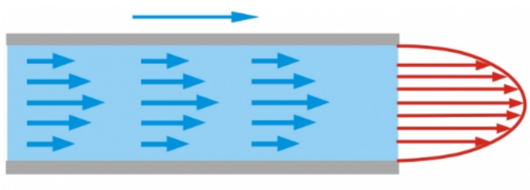

Figure 1.5: Velocity profile of a laminar flow - Reference: www.gunt.de

Obviously, it's easier to work with laminar flows than turbulent ones thanks to their more expectable behavior.

Indeed, when the flow becomes turbulent, the trend of its displacement stays parallel to the wall but fluctuations u' appears accompanied by vortex that disturbs the velocity profile ($u = \bar{u} + u'$).

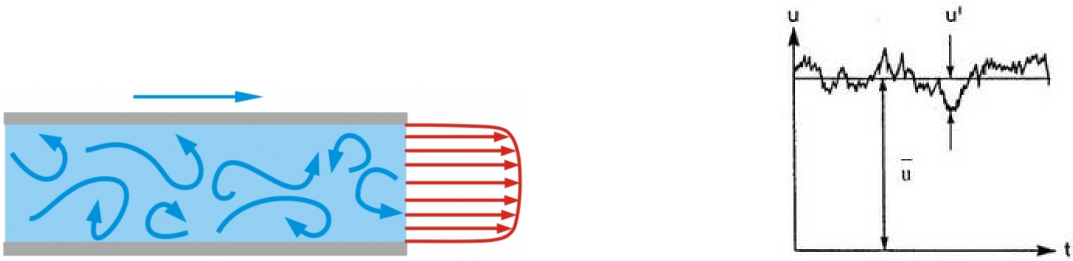

Figure 1.6: Velocity profile of a turbulent flow and fluctuation term
Reference : www.gunt.de

In order to determine the laminar or turbulent behavior of a flow (or the transition region), we use the important non-dimensional Reynolds number.

$$Re = \frac{UD}{\nu} = \frac{\rho UD}{\mu} \tag{1.19}$$

Where U is the depth-averaged velocity in the x-direction at a certain x-position. D is the tube diameter of the flow (in the case of our experiments we use a $D_{equivalent}$ that corresponds to the water height). ν is the kinematic viscosity of the fluid. ρ is the density and μ is the dynamic viscosity of the fluid.

The Moody diagram (figure 1.7) shows us that for a small Reynolds number

($Re < 2000$), the flow is laminar. For higher values of the Reynolds number ($Re > 3000$), the flow is turbulent. For intermediate values ($2000 < Re < 3000$) the flow is a transitional flow.

In order to determine the behavior of our experiments, we calculated the Reynolds number at the section $x = 0$ (position of the dam) and after a relatively long time $t = 5$ seconds. The average velocity U at that position and time is 0.4650 m/s and the water level is 0.126 m over the bed ($D_{equivalent}$) so we are in a case of a turbulent flow with $Re = 58590 \gg 3000$. So we can assume that we are in the presence of a turbulent flow for our experimental analyses.

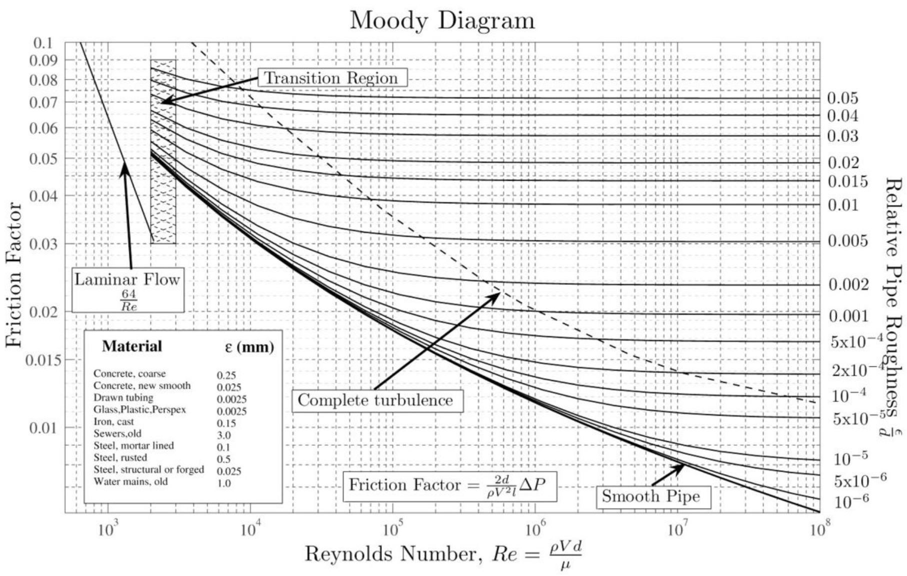

Figure 1.7: Moody diagram - Reference : S. Beck & R. Collins, 2008

A turbulent flow can be distinguished in two types if the flow is on a smooth or on a rough wall. To determine that type, we introduce another non-dimensional number: the sedimentological Reynolds number

$$Re_* = \frac{u_* k_s}{\nu} \tag{1.20}$$

Where u_* is the shear velocity, k_s is the equivalent bed roughness and ν is the kinematic viscosity. The equivalent bed roughness is itself related to a specific sediment diameter d_x (commonly accounted as d_{50}) and to an empirical coefficient α_k that can vary from 1 to 6.60 (Garcia, 2008):

$$k_s = \alpha_k d_x \tag{1.21}$$

If $Re_* < 11.6$, the flow is hydraulically smooth and if $Re_* > 11.6$, the flow is hydraulically rough.

In the case of our experiments, we found $Re_* = 154.8 \gg 11.6$ for the worst case considering the lowest shear velocity $u_* = 0.045\ m/s$ that we obtained at time 0.7 s located 50 cm downstream the dam (the development of this value is explained later in detail in chapter 5 and the sediment characteristics are expressed in table 1.1). It means that our analyses will focus on the case of a rough turbulent flow.

Characteristic of the sand	Symbol	Value
Density	ρ_s	2682 kg/m^2
Median diameter	d_{50}	1.72 mm
Diameter at 10%	d_{10}	1.15mm
Uniformity coefficient	d_{60}/d_{10}	1.8/1.3=1.38
Porosity (void volume fraction)	ε_0	0.42
Bed concentration	c_0	0.58
Friction angle	φ	38°
Permeability	k	2.27 10^{-2}m/s
Dry volumetric weight	W	14.54 kN/m^3

Table 1.1: Sediment characteristics of our experiments

1.5 Sediment transport

While a fluid flows over a sediment bed, erosion phenomena can occur. Sediments can be transported by the flow in two ways: by suspension or by bed-load.

The suspension transport occurs for lighter particles while the bed-load transport occurs for heavier particles for which the sediments move by rolling, sliding or saltating (small successive rebounds) as shown in figure 1.8.

The way to know if this kind of transport occurs or not is based on the Shields diagram (which was then readjusted by Van-Rijn in 1984) (figure 1.9). This diagram makes a relation between the non-dimensional shear stress τ_* and the sedimentological diameter d_*. The area above the red curve corresponds to a flow with sediment transport, while the area below that curve corresponds to a flow without sediment transport.

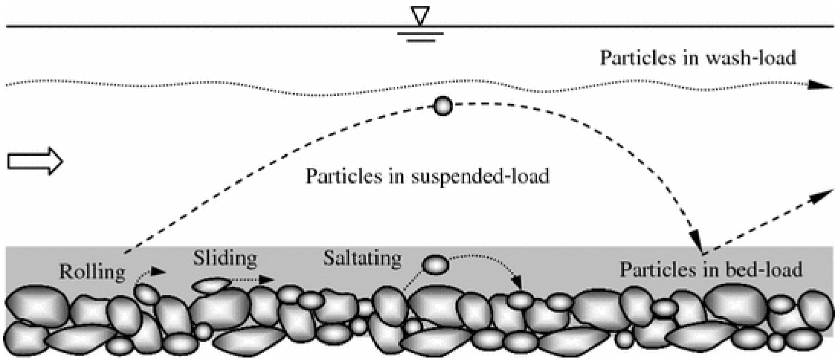

Figure 1.8: Different ways of sediment transport
Reference: Adapted from LGCIV2053 - Hydraulique Fluviale

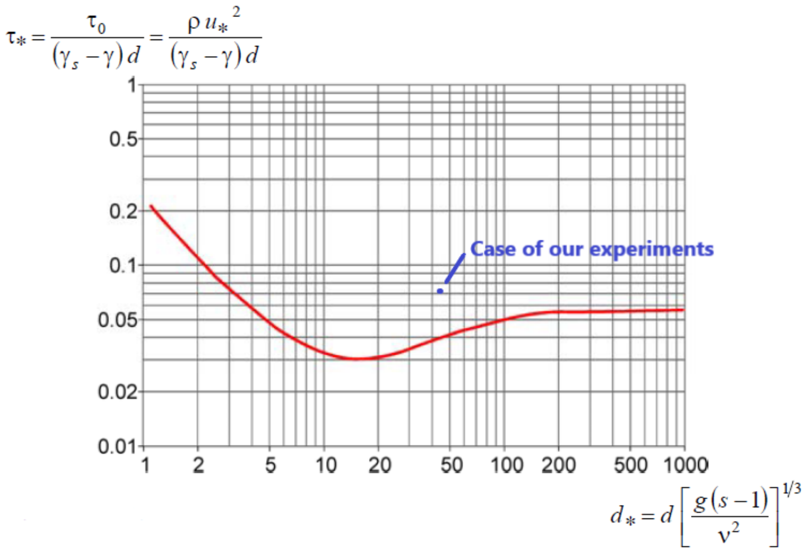

Figure 1.9: Shields - Van-Rijn diagram
Reference: Adapted from LGCIV2053 - Hydraulique Fluviale

To make a link between this diagram and the Moody diagram (figure 1.7) about the laminar or turbulent behavior of the flow, we can observe that :

- When $d_* < 4$ (left part of the diagram), particles are in a laminar flow and figure 1.9 shows that τ_* is inversely proportional to d_*. It gives that $\tau_* = \frac{\tau_b}{(\gamma_s - \gamma) d_{50}} \propto \frac{1}{d_{50}} (\frac{\nu^2}{(s-1)g})^{1/3} = \frac{1}{d_*}$ where we can simplify both sides by $\frac{1}{d_{50}}$ and then, in laminar flows, sediment transport is independent of the sediment diameter but only on the kinematic viscosity ν. It results from the above that the transport in that kind of flow is the consequence of a group phenomenon. Note that γ_s is the specific weight of the sediments, γ is the specific weight of water, and $s = \frac{\gamma_s}{\gamma}$.

- When $d_* > 150$ (on the right of the diagram), particles are in a turbulent flow and figure 1.9 shows that τ_* becomes constant and independent from d_*. It results from the above that transport in a turbulent flow only depends on bed shear stress τ_b and on sediments characteristics (because $\tau_* = \frac{\tau_b}{(\gamma_s - \gamma) d_{50}}$).
- When $4 < d_* < 150$, particles are in a transition phase.

In the case of our experiments, the lowest value of τ_* we found (with the lowest $u_* = 0.045\ m/s$) is $\tau_* = 0.071$ and its corresponding sedimentological diameter $d_* = 43.79$. This point $(43.79; 0.071)$ is located in the above part of the diagram, meaning that sediment transport actually occurs. The characteristics of the sand we used can be found in table 1.1.

In 2008, Garcia proposed a variation of the Shields diagram (figure 1.10) where we can determine the kind of sediment transport (suspension or bed-load).

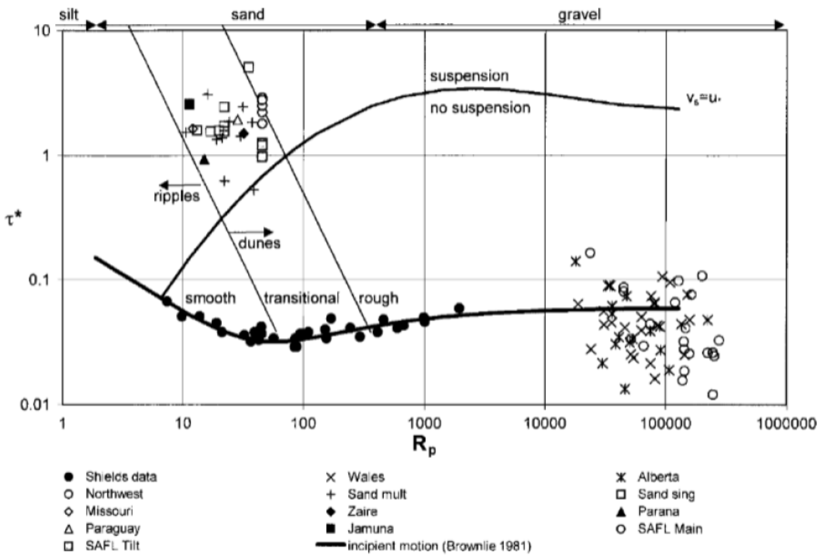

Figure 1.10: Shields diagram from Garcia's letter (2008)

Where $R_p = \frac{\sqrt{g(s-1)}d^{3/2}}{\nu}$ and $\tau_* = \frac{\tau_b}{(\gamma_s - \gamma) d_{50}}$.

Other formulas were determined in order to know if a flow allows a suspension or a bed-load transport. For example Sumer et al. (1996) proposed : If $\frac{w_s}{u_*} \geq 0.8$ to 1.0 then a bed-load transport occurs. Where u_* is the shear velocity and w_s is the falling velocity of the sediment for which Van Rijn gave a value of $w_s = 1.1\sqrt{sgd}$.

1.6 Shallow-water equations coupled with Exner equation

Shallow-water equations are the basis of the numerical simulation we use in the comparison with our experimental data. They are also the equations that Ritter solved to propose his analytical solution, which we will present later.
For these reasons, we will not go into details but we consider it necessary to at least introduce these equations.

The basic assumptions of the shallow-water equations are:

- The density ρ of the fluid is constant (incompressibility).
- The bed slope is small enough to be able to measure the water depth $h = z_w - z_b$ vertically.
- The pressure distribution is hydrostatic and an average velocity U can be defined as $U = Q/A$ where Q is the discharge and A the cross-section area.
- A Manning-type formula, normally used in uniform flow conditions, can be used to express the friction slope S_f. This is a rather simplified approach of the turbulence generated along the walls.

Basically, the shallow-water equations are two equations: the continuity equation and the momentum equation, found respectively by expressing the conservation of mass

$$\frac{Dm}{Dt} = 0 \tag{1.22}$$

and the x-component of Newton's second law for a system

$$F_x = \frac{D(mV_x)}{Dt} = \frac{D(mu)}{Dt} \tag{1.23}$$

The conservative form of the shallow-water equations on a rectangular prismatic channel is given by:

$$\frac{\partial h}{\partial t} + \frac{\partial q}{\partial x} = 0 \tag{1.24}$$

$$\frac{\partial q}{\partial t} + \frac{\partial}{\partial x}(\frac{q^2}{h} + g\frac{h^2}{2}) = gh(S_0 - S_f) \tag{1.25}$$

where q is the unit discharge passing through the section.

Next, it is possible to include the impact of the presence of sediments and to ensure the mass conservation of these sediments with the Exner equation:

$$\frac{\partial z_b}{\partial t} + \frac{1}{1-\varepsilon_0}\frac{\partial q_s}{\partial x} = 0 \tag{1.26}$$

where z_b is the bed elevation, ε_0 is the bed porosity, q_s is the unit-width sediment discharge that has to be estimated in parallel through another equation like the Meyer-Peter and Müller (MPM) formulation, for example.

1.7 Different ways to calculate τ

As seen in section 1.5, the estimation of the bed shear stress τ_b is required to predict if the sediment transport is likely to happen or not.

There are several ways to estimate the bed shear stress in the literature.

1.7.1 Clauser method

This method consists basically in an analogy with the logarithmic part of the velocity distribution of a steady flow over mobile bed. This type of flow will be introduced in more details in subsection 2.3. The goal of this method is to find the best values Δz, u_* and B_r to fit the experimental data velocity and the following logarithmic law found by Sumer et al. (1996):

$$\frac{u}{u_*} = \frac{1}{\kappa}\ln\left(\frac{z-\Delta z}{k_s}\right) + B_r \tag{1.27}$$

where $\kappa = 0.4$ is the Von Karman constant, k_s is a fixed parameter corresponding to the equivalent bed roughness, B_r is an integral constant for rough boundaries which varies all along the flow, Δz is the theoretical level from the fixed bed towards which the velocity logarithmic law goes asymptotically, and u_* is defined as the shear velocity, in such a way that:

$$\tau_b = \rho u_*^2 \tag{1.28}$$

Equation 1.27 corresponds to the logarithmic part of the velocity profile, so it is necessary to find the points that actually fit on this part in order to determine the value of u_* that we can then include in equation 1.28 to find the value of τ_b.

Equally, Ferreira et al. (2012) used the differential form of the logarithmic profile:

$$u_*\Big(\frac{d\{u\}}{dz}\Big)^{-1} = \kappa(z - \Delta z) \tag{1.29}$$

This form can be more convenient for the optimization of u_* and Δz as it does not require the estimation of k_s and B_r and it can be easier to optimize than a logarithm. Yet, it requires the numerical estimation of $\frac{d\{u\}}{dz}$.

1.7.2 Slope method

The bed shear stress is obtained by equilibrium of friction shear forces and gravity along the direction of flow (cf. figure 1.11):

$$\tau_b P dx = \gamma A S_0 dx \tag{1.30}$$

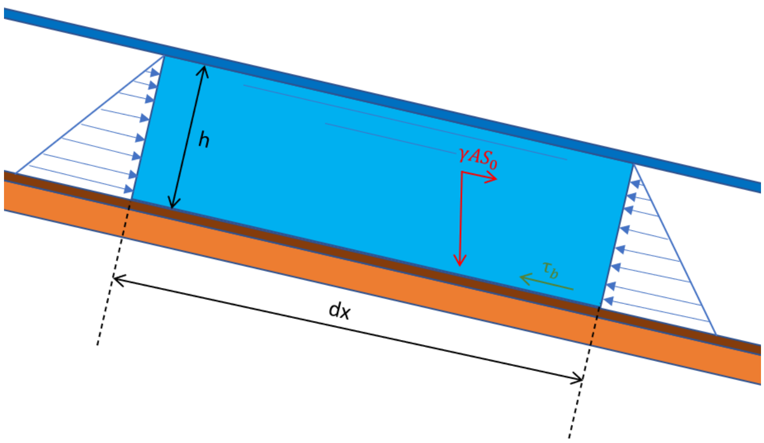

Figure 1.11: Flow with the different forces applied on the control volume
Reference: Adapted from LGCIV2053 - Hydraulique Fluviale

that leads to :

$$\tau_b = \gamma R S_0 \tag{1.31}$$

This can be generalized for non-uniform flows:

$$\tau_b = \gamma R S_f \tag{1.32}$$

where $\gamma = 9810 N/m^3$, where R is the hydraulic radius and where S_f is the friction slope.

There are several ways to estimate the friction slope S_f from experimental data:

- Based on Manning: using equation 1.12, we can find an equation for S_f:

$$S_{f,Manning} = U^2 n^2 R^{-4/3} \tag{1.33}$$

- As seen in section 1.2, there are two methods based on the definition of the total head (equation 1.4)

$$S_{f,steady} = -\frac{\partial \mathcal{H}}{\partial x} \tag{1.34}$$

$$S_{f,unsteady} = -\frac{\partial \mathcal{H}}{\partial x} + \frac{1}{U}\frac{\partial H}{\partial t} \tag{1.35}$$

- Ilaria Fent (2018) also listed several methods based on the shallow-water equations (equations 1.24 and 1.25)

  Clear water layer model: $S_{f,MOM}$ is directly obtained from the momentum equation (equation 1.25), remembering that

$$S_0 = -\frac{\partial z_b}{\partial x} = -\frac{\partial (z_w - h)}{\partial x} = \frac{\partial h}{\partial x} - \frac{\partial z_w}{\partial x} \tag{1.36}$$

$$S_{f,MOM} = -\frac{1}{gh}\frac{\partial q}{\partial t} - \frac{U^2}{gh}\frac{\partial h}{\partial x} - 2\frac{U}{g}\frac{\partial U}{\partial x} - \frac{\partial z_w}{\partial x} \tag{1.37}$$

  Remembering that the unit discharge q can be developed as $q = Uh$, and replacing equation 1.24 in equation 1.25, Song and Graf (1996) proposed a second method:

$$S_{f,SG} = -\frac{1}{gh}\frac{\partial q}{\partial t} + 2\frac{U}{gh}\frac{\partial h}{\partial t} + \frac{U^2}{gh}\frac{\partial h}{\partial x} - \frac{\partial z_w}{\partial x} \tag{1.38}$$

  Mixture layer model: Cao et al. (2004) tried to represent flows involving sediment transport and morphological evolution of the bed. The equations look like a variation of the combination of the shallow water equations 1.24 and 1.25, and the Exner equation 1.26:

$$\frac{\partial z_w}{\partial t} + \frac{\partial q}{\partial x} = 0 \tag{1.39}$$

$$\frac{\partial q}{\partial t} + \frac{\partial}{\partial x}\Big(\frac{q^2}{h} + g\frac{h^2}{2}\Big) = gh\Big(S_0 - S_f\Big) - \frac{1}{2}\frac{\rho_s - \rho}{\rho_m} gh^2 \frac{\partial C}{\partial x} + \Big(\frac{\rho_0}{\rho_m} - 1\Big) u \frac{\partial z_b}{\partial t} \tag{1.40}$$

where ρ is the water density, C is the sediment concentration within the fluid, ρ_0 is the bed density, ρ_s is the sediments density and ρ_m is the depth averaged density of the water-sediment flow mixture.

$$\frac{\partial z_b}{\partial t} = \frac{E - D}{1 - \varepsilon_0} \tag{1.41}$$

where E and D are respectively the erosion and deposition rate of sediments.

In our case, the density and the concentration variations in the flow can be assumed to be negligible, because sediment transport occurs only by bed load. This allows to neglect the last two terms in equation 1.40. We can then obtain the friction slope by combining equations 1.39 and 1.40:

$$S_{f,ML} = -\frac{1}{gh}\frac{\partial q}{\partial t} + 2\frac{U}{gh}\frac{\partial z_w}{\partial t} + \frac{U^2}{gh}\frac{\partial h}{\partial x} - \frac{\partial z_w}{\partial x} \tag{1.42}$$

Clear-water layer model over steep slope: Savage and Hutter (1989) proposed another formulation for the clear-water layer shallow-water model, taking into account the topography of the terrain. Juez et al. (2013) simplified the model, still accounting for gravity forces acting on the pressure terms:

$$\frac{\partial h}{\partial t} + \frac{\partial q}{\partial x} = 0 \tag{1.43}$$

$$\frac{\partial q}{\partial t} + \frac{\partial}{\partial x}\left(\frac{q^2}{h} + g\frac{h^2}{2}\cos^2\alpha\right) = gh\left(S_0\cos^2\alpha - S_f\right) \tag{1.44}$$

where α is the slope angle of the bottom, so that $\cos^2\alpha = \frac{1}{\tan^2\alpha+1} = \frac{1}{(\frac{\partial z_b}{\partial x})^2+1}$. The friction slope is then easily found:

$$\begin{aligned} S_{f,SS} = -\frac{1}{gh}\Bigg[&\frac{\partial q}{\partial t} + 2Uh\frac{\partial U}{\partial x} + U^2\frac{\partial h}{\partial x} + gh\frac{\partial z_w}{\partial x}\left(\left(\frac{\partial z_b}{\partial x}\right)^2 + 1\right)^{-1} \\ &-gh^2\frac{\partial z_b}{\partial x}\frac{\partial^2 z_b}{\partial x^2}\left(\left(\frac{\partial z_b}{\partial x}\right)^2 + 1\right)^{-2}\Bigg] \end{aligned} \tag{1.45}$$

Boussinesq Model: Castro and Hager (2013) proposed a variation of the shallow water equations for unsteady Boussinesq-type flows for a movable bed:

$$\frac{\partial h}{\partial t} + \frac{\partial q}{\partial x} = 0 \tag{1.46}$$

$$\frac{\partial q}{\partial t}+\frac{\partial}{\partial x}\left(\frac{q^2}{h}+g\frac{h^2}{2}+\frac{q^2}{h}\Big(\frac{\varepsilon_1}{2}+\frac{\varepsilon_2}{3}\Big)\right) = gh(S_0-S_f)+\frac{1}{2}S_0\Big(\frac{q}{h}\Big)^2(2\varepsilon_1+\varepsilon_2) \quad (1.47)$$

where ε_1 and ε_1 are defined in Castro and Hager (2013) and represent respectively the bed effects due to its deformation in time and space and the free surface profile effects:

$$\begin{aligned}\varepsilon_1 = &\frac{h}{U^2}\frac{\partial^2 z_b}{\partial t^2} - \frac{1}{U^2}\frac{\partial h}{\partial t}\frac{\partial z_b}{\partial x} + \frac{h}{U^2}\frac{\partial U}{\partial t}\frac{\partial z_b}{\partial x} + \frac{h}{U}\left(\frac{\partial^2 z_b}{\partial x \partial t} - \frac{1}{h}\frac{\partial h}{\partial x}\frac{\partial zb}{\partial t}\right)\\ &+\frac{h}{U}\frac{\partial^2 z_b}{\partial t \partial x} - \frac{1}{U}\frac{\partial h}{\partial t}\frac{\partial z_b}{\partial x} + h\left(\frac{\partial^2 z_b}{\partial x^2} - \frac{1}{h}\frac{\partial h}{\partial x}\frac{\partial z_b}{\partial x}\right) - \frac{h}{U^2}\frac{\partial z_b}{\partial t}\frac{\partial U}{\partial x}\end{aligned} \quad (1.48)$$

$$\begin{aligned}\varepsilon_2 = &\frac{h}{U^2}\frac{\partial^2 h}{\partial t^2} - \frac{1}{U^2}\left(\frac{\partial h}{\partial t}\right)^2 + \frac{h}{U^2}\frac{\partial U}{\partial t}\frac{\partial h}{\partial x} + \frac{h}{U}\left(\frac{\partial^2 h}{\partial x \partial t} - \frac{1}{h}\frac{\partial h}{\partial x}\frac{\partial h}{\partial t}\right)\\ &+\frac{h}{U}\frac{\partial^2 h}{\partial t \partial x} - \frac{1}{U}\frac{\partial h}{\partial t}\frac{\partial h}{\partial x} + h\left(\frac{\partial^2 h}{\partial x^2} - \frac{1}{h}\left(\frac{\partial h}{\partial x}\right)^2\right) - \frac{h}{U^2}\frac{\partial h}{\partial t}\frac{\partial U}{\partial x}\end{aligned} \quad (1.49)$$

The friction slope in this case is found:

$$\begin{aligned}S_{f,CH} = -\frac{1}{gh}\Bigg[&\frac{\partial q}{\partial t} + 2Uh\frac{\partial U}{\partial x} + U^2\frac{\partial h}{\partial x} + gh\frac{\partial z_w}{\partial x} + 2Uh\left(\frac{\varepsilon_1}{2}+\frac{\varepsilon_2}{3}\right)\frac{\partial U}{\partial x}\\ &+U^2\left(\frac{\varepsilon_1}{2}+\frac{\varepsilon_2}{3}\right)\frac{\partial h}{\partial x} + U^2 h\left(\frac{1}{2}\frac{\partial \varepsilon_1}{\partial x} + \frac{1}{3}\frac{\partial \varepsilon_2}{\partial x}\right) + \frac{1}{2}U^2(2\varepsilon_1+\varepsilon_2)\frac{\partial z_b}{\partial x}\Bigg]\end{aligned} \quad (1.50)$$

1.7.3 Reynolds stress method

The shear stress can be separated into a laminar component and a turbulent component. The laminar component τ_{lam} can be calculated using the vertical variation of the horizontal component of the velocity and the turbulent component τ_{turb} is determined after the application of the time average for the turbulent components of velocity :

$$\tau = \tau_{lam} + \tau_{turb} = \mu\frac{\partial u}{\partial z} - \rho\overline{u'w'} \quad (1.51)$$

where μ is the fluid dynamic viscosity, $\bar{\cdot}$ stands for time-average and u' and w' are longitudinal and vertical velocity fluctuations.

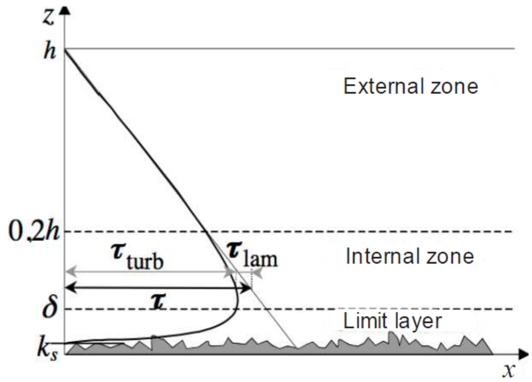

Figure 1.12: Turbulent and laminar components of shear stresses for a steady turbulent flow (Yalin 1977) - Reference : Thesis of Ilaria Fent, 2018

This method is typically used for uniform flows. Because of the high unsteadiness of our flow it can be difficult to distinguish between fluctuations related to turbulent effects and those related to experimental uncertainties.

If we pay attention to each of these methods, we can see that $\tau_b = f(u)$ is a function of the velocity. It is the reason why it is essential to analyse the velocity profile as we see in the next chapter.

Chapter 2

State of the art

Before starting to analyze our experiment velocity profile, it is interesting to know what kinds of velocity profiles the different authors found for different kinds of flows.

Indeed, in the everyday life, we can find different conditions of flow. Some of them are explained in this chapter. The velocity profile of a flow is what characterizes it. For the different kinds of flows, different velocity profiles have been found with a particular attention about the horizontal velocity profile u. This part of the chapter has already been performed by Ilaria Fent in her thesis made in 2018. It's the reason why some sections are largely inspired by her thesis.

In the case of dam break flows over mobile bed, which are highly unsteady flows, no precise velocity profile is known. Our study aims to determine a new empirical method to define one by making comparisons with methods described in this chapter.

Another part of this chapter is dedicated to the conclusions found in the previous thesis made by Ilaria Fent in 2018 and in the Master's thesis made by Donifan Camacho and Pauline Radelet in 2019. As a reminder, they also made their theses about velocity profiles for dam-break flows over mobile bed experiments and the experiments were realized in the same flume as ours, which is located at the LEMSC laboratory of UCLouvain.

2.1 Velocity distribution in steady uniform flow over fixed bed

In 1933, Nikuradse made numerous experiments in steady flow conditions in circular pipes inside which the walls were covered with sand of a known grain size glued on. The diameter of these sand grains being defined as the Nikuradse's equivalent sand roughness k_s. Combining his experiments with the experiments of Keulegan (1938) in a flume with steady uniform flow, a logarithmic velocity distribution was observed.

Indeed, for hydraulically smooth boundaries, the flow profile is linear near the wall (equation 2.1), while it is logarithmic above a certain level (equation 2.2).

$$\frac{u}{u_*} = \frac{u_* z}{\nu} \tag{2.1}$$

$$\frac{u}{u_*} = \frac{1}{\kappa}\ln(\frac{u_* z}{\nu}) + B_s \tag{2.2}$$

Where u_* is the friction velocity, z is the distance from the fixed bottom, ν is the kinematic viscosity of water, $\kappa = 0.4$ is the Von Karman constant and B_s is the integral constant for smooth boundaries, equal to 5.50 from Nikuradse experiments.

For hydraulically rough boundaries, the velocity profile is directly logarithmic because of the wall irregularities that break down the laminar layer :

$$\frac{u}{u_*} = \frac{1}{\kappa}\ln(\frac{z + z_0}{k_s}) + B_r \tag{2.3}$$

where z_0 is a reference level and B_r is the integral constant for rough boundaries. If the wall is completely rough, then the constant $B_r = 8.5$ for $z_0 = 0$, according to Nikuradse results.

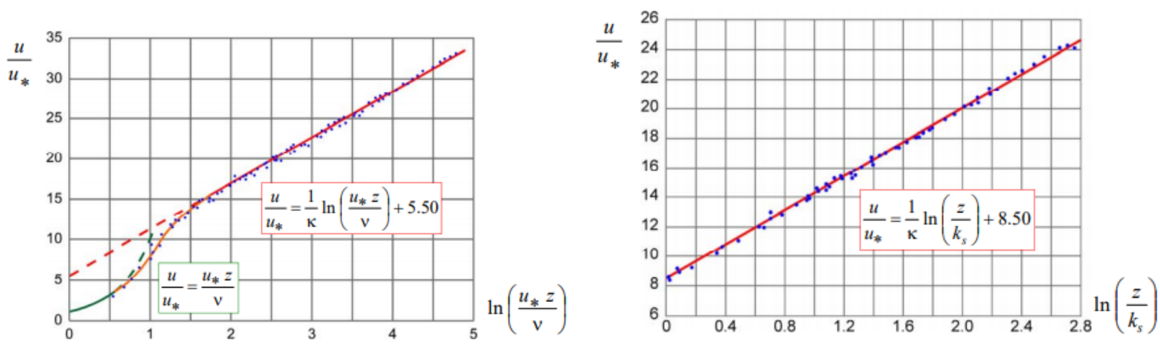

Figure 2.1: Velocity profile (Nikuradse, 1933) for smooth pipes (on the left) and for rough pipes (on the right) - Reference : LGCIV2053 - Hydraulique Fluviale

It's interesting to know that for free surface flows, a wake effect (described by Coles, 1956) affects the region close to the free-surface. It is not shown in figure 2.1 which is based on experiments in pipe flows.

The inner region, where the log-law is valid, is often limited to the relative value $z/h < 0.2$, determined by Graf an Altinakar (1988).

2.2 Velocity distribution in unsteady flow over fixed bed

Thanks to imagery techniques such as PIV and PTV, non-intrusive velocity measurements, it is now possible to investigate the velocity distribution also in unsteady flows.

In 1991, Tu carried out 13 tests in unsteady flows in a inclined fixed-gravel flume with 3 different kinds of gravels. In his analysis, the velocity distribution was slightly different in the rising part of the hydrograph than in the falling part, but the log-law velocity profile (equation 2.3) was still valid in the inner region (figure 2.2).

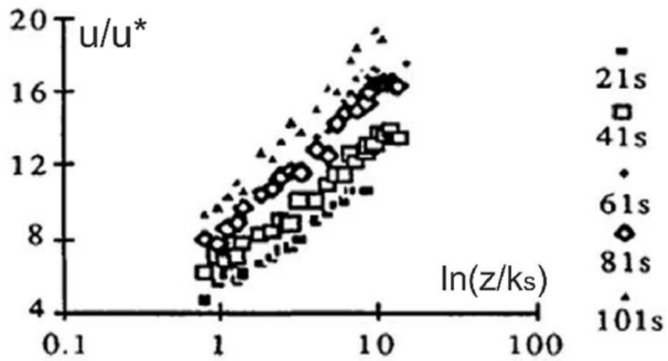

Figure 2.2: Logarithmic velocity profile in unsteady flow over fixed bed
Reference : PhD thesis of Tu, 1991

In 1992, Tu and Graf found that the log-law was also present in the inner region but with a constant B_r varying between 3.8 and 14.5.

In 1996, Song and Graf carried out experiments in unsteady flows over fixed bed in a tilting flume with water and a sediments recirculation mechanism. As can be seen in figure 2.3, the log-law was still valid but with some parameters adaptations : they gave the roughness directly as $k_s = d_{50}$ and the Von Karman constant $\kappa = 0.40$, they readjusted the gravel bed reference to $z_0 = 0.25k_s$ and the constant B_r was in the range of $8.5 \pm 15\%$.

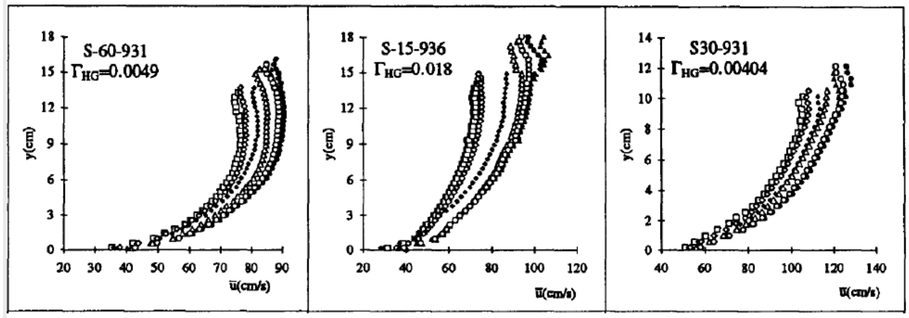

Figure 2.3: Logarithmic velocity profile in unsteady flow over fixed bed
Reference : Article of Song and Graf, 1996

2.3 Velocity distribution in steady flow over mobile bed

For this kind of flows, Sumer et al. (1996) carried out experiments with water and a sediments recirculation mechanism. The flume was 10 meters long, 0.3 meter large and 0.3 meter deep. They carried out the experiment 158 times with 4 different sizes of sediments and the water surface was smoothed by a rigid lid.

They aimed to study the velocity profile in the layer where the sediment transport takes place, called the "sheet-flow layer".

Based on the experimental velocity profile, Sumer et al. observed that a log-law clearly appears in the upper part of the sheet-flow layer and continues in the lower part of the clear water (cf. figure 2.5). This log-law was similar to equation 2.3 but with a modified definition of z :

$$\frac{u}{\mathbf{u}_*} = \frac{1}{\kappa} \ln\left(\frac{z - \mathbf{\Delta z}}{\mathbf{k_s}}\right) + B_r \tag{2.4}$$

where z is now the distance to the bottom of the sheet-flow layer (the limit between immobile and mobile sediments) and Δz is the theoretical level from the fixed bed towards which the velocity logarithmic law goes asymptotically (cf. figure 2.4).

Sumer et al. fixed $B_r = 8.5$ and $\kappa = 0.407$. In order to determine the value of the **parameters** $\mathbf{u}_*$, $\mathbf{\Delta z}$ and $\mathbf{k_s}$ in equation 2.4, they proceeded as follows:

- They combined the equations 1.28 (Clauser method) and 1.32 (Slope method) to obtain:

$$\tau_b = \gamma R S_f = \rho u_*^2 \quad \rightarrow \quad \mathbf{u}_* = \sqrt{g R S_f} \tag{2.5}$$

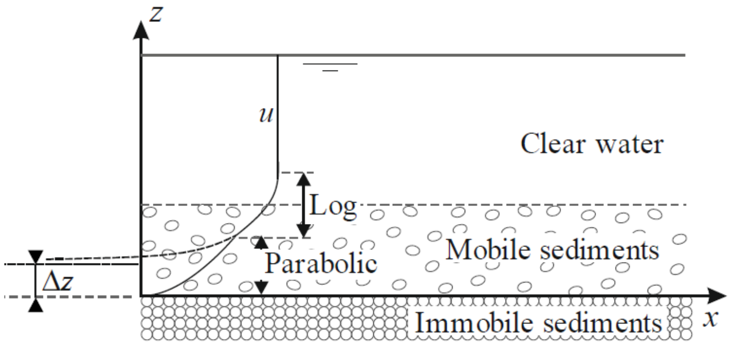

Figure 2.4: Definition of variables by Sumer et al. (1996), for a velocity distribution with logarithmic law near bed in presence of a sheet-flow layer
Reference : Thesis of Ilaria Fent, 2018

where they used $S_{f,Manning}$ (equation 1.33) in the Slope method. This value of u_* divided by κ, $\frac{u_*}{\kappa}$, corresponds in fact to the slope of the log-law velocity (equation 2.4) in the semi-logarithmic scale as we can see in the following development:

$$u = \frac{u_*}{\kappa} \ln\left(\frac{z - \Delta z}{k_s}\right) + u_* B_r \tag{2.6}$$

putting k_s out of the main logarithmic part

$$\underbrace{u}_{y} = \underbrace{\frac{u_*}{\kappa}}_{m} \underbrace{\ln(z - \Delta z)}_{x} + \underbrace{u_*\Big(B_r - \frac{1}{\kappa}\ln(k_s)\Big)}_{p} \tag{2.7}$$

giving, in the semi-logarithmic scale:

$$y = mx + p \tag{2.8}$$

with $m = \frac{u_*}{\kappa}$, the slope.

- Once $\mathbf{u}_*$ is fixed, they determined the value of $\mathbf{k_s}$, as part of the independent term p in equation 2.8 that allows the vertical translation

- Finally, they determined the value of $\mathbf{\Delta z}$ in order to fit the theoretical log-law profile (equation 2.4) with the experimental profile on the right portion of the profile as can be seen in figure 2.5 on the left. Sumer et al. also showed, in the same figure on the right, the dependence of the Δz values (adimentionalized dividing by d) with the Shield's parameter θ:

$$\theta = \frac{u_*^2}{g(s-1)d} \tag{2.9}$$

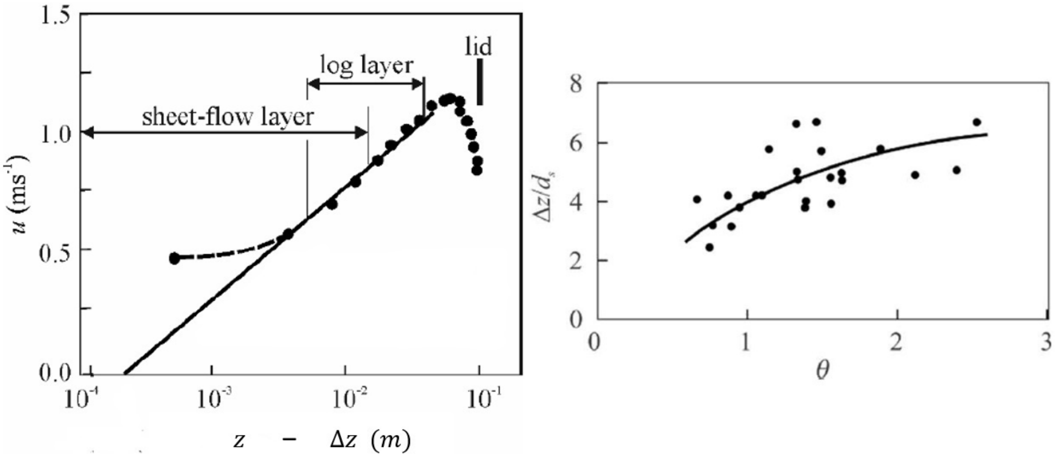

Figure 2.5: On the left : Experimental velocities fitted with the theoretical one
On the right : level of the theoretical bed Δz in function of θ
Reference : Sumer et al., 1996

Sumer et al. represented the thickness of the sheet-flow layer δ (adimentionalized dividing by d) in function of the Shield's parameter θ (cf. figure 2.6) where we can see that δ is proportional to θ.

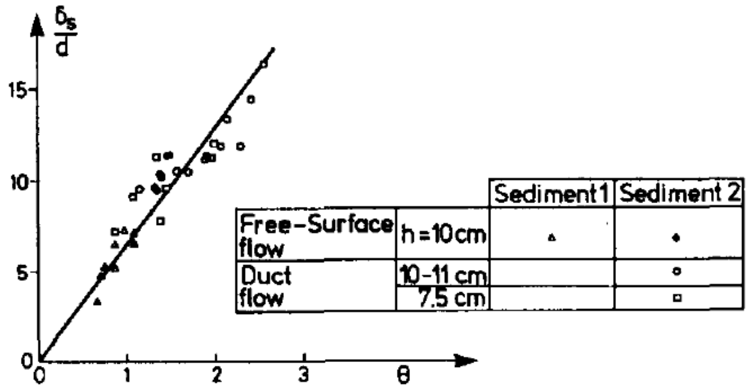

Figure 2.6: Thickness of the sheet-flow layer in function of θ
Reference : Sumer et al., 1996

In the lowest part of the sheet-flow layer, Sumer et al. observed a parabolic shape of the velocity, then they proposed a power law for the velocity distribution :

$$\frac{u}{u_*} = \frac{2.50}{\theta^{3/4}} \left(\frac{z}{d} \right)^{3/4} \tag{2.10}$$

2.4 Velocity distribution in unsteady flow over mobile bed

For this kind of flows, Qu (2003) carried out 12 experiments with various hydrographs in a tilting flume. The flow starts over a raised fixed bed with an appropriated roughness in order to condition the flow. A little further, the flow goes over a mobile fine gravel bed with the same roughness as the fixed bed. After that part of the flow, there is a trap that collects the transported sediments and behind that trap, we recover the same kind of bed as at the beginning of the flume. From his experiments, Qu deduced that the inner region follows a logarithmic profile and that the outer region deviates from the logarithmic trend and follows the Cole's wake function (cf. figure 2.7). No significant differences were observed in the inner region between experiments over fixed bed or over mobile bed.

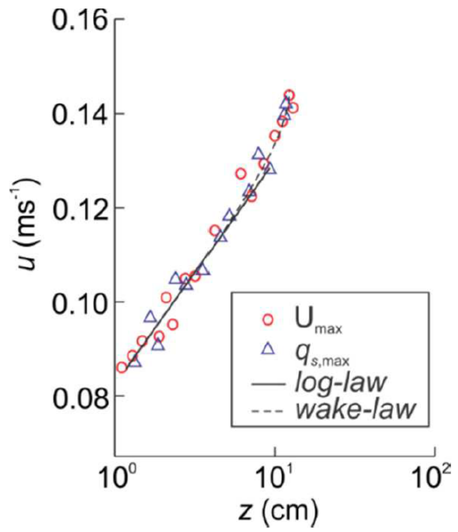

Figure 2.7: Example of velocity profile for an unsteady flow over mobile bed
Reference : PhD thesis of Qu, 2003

2.5 Analytical velocity distribution for the dam-break over frictionless and fixed bed

This part does not give us a velocity profile for the entire height of the section of the flow, but it gives a value of the average velocity and the height of flow for each section.

Ritter (1892) gave the first analytical solution of the dam break bed problem by solving the shallow water equations (equations 1.24 and 1.25) on a frictionless bed. He made several assumptions:

- Rectangular prismatic channel
- Infinite extension
- Horizontal ($S_0 = 0$) and frictionless ($S_f = 0$) bed

He considered the flow resulting from the sudden removal of a gate between a reservoir initially filled with a depth of water h_0, and an initially dry channel (cf. figure 2.8(a)). With these assumptions, the equations 1.24 and 1.25 become:

$$\frac{\partial h}{\partial t} + \frac{\partial q}{\partial x} = 0 \tag{2.11}$$

$$\frac{\partial q}{\partial t} + \frac{\partial}{\partial x}\left(\frac{q^2}{h} + g\frac{h^2}{2}\right) = 0 \tag{2.12}$$

The analytical solution is given by:

$$\frac{U(x,t)}{c_0} = \frac{2}{3}\left(1 + \frac{x}{c_0 t}\right) \tag{2.13}$$

$$\frac{c(x,t)}{c_0} = \frac{\sqrt{gh}}{\sqrt{gh_0}} = \sqrt{\frac{h}{h_0}} = \frac{2}{3}\left(1 - \frac{1}{2}\frac{x}{c_0 t}\right) \tag{2.14}$$

where $c(x,t)$ is the relative celerity of an infinitesimal perturbation and c_0 is the same relative celerity associated to the initial depth of water in the reservoir h_0.

When $U(x,t) < c(x,t)$, information can travel both in the upstream and downstream direction and the flow is called subrictical.
When $U(x,t) > c(x,t)$, information can only travel in the downstream direction and the flow is called supercritical.

Noting that when $h(x,t) = h_0$, equation 2.14 gives :

$$\sqrt{\frac{h_0}{h_0}} = 1 = \frac{2}{3}\left(1 - \frac{1}{2}\frac{x}{c_0 t}\right) \quad \rightarrow \quad x = -c_0 t \tag{2.15}$$

And when $h(x,t) = 0$ (position of the front wave), equation 2.14 gives :

$$\sqrt{\frac{0}{h_0}} = 0 = \frac{2}{3}\left(1 - \frac{1}{2}\frac{x}{c_0 t}\right) \quad \rightarrow \quad x = 2c_0 t \tag{2.16}$$

These results are shown in figure 2.8(b) and figure 2.8(c) and thanks to these results, we can easily predict the position of the back wave an the position of the front wave at every time.

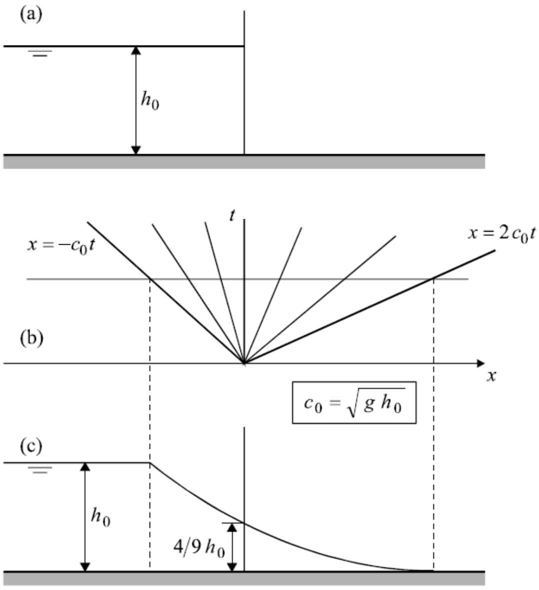

Figure 2.8: Analytical solution
Reference : LGCIV2054 - Transient flows taught by Sandra Soares Frazao

Note that the water depth $h(0,t)$ and the velocity $U(0,t)$ do not vary in time at the position of the gate ($x=0$) and are respectively equal to $\frac{4}{9}h_0$ and $\frac{2}{3}\sqrt{gh_0}$. As time passes, these values act as pivot points as can be seen in figure 2.9.

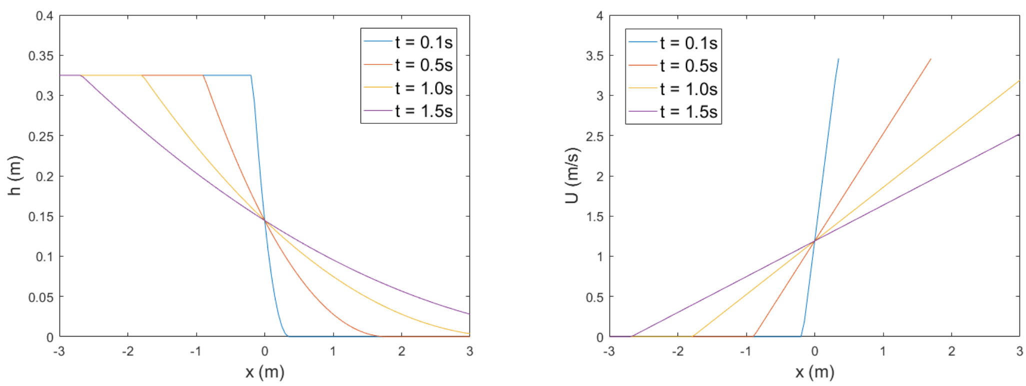

Figure 2.9: Evolution of water depth h and average velocity U in time for a initial water depth $h_0 = 0.325m$

Rui Aleixo showed in his PhD thesis (2013) that this analytical solution corresponds well to experimental measurements. He performed the dam-break experiment without using any eroded material, unlike us. He filled the upstream part of the dam with water (initial depth h_0), then determined the water height (cf. figure 2.10), the velocity profiles at different x, and at different times over the entire height of the flow (cf. figure 2.11). Working with nondimensional values (in uppercase letters), he noticed that for given X and T, Z and U would take the same value regardless of the initial condition h_0.

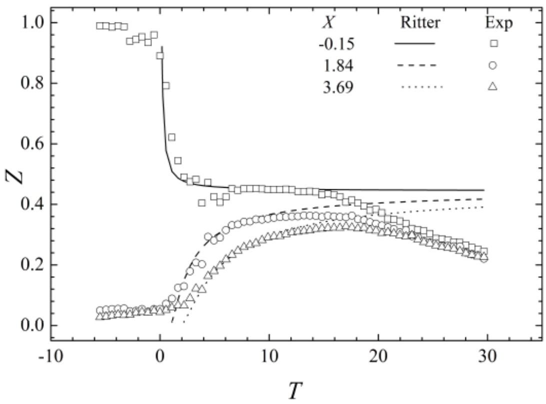

Figure 2.10: Comparison between the average values of the water level evolution in three different points and the Ritter solution. (Initial water level: $h_0 = 0.325m$) - Reference : Rui Aleixo's thesis (2013)

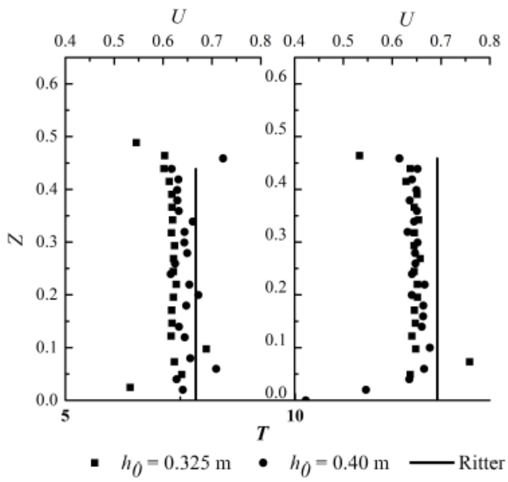

Figure 2.11: Comparison between theoretical mean velocity obtained from Ritter model and measured velocity profiles for T = 5 and T = 10 at X = 0. Reference : Rui Aleixo's thesis (2013)

He came to the conclusion that the obtained velocity results compared quite well between them and with the Ritter solution. The differences between the theoretical values and experimental results could be explained by the limitations of Ritter's model, since it takes into account neither the vertical component of velocity nor the friction with the channel's bed.

2.6 Velocity distribution for the dam-break over mobile bed

A dam-break flow over mobile bed is also an unsteady flow over mobile bed but it has an important transient character.

In this section we present the different analyses made by Ilaria Fent in her thesis and by Donifan Camacho and Pauline Radelet in their Master's thesis.

2.6.1 Conclusion of the thesis of Ilaria Fent

Throughout her PhD, Ilaria Fent carried out experiments in a flume that models a dam break over a mobile bed. The experiment set-up is explained at section 3 and is the same set-up that we used for our experiments.

Based on her experiments, she observed that every velocity profile had the same trend that was divided in 3 parts as shown in figure 2.12:

- (1) the first part where the velocity u evolves with z from 0 to a certain value.
- (2) the second part where the velocity varies around a constant value.
- (3) the last part near the surface level where we can observe a diminution of the velocity due to the Cole's wake effect in contact with air.

In figure 2.12 are also shown the levels z_w, $z_{b,up}$ and $z_{b,low}$ that represent respectively the water surface level, the upper level of the sheet-flow layer (layer containing the transported sediments) and the lower level of the sheet-flow layer (corresponding to the interface between mobile bed and non-mobile bed). It is important to note that these three levels do not correspond to the separation of the three parts ((1),(2),(3)).

By reversing the axes and making the abscissa logarithmic, Ilaria Fent detected a log-law in the upper part of the sheet-flow layer and in the lower part of the clear water (cf. figure 2.13), similarly to Sumer et al.'s observation in steady flows over mobile bed (cf. figure 2.5).

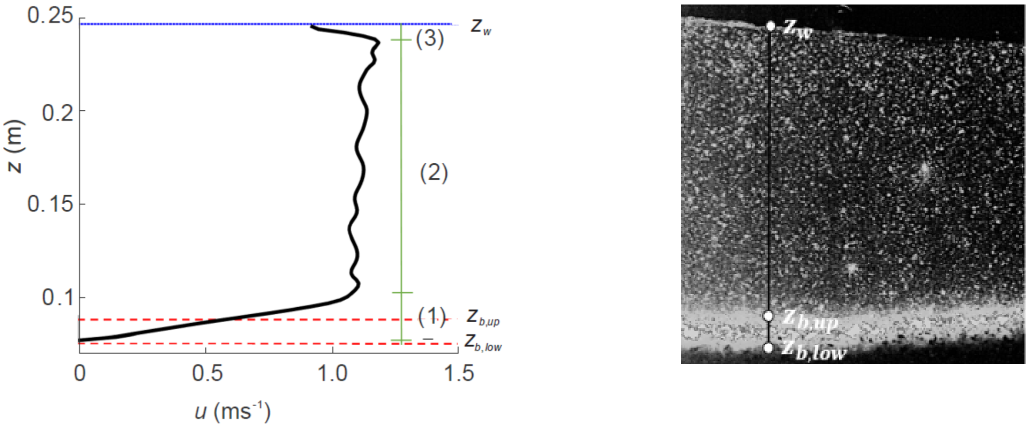

Figure 2.12: On the left : the 3 parts of horizontal velocity profile at the gate section (x = 0) at time = 1 s - On the right : Picture of the flow for $x = [-0.05m \quad 0.15m]$ at time = 1 s where the levels z_w, $z_{b,up}$ and $z_{b,low}$ are illustrated at gate section (x = 0)
Reference : Adapted from Ilaria Fent's thesis, 2018

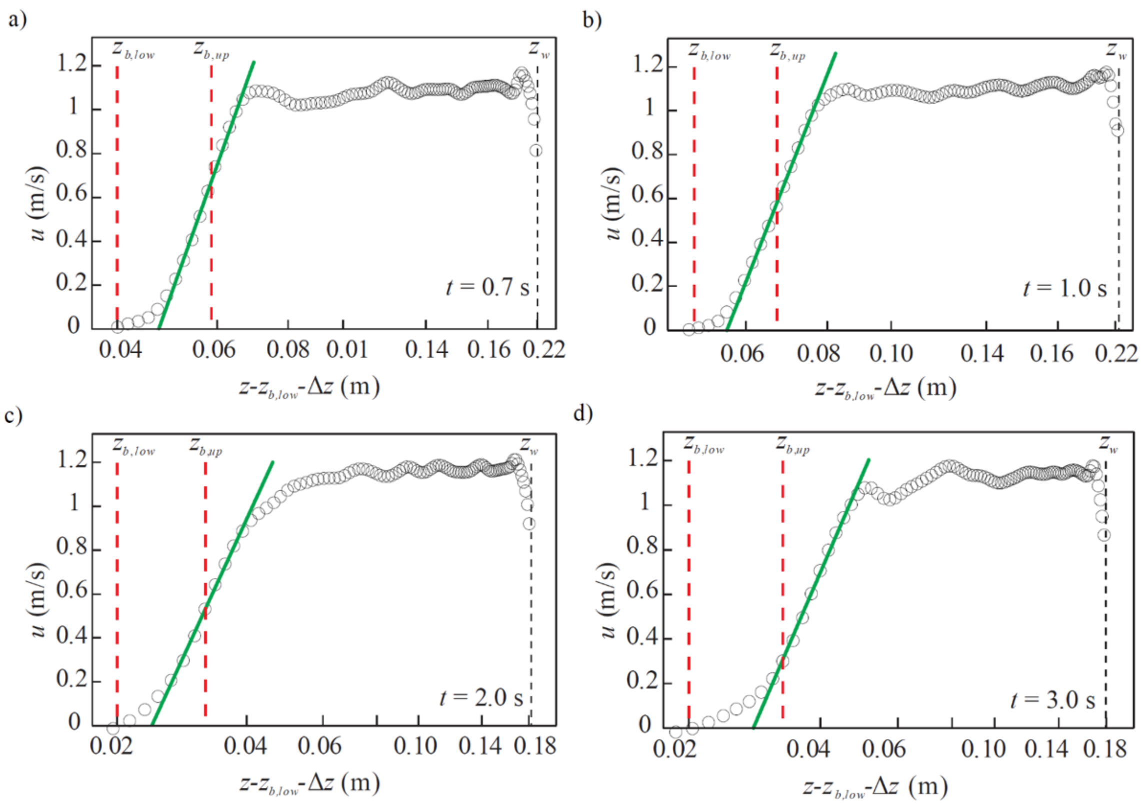

Figure 2.13: Semi-logarithmic plot of horizontal velocity for different times at x = 0 m - Reference : Thesis of Ilaria Fent, 2018

Figure 2.13 shows, for times $t = 0.7s, 1s, 2s, 3s$ the comparison between the experimental velocity and the logarithmic regression line computed from :

$$u = \frac{u_*}{\kappa} \ln(z - z_{b,low} - \Delta z) + u_* \Big(B_r - \frac{1}{\kappa} \ln(k_s)\Big) \tag{2.17}$$

where $\frac{u_*}{\kappa}$ is the slope of the line on the semi-logarithmic scale where she extracted the value of the shear velocity u_* and where Δz is the theoretical level from the fixed bed towards which the velocity logarithmic law tends asymptotically. The value of Δz is as the one giving the best linear regression for the measured values of the velocity closest to the upper limit of the mobile bed layer $z_{b,up}$, considering at least 8 measured points.

Ilaria Fent calculated the value of parameters for the four considered times that are summarized in table 2.1.

time (s)	$z_{b,up}$ (m)	$z_{b,low}$ (m)	Δz (m)	u_* (m/s)	θ (-)
0.0	0.10	0.10			
0.7	0.090	0.071	-0.04	1.26	57.26
1.0	0.089	0.072	-0.05	1.32	62.95
2.0	0.091	0.079	-0.02	0.74	19.91
3.0	0.091	0.078	-0.02	0.79	22.61

Table 2.1: Evolution of the variables needed in the velocity distribution study and the consequent calculation of shear velocity and Shield's parameter

It can be observed in figure 2.13 that the log-law progressively develops in the clear water (over $z_{b,up}$) with the increase of time.

Once the shear velocity u_* was found and thanks to the Clauser method (cf. subsection 1.7.1), it's simple to find the bed shear stress $\tau_b = \rho u_*^2$. For all u_* found at all times an all positions, she found that τ_b was between 5 and 15 Pa.

Ilaria Fent also tried the Reynolds stress method requiring to extract the velocity fluctuations. But she concluded that this method was not easy to apply to her data because of the difficulty to differentiate the right velocity fluctuations caused by the turbulence with the bad ones that are caused by the experimental inaccuracies. For this reason, we did not used this method neither in our analyses.

2.6.2 Conclusion of the Master's thesis of Donifan Camacho & Pauline Radelet

In their Master's thesis, Donifan Camacho and Pauline Radelet confirmed that a log-law was present in the velocity profile on a dam-break flow over mobile bed. They used different ways to determine τ_b, but in particular, they explained that the slope method $\tau_b = \gamma R S_f$ using S_f calculated by Manning, underrated the value of τ_b.

Therefore, we tried to understand their conclusion but we found a flaw in their explanation about the underrating. We develop it in the following lines.

First, they calculated $\tau_b = \gamma \frac{U^2 n^2}{R^{1/3}}$ combining equations 1.32 and 1.33 and they found values of τ_b around 9 Pa. Once that value found, they used $\tau_b = \rho u_*^2$ in order to extract the value of u_* where u_*/κ corresponds to the slope of the log-law in the Sumer et al. equation:

$$\underbrace{u}_{y} = \underbrace{\frac{u_*}{\kappa}}_{m} \underbrace{\ln(z - z_{b,low} - \Delta z)}_{x} + \underbrace{u_* \Big(B_r - \frac{1}{\kappa}\ln(k_s)\Big)}_{p} \tag{2.18}$$

In figure 2.14, they plotted the experimental velocities with the theoretical ones and they manage to fit them thanks to the manipulation of the parameter Δz.

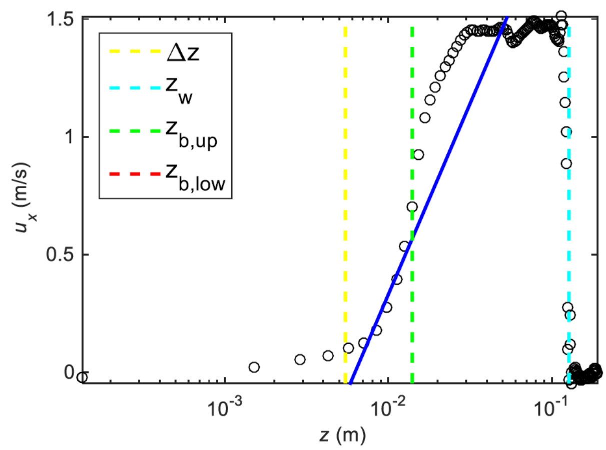

Figure 2.14: Experimental Velocity profile compared with the theoretical one - Taking $z_{b,low}$ as reference level
Reference : Master's thesis of Donifan Camacho Pauline Radelet, 2019

They conclude by saying that the calculated value of u_* was not the optimal one because, as can be seen in figure 2.14, the slope of the theoretical profile (in blue) could better fit with the experimental velocities if another value of $u*$ was chosen.

So they tried another way to find the best fit between the theoretical and experimental values. Instead of calculating u_* with the slope method, they directly used the Clauser method by finding the best value of u_* that perfectly fitted with experimental values as can be seen in figure 2.15.

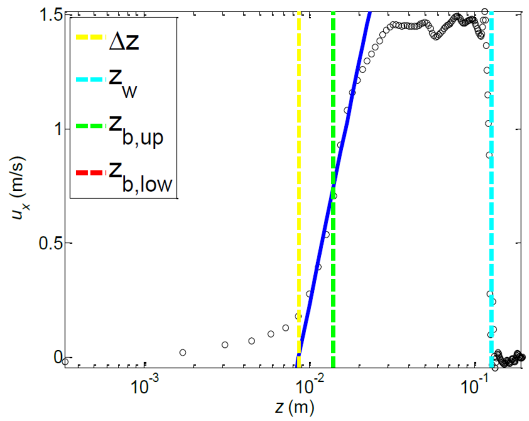

Figure 2.15: Experimental velocity profile compared with the theoretical one - Taking $z_{b,low}$ as reference level
Reference : Master's thesis of Donifan Camacho Pauline Radelet, 2019

This way, they obtained values around $\tau_b = 90Pa$, which is approximately ten times larger than the previous method. It was the reason why they concluded that the slope method using $S_{f,Manning}$ underrated the shear stress τ_b.

The error that was made in this conclusion lies in the manipulation of the graph in figure 2.14 and 2.15. As can be seen, the abscissa are "z" but, in reality, Δz must be included in the axis.

Indeed, shifting horizontally a logarithm function in a standard axis system (with the parameter Δz, for example) is not equivalent to the horizontal shift of a linear function on a semi-logarithmic axis-system. More explicitly:

Let $z' = z - z_{b,low}$ and

$$u = m\ln(z') + p \tag{2.19}$$

be the linear form of the log-law (equation 2.18) without any shift. If we try to find a linear regression of the points (ln(z'),u), we logically find the slope m and the intercept p.

Next, if we apply a shift so that:

$$u = m \ln(z' - \Delta z) + p \tag{2.20}$$

It is necessary to make a linear regression of the points ($\ln(z' - \mathbf{\Delta z})$,u) in order to find the correct slope m and intercept p, and then, to take account of Δz. What was apparently not considered in the method.

This leads to the important conclusion that u_* and Δz have to be found at the same time as part of an optimization. And so, the calculation they made using S_f calculated by Manning could give a value of u_* which would correctly fit the experimental velocity profile with the theoretical one if we choose the appropriate Δz.

Chapter 3

Dam break experiment

One of our goals with this thesis was to enlarge the database of experiments but the lockdown related to the coronavirus outbreak stopped us. Before the lockdown, we took the time to familiarize ourselves with the lab and we did the experiment several times to verify that we were correctly following the protocol followed by our predecessors. Unfortunately, we did not have the time to modify any parameter to enlarge the database but we made some suggestions for our successors in the conclusion chapter. It was not really a problem because, for this reason, we had more time to carry out our new ideas of analysis on Ilaria Fent's experimental data. It is worth reminding the experimental set-up our predecessors used.

3.1 Experimental set-up

The dam break experiments have been realized in the LEMSC (Laboratoire essais mécaniques, Strctures et Génie civil) laboratory. The channel has a rectangular cross section 25 cm wide and 50 cm high and a length of 6 m. Overall views of the channel can be seen in figure 3.1. The geometry is also shown in figure 3.2.

The walls are made of glass so that the phenomena are observable. The gate is halfway between the upstream end and the downstream end. It is made of aluminum, 12 mm thick, 24.4 cm wide and 80 cm high. This gate acts as the dam. By making it go down very quickly, we simulate a dam failure.
The parameters of the experiment are basically the initial water depth in the reservoir h_0, the nature of the sediments being eroded, and the height of the layer of sediments on the bottom of the flume.

The Shields diagram can be useful to determine if a material will be eroded or not. We showed that it is the case for our sand in figure 1.9.

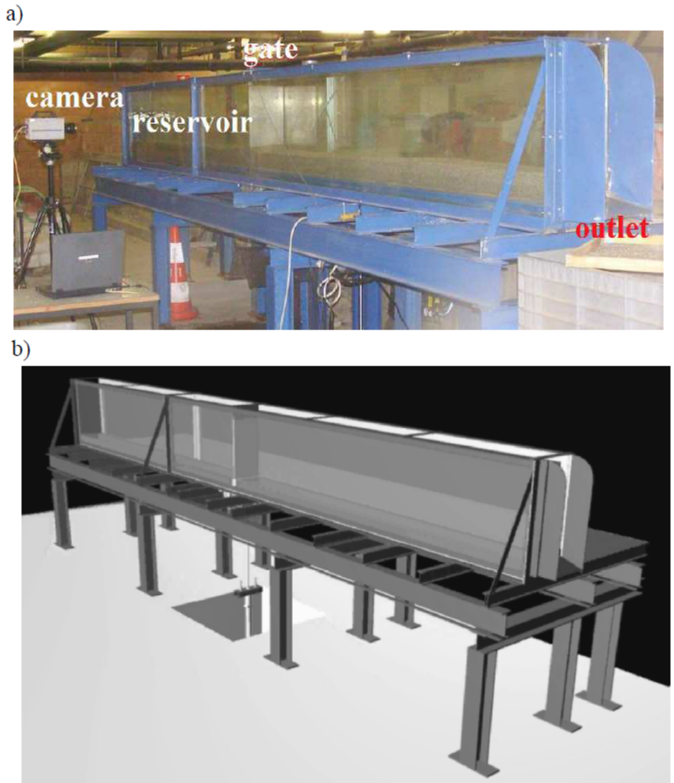

Figure 3.1: Dam break channel in the Hydraulic Laboratory of UCLouvain.
a) photo at the laboratory; b) overall view from Spinewine (2005)
Reference : Ilaria Fent's thesis (2018)

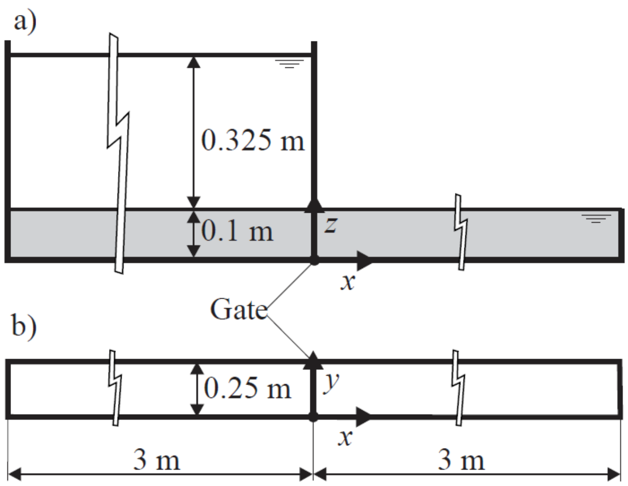

Figure 3.2: Geometry of the dam break channel, with the initial condition of water and sediment depths. - Reference : Ilaria Fent's thesis (2018)

A 10 cm high layer of sediments is placed along the entire length of the flume. The characteristics of the sand we used can be found in Table 3.1.

To preserve the initial conditions in order to ensure repeatability, we compact the sediments as evenly as possible using a 10 kg mass released from the same height using an instrument made by previous students as shown in figure 3.3.

Figure 3.3: Compacting system
Reference: Donifan Camacho-Fernandes and Pauline Radelet's Master's thesis (2019)

Both Ilaria Fent and us made the experiments by filling the upstream part of the canal with an initial water depth of $h_0 = 32.5cm$. After filling the upstream part of the canal, we also saturated the sand with water in the downstream part to preserve the initial conditions.

Characteristic of the sand	Symbol	Value
Density	ρ_s	2682 kg/m^2
Median diameter	d_{50}	1.72 mm
Diameter at 10%	d_{10}	1.15mm
Uniformity coefficient	d_{60}/d_{10}	1.8/1.3=1.38
Porosity (void volume fraction)	ε_0	0.42
Bed concentration	c_0	0.58
Friction angle	φ	38°
Permeability	k	2.27 10^{-2}m/s
Dry volumetric weight	W	14.54 kN/m^3

Table 3.1: Sediment characteristics of our experiments

As we used the Particle Image Velocimetry (PIV) to determine the velocity profiles, the choice of the tracer particle is important. We explain this method in more details in section 4. Ilaria Fent chose to use Eliokem's pliolite® because of its density close to the density of water ($\rho_P/\rho_w = 1.03$). She noticed that using a sieve at 475 μm to filter the pliolite gave satisfying results. Next, we mix the pliolite with water and soap in a bottle. This allows a better dispersion in the fluid. Otherwise, the particles would tend to float due to the surface tension of the water. This mixture is then incorporated into the water upstream of the door.

When everything is ready, we make the gate go down very quickly thanks to a pneumatic system, as shown in figure 3.4, which consists in a compressor, a compressed air receiver, a pressure gauge and a valve.

Figure 3.4: On the left: View of the canal gate - On the right: Pneumatic system
Reference: Donifan Camacho-Fernandes and Pauline Radelet's Master thesis (2019)

When the compressor is switched on, the air is compressed up to 8 bars and, by opening the valve, the pressurized air is transferred to the compressed air receiver. The purpose of this reservoir is to minimize the distance to the solenoid valve that activates the cylinder, so as to minimize pressure drops. In order to ensure good repeatability, it is important to recharge the pressure in the pneumatic system to 8 bars. The entire circuit is controlled by a Programmable Logic Controller (PLC) on which we find 3 switches. The first and the third, when held for 5 seconds, control the descent of the door. The second one, on the other hand, raises the door. It is also possible to connect the camera to the PLC so that holding the first and the third switches triggers the camera (cf. figure 3.5). This is practical for several reasons: first of all, the starting time of the experiments is standardized, and secondly, it saves the little memory the camera has.

Figure 3.5: On the left: Programmable Logic Controller - On the right: High-Speed Camera - Reference: Donifan Camacho-Fernandes and Pauline Radelet's Master thesis (2019)

The high-speed camera is the "fastcam SA3 Photron" (cf. figure 3.6.c)). It offers high-resolution images 1024 x 1024 pixel at frame rates up to 1000 fps. Like Ilaria Fent, we chose to keep the frame rate of 500 fps, which, considering the 2 Gb memory of the camera, allows recording a little bit less than 3 seconds at maximum resolution.

In addition to the tracer we talked about earlier, the detection of velocity by PIV requires the illumination of the studied longitudinal section (parallel to the walls) using a laser with a spectral wave length $\lambda = 660\mu m$ (cf. figure 3.6.a) and b)). This laser allows the software DaVis (LaVision) to detect the pliolite particles. The PIV process is explained in more details in section 4.1

Once the experiment has been carried out, the water is collected in a tank located at the outlet of the canal and on which a sieve is placed to collect the transported sediments. In order to reuse the water, a cellar pump returns the water to the upstream side of the gate.

Appendix A contains a laboratory checklist made by Donifan Camacho and Pauline Radelet in French for successor students.

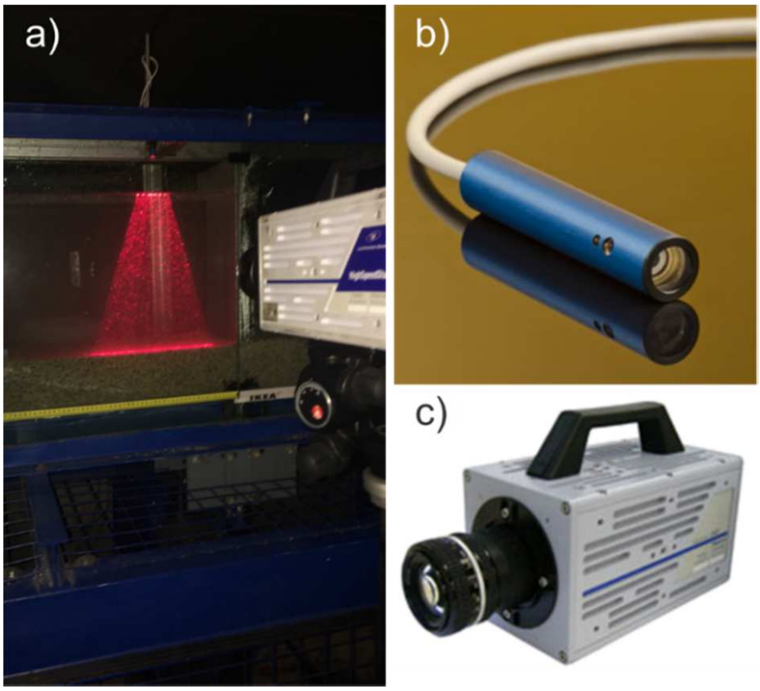

Figure 3.6: Devices used to record the dam break experiment: laser and high-speed camera. - Reference : Ilaria Fent's thesis (2018)

3.2 Instantaneous gate opening

We said that we had to make the gate go down very quickly, but is it quick enough to be considered instantaneous ? That's the question we address.

As proposed by Lauber and Hager (1998) and as studied by Aleixo et al. (2011), we can use the following criterion to check that the removal time of the gate t_r is sufficiently small for the removal of the gate to be considered instantaneous:

$$t_r < \sqrt{2\frac{h_0}{g}} \tag{3.1}$$

The initial water depth upstream the gate in our experiments is 32.5 cm, which leads to

$$t_r < 0.257s \tag{3.2}$$

As explained by Ilaria Fent in her thesis, Aleixo (2013) understood that the acceleration of the door depends on the deflection due to the hydrostatic pressure and on the friction between the gate and the water column. He proposed a second criterion to calculate the removal time with a stricter definition:

$$t_r < \sqrt{2\omega \frac{h_0}{g}} \tag{3.3}$$

with $\omega = z_p/h_0$, where z_p is the height of non-perturbed water at the first moment the gate is totally removed.

Ilaria Fent calculated the time interval between the instant corresponding to the top of the gate at the free water surface level, and the instant when it's at the border between water and sediments. The time interval between these two images is $t_r = \Delta t = 9.2 * 10^{-3}s$. She compared this value with $t_r < \sqrt{2\omega \frac{h_0}{g}}$ where she estimated $\omega \approx 0.3$ based on figure 3.7. This leads to $t_r < 0.14s$

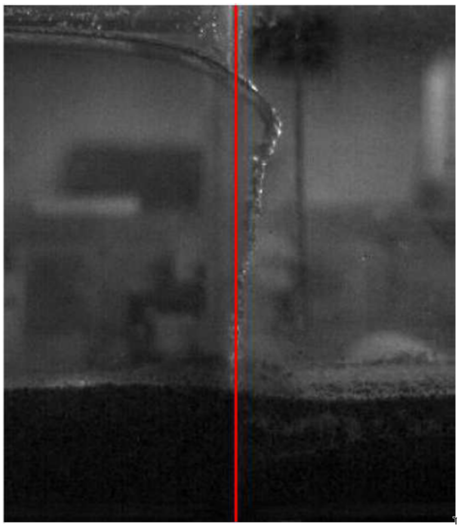

Figure 3.7: Water column perturbation due to removal gate at the instant when the top of the gate is at the border between water and sediments.
Reference : Ilaria Fent's thesis (2018)

The actual removal time $t_r = 9.2 * 10^{-3}s$ meets both criteria. We can therefore consider the opening of the door to be instantaneous.

Chapter 4

Experimental data processing

In this chapter we explain the way the data are extracted in order to use them in our analyses. This measurement explanations are highly inspired from Ilaria Fent's thesis and from Donifan Camacho and Pauline Radelet's Master's thesis.

The main gross observations we can extract from the experiments are the evolution of the free water surface z_w and the movement of sediments within the bed in order to understand the limit between the clear water layer, and the sediment layer and between the mobile and the fixed bed.

4.1 Detection of velocity by PIV

The Particle Image Velocimetry (PIV) is the method used for the analyses of the laboratory experiments. This method covers a series of images in order to compute velocity vectors. This method has the advantage to be non-intrusive (avoiding thus the modification of the flow) contrary to the more classical methods such as the ADCP (Acoustic Doppler Current Profiler).

In order to compute velocities by PIV method thanks to the software DaVis 8 (LaVision), the necessary and sufficient condition is to cover at least 2 images of the flow like in figure 4.1, in which the water particles are traced.

In the case of our experiments, we use pliolite as tracer as explained at chapter 3, which mixes perfectly with water particles. As a result, the calculation of the tracer velocity is a perfect representation of the water velocity.

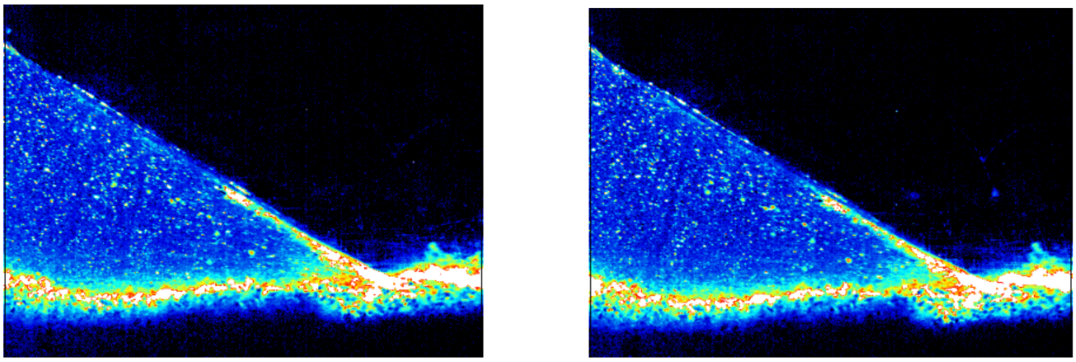

Figure 4.1: Gross images of our experiment with a time interval of 0.002 s between the 2 images

4.1.1 Principle

Explained in simple terms, the PIV principle consists in the detection of a group of particles present on an image and to spot the same group of particles on the next image by means of software. In more details, every image saved with the camera is composed of pixels that have the same size but different shades and intensities. The PIV method consists then in the division of the image into small interrogation windows which are all composed of a pixel fraction (that we have to determine) representing a little part of the full initial image.

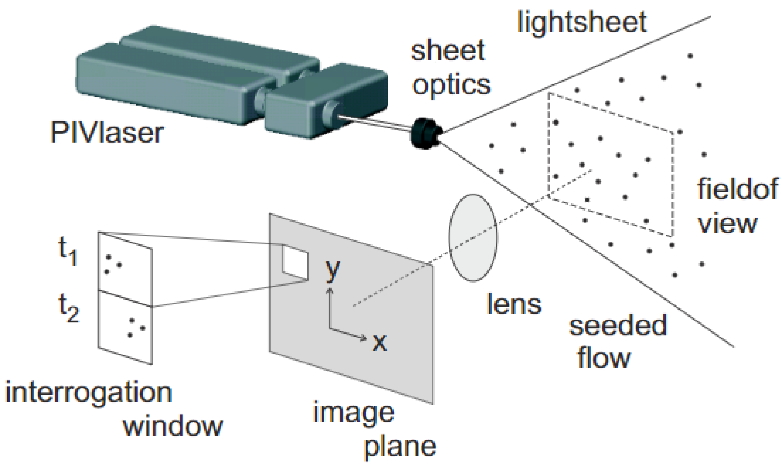

Figure 4.2: General setup of a 2D PIV system
Reference : FlowMaster manual of LaVision

By performing a cross-correlation between an interrogation window taken at time t and the same interrogation window at time $t + dt$ (dt being the time interval between the two images), the software using the PIV method tries then to determine a correlation peak as shown in figure 4.3. In other words, the software looks for the most likely displacement of a group of particles detected on time t and within dt seconds.

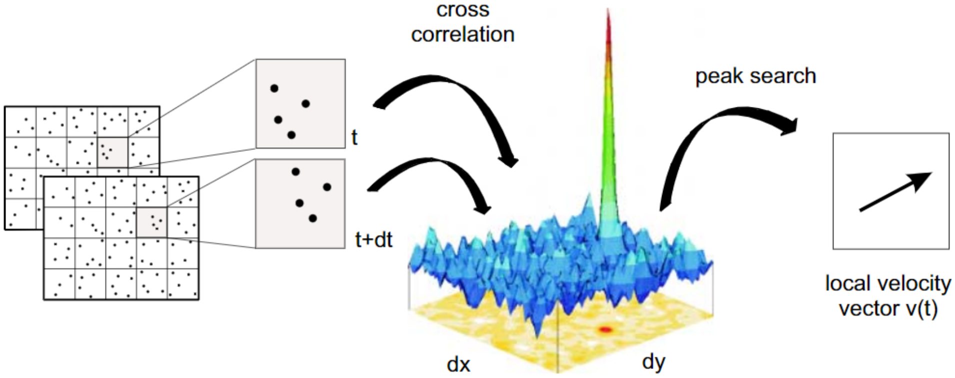

Figure 4.3: Illustration of a correlation peak
Reference : FlowMaster manual of LaVision

Once the displacement dx of this group is found, the calculation of the velocity vector is easy if we apply the definition of velocity :

$$v = \frac{dx}{dt} \tag{4.1}$$

During Ilaria Fent's experiments, the camera took 500 images per second, so the time interval is $dt = 0.002s$. Obviously, the software performs this calculation, and also repeats these operations for all the interrogation windows of the image, and that for all uploaded images to be processed.

Given that we have a lot of images to process, that an image is generally 1024x1024 pixels, that each image is divided into several hundred interrogation windows and that on each window may stand several flow particles, the calculation of velocity vectors can be time consuming, even with a very powerful computer.

4.1.2 Calibration

Before starting the experiment, the camera is placed in front of the desired channel portion. Once the balancing of the camera is tested, a first image of the calibration plate is taken (figure 4.4 on the left). It is important to place the calibration plate exactly vertical under the laser sheet. The perpendicularity of the calibration plate is verified by a spirit-level tool.

If the camera is placed in front of a downstream portion (initially dry), it is important to fill this portion with water just during the calibration time.

The picture generally suffers from distortion, depending on the lens used, so they must be numerically corrected after each test in order to recover parallel lines (figure 4.4 on the right), and to transfer pixel data into the metric system. The calibration of all the other images recorded during the experiment is automatically completed by the software DaVis8 (LaVision), once the calibration plate is uploaded.

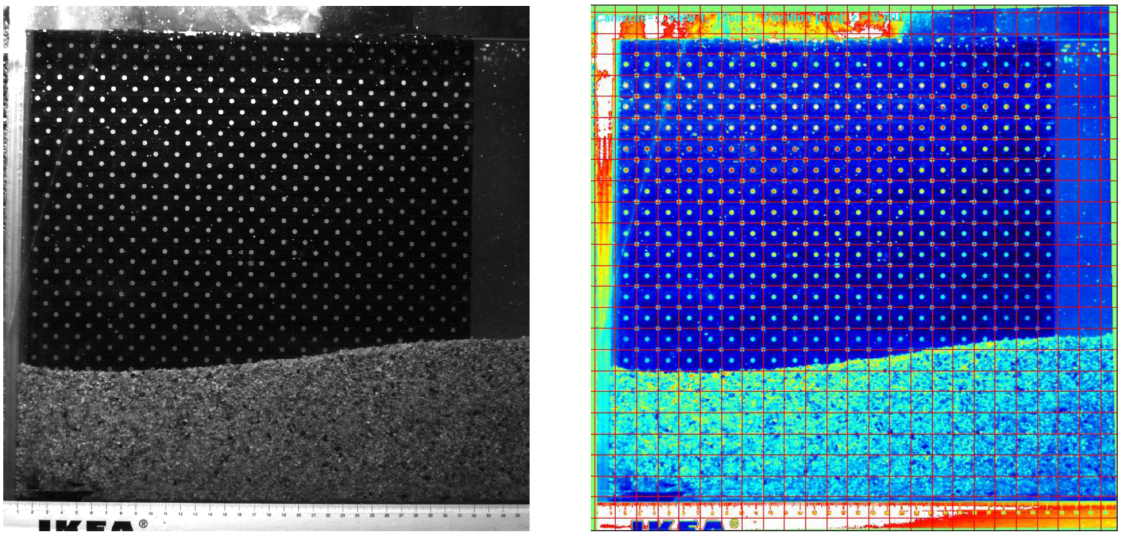

Figure 4.4: On the left : Image of the calibration plate
On the right : Image corrected thanks to the calibration on DaVis8
Reference : Master's thesis of Donifan Camacho and Pauline Radelet

4.1.3 Overlap

Another important notion to understand is the overlap. Let us return for a moment to the determination of the correlation peak between 2 corresponding interrogation windows. If it seems obvious to have to compare 2 windows located at the same position for 2 different images, the detection of the group of particles in a window from the image at time t and in a window from the image at time $t + dt$ must be done with a certain step, which is linked to an option proposed by DaVis8 called overlap.

To illustrate this concept, let us consider the simple case of a chosen overlap of 0% of the size of the initial interrogation window. This means that, after having identified a group of particles in a window from the image at time t, the software will search this group of particles, from the same window but on the image at time $t + dt$, and being allowed to spot in the adjacent windows to the starting one (since an overlap of 0% has been chosen).

If we choose an overlap of $X\%$, the software would search for the group of particles from the same window on the image at time $t + dt$ but this time being allowed to spot the windows shifted by $100 - X\%$ of the initial size, as shown in figure 4.5.

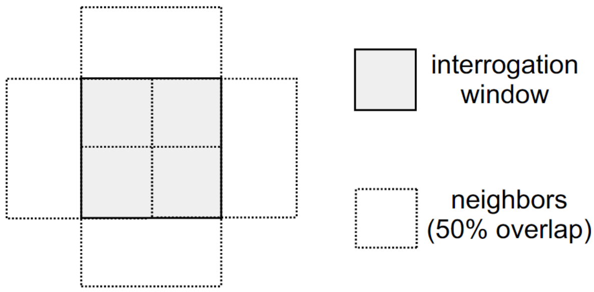

Figure 4.5: Example for 50% interrogation window overlap
Reference : FlowMaster manual of LaVision

4.1.4 Calculation example

The example shown in figure 4.6 is a good way to illustrate the PIV method we use for the velocity vector calculations :

- Illustration (a) presents a gross image $I1$ of a flow where the particles have been traced. The small cells in thin black lines are the different interrogation windows. A red line cell $w1$ is identified by the software.
- Illustration (b) presents another gross image $I2$ of the same flow taken at the same position as image $I1$ but dt seconds later. The red interrogation window $w2$ is identified in the same place on image $I2$ as $w1$ on $I1$.
- On illustration (c) the software identified in red all the traced particles inside $w1$ of image $I1$ at time t. In this case there is 4 particles.
- On illustration (d) the software tries to spot, on $I2$ at time $t + dt$, the group of 4 particles previously identified on $w1$, which is obviously next to cell $w2$.

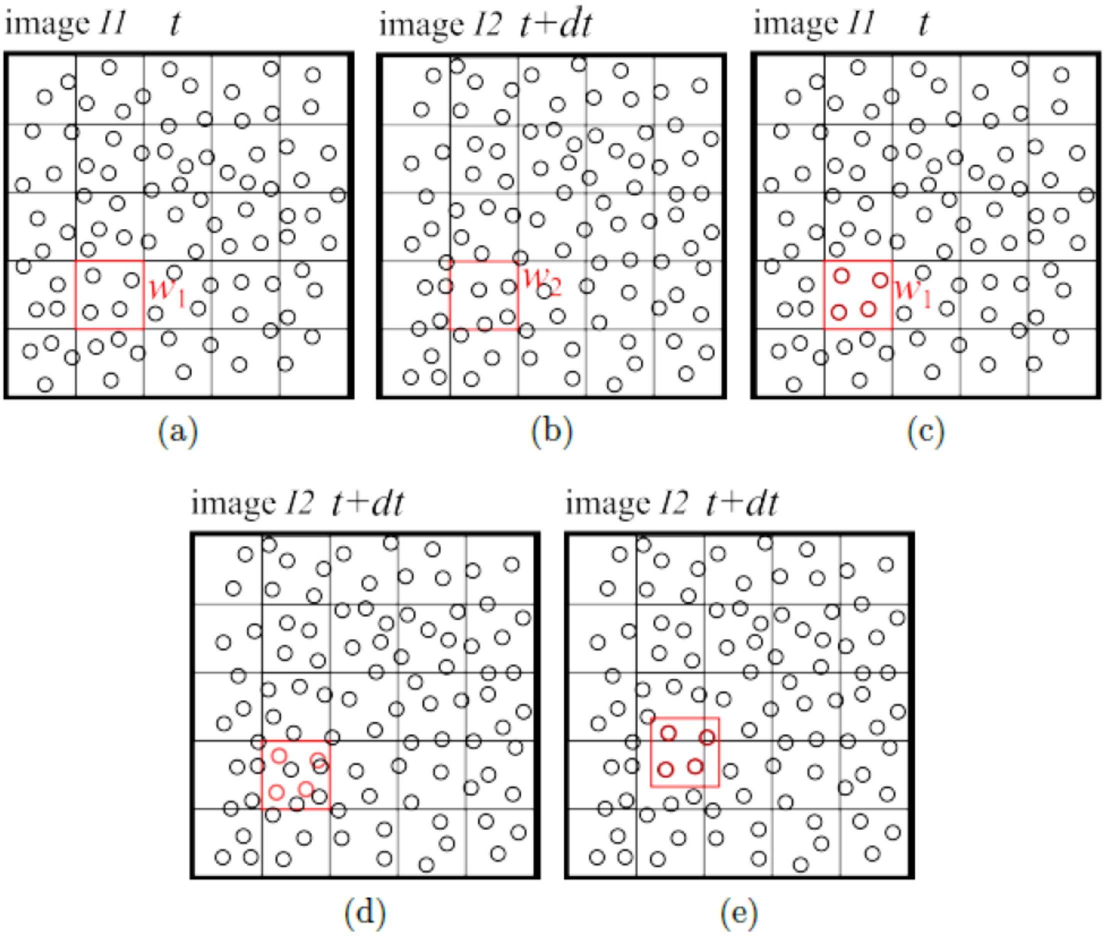

Figure 4.6: Example of PIV method
Reference : Master's thesis of N. Behet-Wydemans and F. Jacques

- On illustration (e) the software finds the group of 4 particles which is located in the adjacent interrogation windows on $I2$, overlapping more or less the starting window $w2$. This way the software makes a correlation between the position of the 4 initial particles on $I1$ and the position of these on $I2$. The correlation peak obtained therefore corresponds to the most likely position of the 4 particles of $w1$ on image $I2$.

  Finally, and thanks to the displacement to which this peak corresponds, the software can calculate the velocity vector of these 4 particles by dividing their displacement dx by the time interval dt between image $I1$ and $I2$.

4.2 Determination of the water and bed surfaces

Once the recording and the calculation of the velocity vectors are done, the last step to do in order to extract all the gross data is to determine the levels z_w, $z_{b,low}$ and $z_{b,up}$ from the recorded images.

At the beginning of the treatment of the recorded images, we tried to use a Matlab code previously used by our predecessors in order to extract these values. That Matlab code was based on the identification of a difference in contrast and intensity between pixels. After specifying the minimum and maximum threshold intensity values, the pixel deviation tolerances and the grain size in pixels in a calibration file, the code applies a binomial filter on the image and detects the free surface z_w, the upper limit of the sheet-flow layer $z_{b,up}$ and the interface between the non-mobile bed and the mobile bed $z_{b,low}$.

Unfortunately, we had some difficulties with this code given that the identification of these levels was not satisfactory and required to change the parameters calibration file for each experiment (cf. figure 4.7).

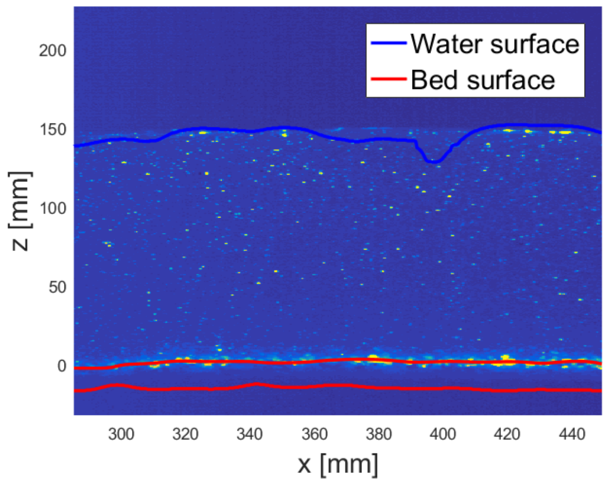

Figure 4.7: Levels found by the Matlab code : Not satisfactory

Finding the right calibration parameters for each image we analyzed was a waste of time, so we decided to use a less automated but more satisfactory method: to identify the different levels manually thanks to another option of this Matlab code which allowed us clicking on several points belonging to the level interfaces that we detected (cf. figure 4.8). Admittedly, this method is not very optimal but it takes us less time than the first.

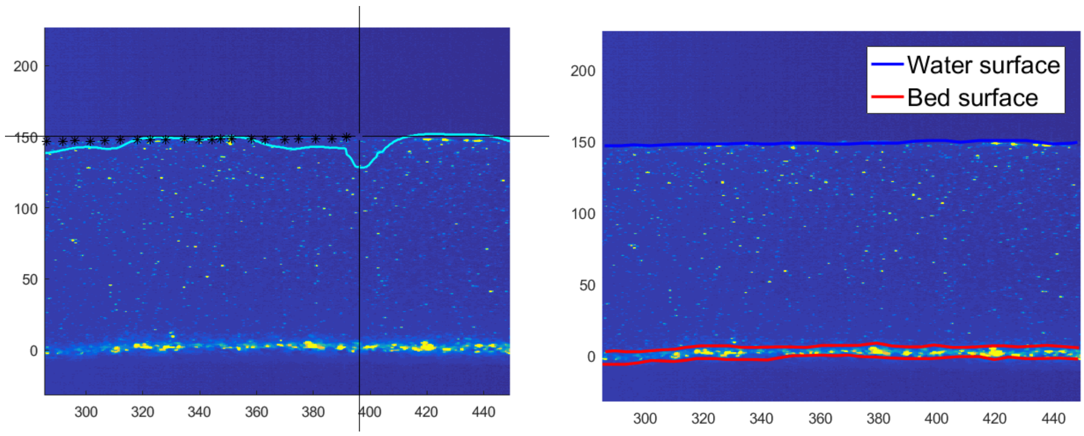

Figure 4.8: On the left : Cursor which allowed to click on points belonging to the level interfaces - On the right : Levels found by manual detection

It's important to pay attention to the fact that the detection of the upper limit of the sheet flow is not always obvious (especially when there is a lot of transported sediments) because it is similar to a cloud of particles that does not have a perfect delimitation.

After achieving this local detection, and giving that we wanted to analyze the flow as a whole, we concatenated the images taken by the camera at different positions along the flume to obtain the interfaces along the whole length, as shown in figure 4.9 and 4.10. This way of analyzing the data is something new that we brought and that hadn't been thought of before. Moreover, it is a way that allows us to have a much larger view of the experience and not only in a local portion of the flume.

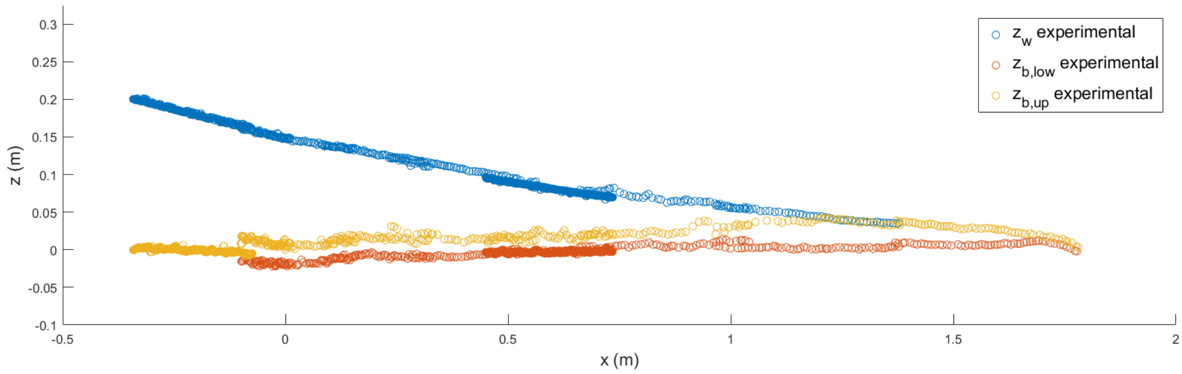

Figure 4.9: Experimental data z_w, $z_{b,low}$ and $z_{b,up}$ in function of x at time $t = 0.9s$

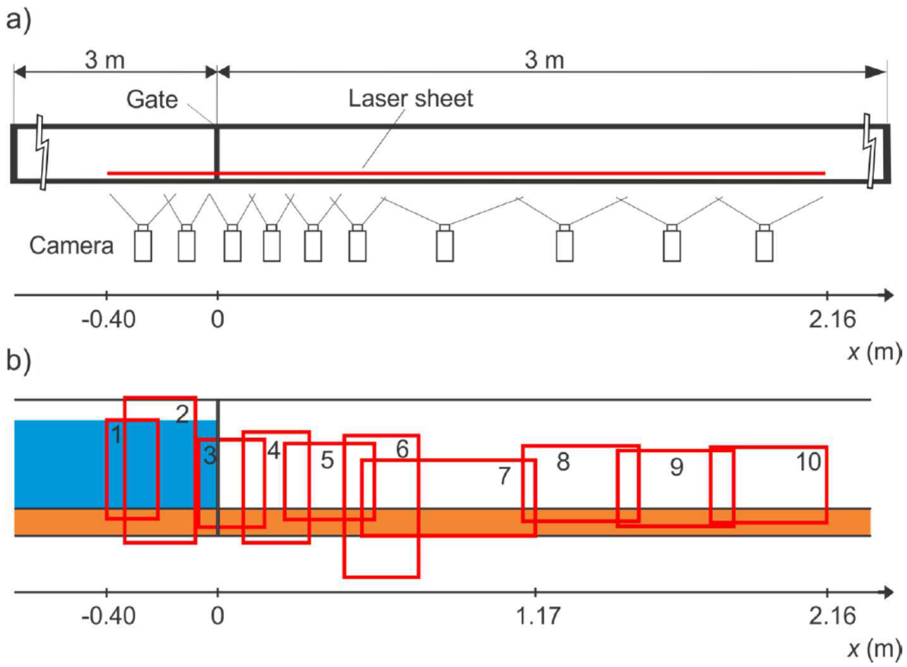

Figure 4.10: Several positions of the laser and the camera to record different areas of the event. a) map of the channel with the position of the laser sheet, b) frontal view - Reference : Thesis of Ilaria Fent, 2018

4.3 Repeatability of the experiments

One of the recorded experiments we considered in our analyses, made by Ilaria Fent, was repeated twenty-four times at the exact position of the gate (x = 0) to validate the assumption of its repeatability. She decided to introduce nondimensional forms of the variables of the flow:

- Time

$$t^{ND} = t\sqrt{g/h_0} \tag{4.2}$$

- Longitudinal coordinate

$$x^{ND} = x/h_0 \tag{4.3}$$

- Vertical coordinate

$$z^{ND} = z/h_0 \tag{4.4}$$

- Water depth

$$h^{ND} = h/h_0 \tag{4.5}$$

- Horizontal velocity

$$u^{ND} = u/\sqrt{gh_0} \tag{4.6}$$

She drew the profiles for the water surface z_w and for the bed surface z_b (that correspond to $z_{b,low}$) for the twenty-four experiments and noticed that all these repetitions showed pretty good agreement between the experimental series.

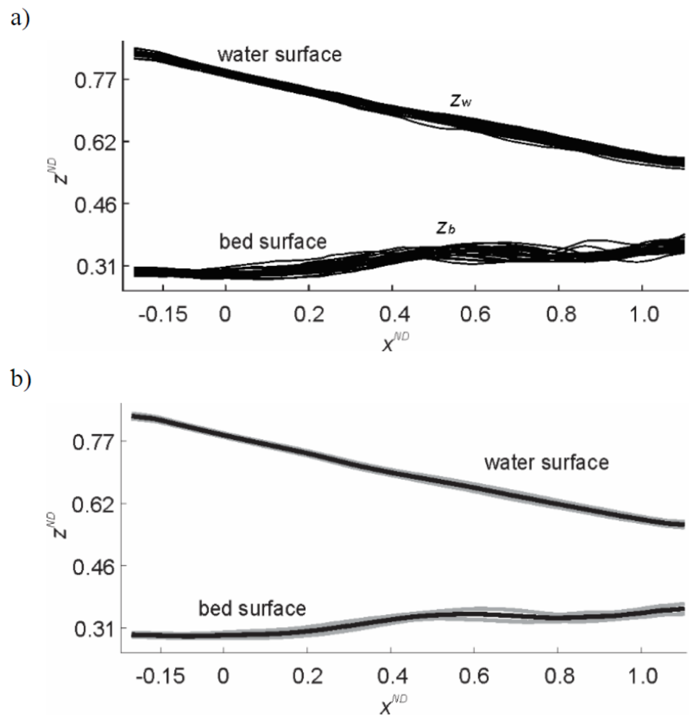

Figure 4.11: Extracted water surface and bed profiles at non-dimensional time t^{ND} = 2.20 (t = 0.4 s). a) superposition of profiles from 24 runs. b) profiles resulting from ensemble averaging over 24 runs, with the solid black line representing the averaged values and the gray zone representing the standard deviation. - Reference : Ilaria Fent's thesis (2018)

She also calculated the standard deviation of the nondimensional horizontal velocity u^{ND} as shown in figure 4.12.

She noticed that the ratio between the standard deviation and the mean value of each variable (water z_w and bed z_b surface levels and horizontal u and vertical w velocities) was less than 5%, confirming the repeatability of the event.

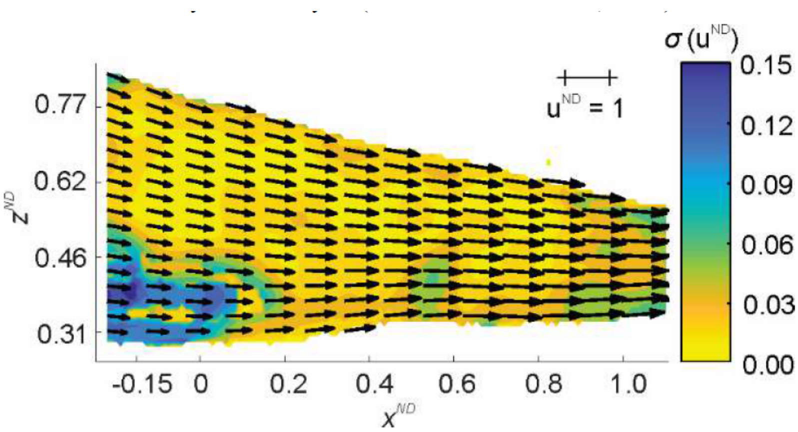

Figure 4.12: Ensemble averaged velocity field obtained by PIV method, at nondimensional time $t^{ND} = 2.20$ (t = 0.4 s). In the background is the standard deviation σ of the nondimensional horizontal velocity u^{ND}
Reference : Ilaria Fent's thesis (2018)

4.4 Moving average

The camera shoots only a small part of the 6 meters of the channel at a time (about 40 centimeters, but, of course, it varies depending on how we place the camera). In order to compare the entire flow to the associated Ritter analytic solution or to the associated numerical simulation, we wanted to juxtapose the results of all the experiments to have values for the whole channel as shown in figure 4.10. This is also useful in order to have the trend of the friction slope S_f across the channel.

We decided to use a moving average to fix several issues that happen when we work with the variation of a variable in the x-direction:

- As explained in section 4.2, we determined the water levels z_w, and the two levels associated to the transported layer $z_{b,up}$ and $z_{b,low}$ by clicking on the images. Since we click approximately, the different points do not have equidistant abscissas. The output of this process is a list of coordinates (x, z). The issue is that the x-coordinates are not the same as the abscissas given by the software DaVis when we determine the velocities. The same issue happens for the numerical simulations which have a $5cm$ step. Using a moving average can fix these problems as we can choose the abscissas.

- Some experiments overlap. We can in fact take advantage of this fact to reduce possible errors. For a given abscissa, the value of the flow characteristic (z_w, U, $z_{b,up}$ or $z_{b,low}$) will be the average (taking into account all the experiments) of this characteristic around that abscissa with a chosen radius.

- Using a moving average on the data makes the different characteristics and their respective derivatives smoother, leading to less numerical oscillations.

The principle is to evaluate for each abscissa the average of the values of the variables around that point. We decided to evaluate the variables with a $5cm$ step by averaging around each abscissa with a $10cm$ radius.

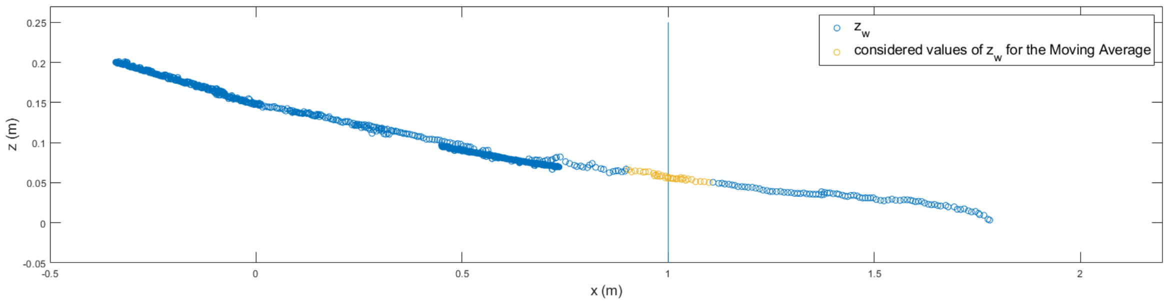

Figure 4.13: Illustration of the moving average process for $z_w(x = 1m)$ at time $t = 0.9s$

A $10cm$ radius around the abscissa seems high, but it revealed to give very satisfying results as shown in figure 4.14, where we repeated the process for the whole x-axis, for z_w, $z_{b,up}$ and $z_{b,low}$.

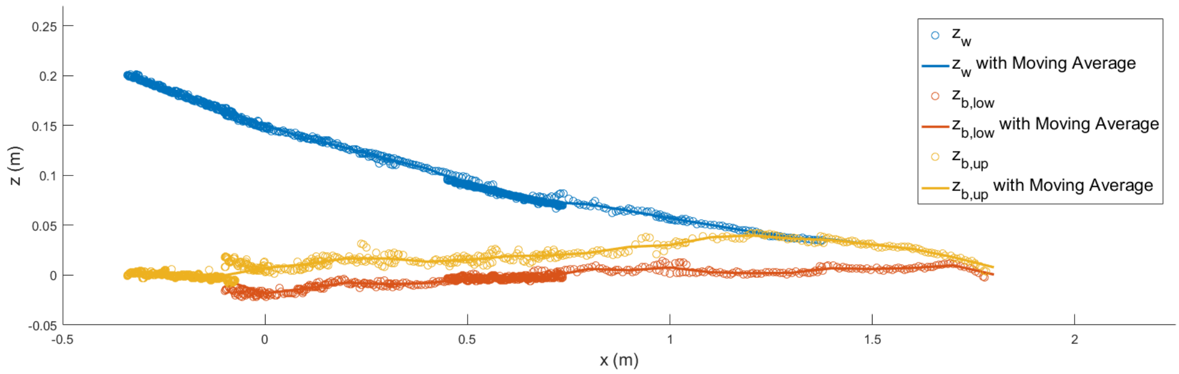

Figure 4.14: Experimental data z_w, $z_{b,low}$ and $z_{b,up}$ in function of x at time $t = 0.9s$

As said before, we only used this moving average process when working in the x-direction. We also used moving averages for the average velocity U, for the total head $\mathcal{H}$, and for the derivatives of the flow variables when they oscillate too much. We didn't use moving averages when using the vertical variation of the velocity profile for a given abscissa, as we do when we apply the Clauser method in section 5, for example.

Chapter 5

Results and analyses

In this Master's thesis, we aim to have a better understanding of the sediment transport that occurs after a dam break. To know more about it, we calculated the shear stress τ_b thanks to the methods that were presented in section 1.7. All these methods require the knowledge of the velocity profile.

In this chapter, we provide the real contribution of this work. The analyses of the different methods and our results are presented. We will see that some of the methods we use did not lead to conclusive findings, while some of them did bring interesting conclusions.

5.1 Investigation of the velocity profile found by Sumer et al. (1996)

Some of the methods presented in this chapter require to know the value of the shear velocity u_* that can be extracted from the velocity profile. In this section we explain in more details the theoretical velocity profile found by Sumer et al. (1996) (equation 5.1) and the parameters that compose it. These parameters can be modified in order to fit the theoretical profile with the experimental profile, as shown in figure 5.1.

$$u = \frac{u_*}{\kappa}\ln(z - z_{b,low} - \Delta z) + u_*\Big(B_r - \frac{1}{\kappa}\ln(k_s)\Big) \tag{5.1}$$

In this profile, the different parameters are :

- The Von Karman constant κ which we fixed at 0.407 in our experiments, but

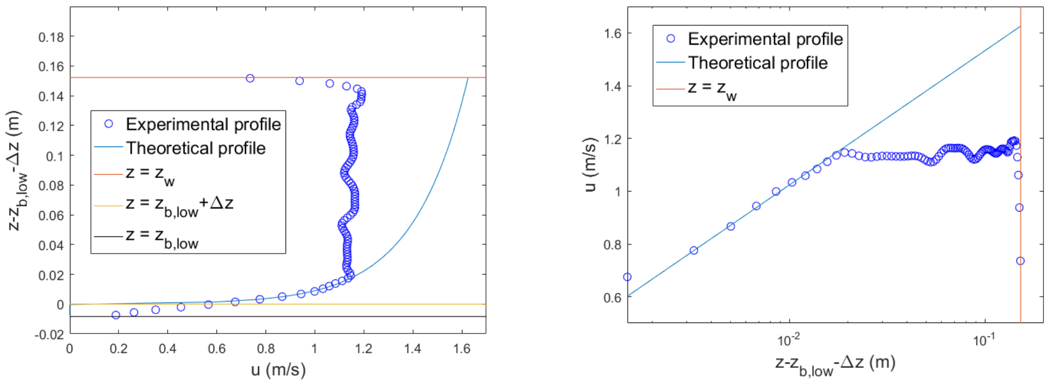

Figure 5.1: Example of our velocity profile with regular axes on the left and with logarithmic x-axis on the right

which can take other values. In the literature, values between 0.37 to 0.42 can be found.

- The bed roughness $k_s = d_{50} = 0.00172m$. The similitude between the diameter and the equivalent bed roughness is possible only if the sediments are considered uniform. This is the assumption we made. If this assumption cannot be confirmed, authors propose other approximations of equivalent bed roughness like $2d_{50}$ (Alabi), $2.5d_{50}$ (Beheshti), d_{65} (Einstein), $35d_{84}$ (Léopold et al.), ...

- The lower level of the solid transport layer $z_{b,low}$ which varies with time and space as a function of the sediment transport, and that we can determine locally from the images taken by the camera, as explained in section 4.2.

- The shear velocity u_* which varies with time and space. If we work with regular axes (figure 5.2 on the left), the effect of the variation of u_* contracts or expands the theoretical profile.
  With semi-logarithmic and inverted axes (figure 5.2 on the right), the theoretical log-law profile becomes linear, and as a consequence the effect of the variation of u_* is to affect the slope of the theoretical profile.
  We can compare figures 5.1 and 5.2 to understand this modification.

- Δz which also varies with time and space. As a reminder, Δz corresponds to the theoretical level from $z_{b,low}$ towards which the velocity logarithmic law tends asymptotically. It's important to know that in our analyses, we fix the reference level at $z_{b,low} + \Delta z$. If we work with regular axes (figure 5.3 on the left), the effect of the variation of Δz is to shift vertically the theoretical profile compared to the experimental one.

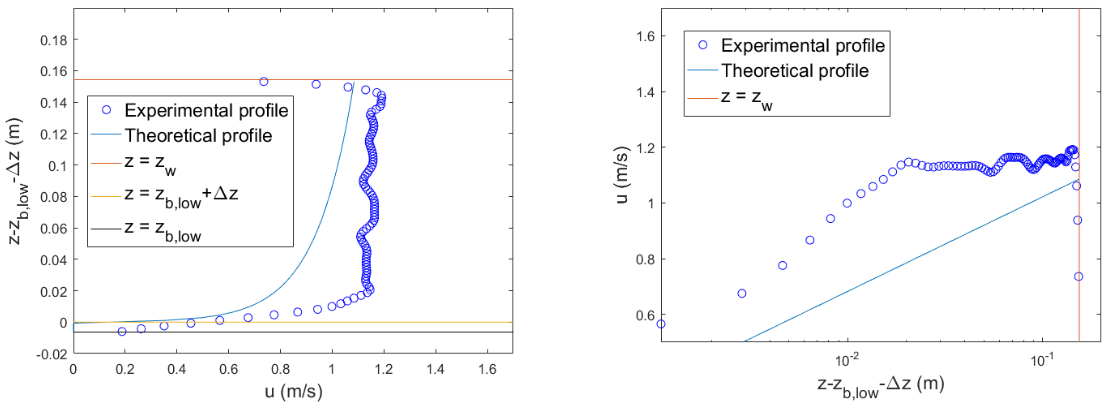

Figure 5.2: Qualitative example of the effect of the diminution of u_* on the velocity profile that we can compare with figure 5.1

With semi-logarithmic and inverted axes (figure 5.3 on the right), the effect of Δz is to modify the reference level. The consequence is a horizontal shift of the experimental profile that contracts or expands itself due to the logarithmic scale.

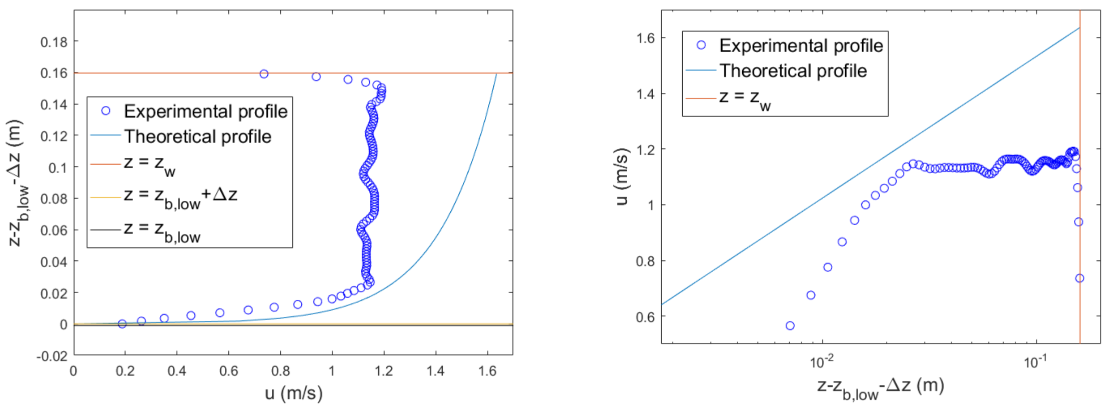

Figure 5.3: Qualitative example of the effect of the diminution of Δz on the velocity profile that we can compare with figure 5.1

This way, we can notice and remind that if we want to match the slope of the theoretical and the experimental profiles in semi-logarithmic scale, we have to take account of both u_* and Δz.

Another difficulty lies in the fact that it is not easy to find the exact portion of the experimental profile that is actually logarithmic. When fitting visually the theoretical equation to the experimental profile, it seems that there is more than one appropriate couple (Δz, u_*). In other words, for any Δz, there is a u_* that can give a good visual fitting as shown in figure 5.4. Therefore, it's more interesting to correctly fix one of these two parameters and to play with the variation of the other one as we try in the next sections.

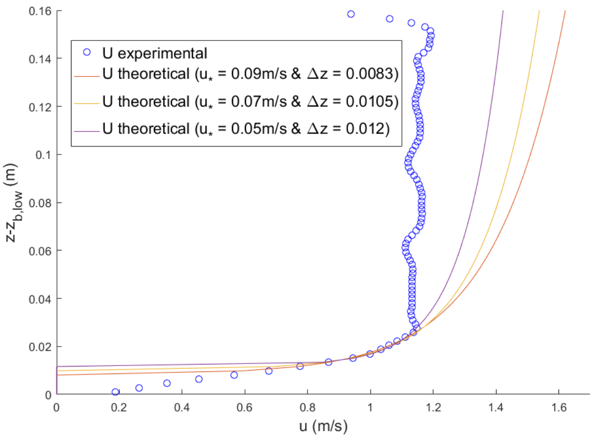

Figure 5.4: Experimental velocity profile with theoretical profiles designed by 3 different couples $u_* - \Delta z$

- B_r which varies with time and space. If we work with regular axes (figure 5.5 on the left), the effect of the variation of B_r is to shift horizontally the theoretical profile compared to the experimental one.

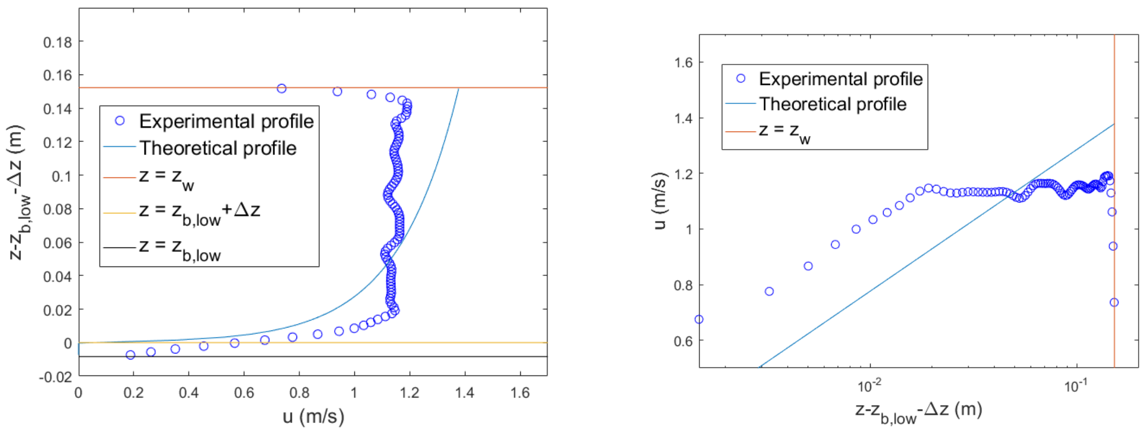

Figure 5.5: Qualitative example of the effect of the diminution of B_r on the velocity profile that we can compare with figure 5.1

With semi-logarithmic and inverted axes (figure 5.5 on the right), the effect of the variation of B_r is to shift vertically the theoretical profile compared to the experimental one (while keeping the good slope).

5.2 Clauser method (using the $\Delta z - u_*$ relation proposed by Sumer et al.)

This method is based on the following formula :

$$\tau_b = \rho u_*^2 \tag{5.2}$$

where the shear velocity u_* clearly appears and we will find its value by fitting the theoretical profile found by Sumer et al. (equation 5.1) with the experimental profile. But as said in section 5.1, it can be interesting to fix beforehand Δz in order to restrain us at only one degree of freedom and to find only one value of u_*. This is why, for this method, we choose to refer to previously presented figure produced by Sumer et al. where they put in relation Δz and u_* (which appears in the abscissa in the Shields parameter $\theta = \frac{u_*^2}{g(s-1)d}$) as shown in figure 5.6.

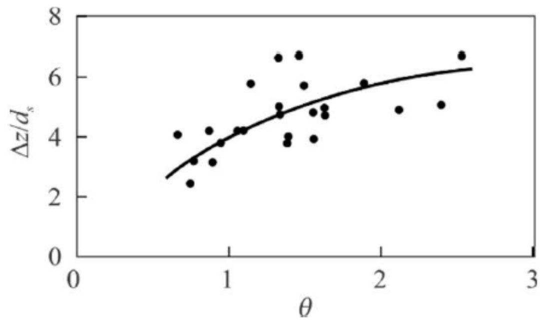

Figure 5.6: Level of the theoretical bed Δz as a function of θ
Reference : Sumer et al. (1996)

By making a logarithmic approximation on the points (solid line in figure 5.6), we find the equation :

$$\frac{\Delta z}{d_{50}} = 0.9937 \ln(\theta) + 6.0996 \tag{5.3}$$

Using this equation, every time we change the value of u_* implies that θ and Δz will automatically be adapted to each other. We try different values of u_* by trial and error approach until the slope of theoretical profile fits with the experimental one.

Once the slope is the good one, we change the value of B_r in order to vertically shift the theoretical profile on the experimental one. The experimental points that fit with the theoretical ones are filled in red in figure 5.7 where results for time 0.7s, 0.9s, 1.1s and 1.3s at the position of the gate (x=0) are shown.

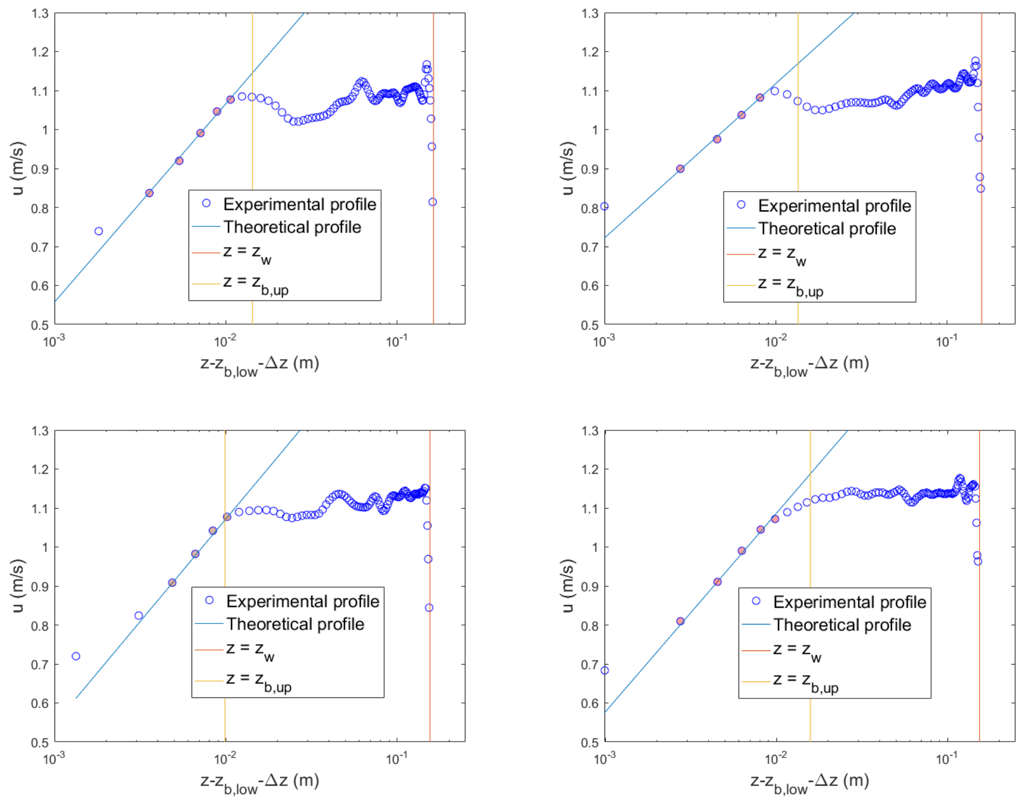

Figure 5.7: Theoretical velocity profiles fitted on the experimental ones for times t = 0.7s (on the top left), t = 0.9s (on the top right), t = 1.1s (on the lower left) and t = 1.3s (on the lower right) at the gate's position x = 0 m

The different parameters found for all these times at positions 0.0, 0.2, 0.5, 1.0 and 1.5 m are shown in table 5.1.

On the penultimate column, r is the ratio between the absolute position of the higher red experimental point "z_h" that fits on the theoretical profile, divided by the absolute $z_{b,up}$ position.

$$r = \frac{z_h - z_{b,low}}{z_{b,up} - z_{b,low}} \tag{5.4}$$

x(m)	t(s)	z_w(m)	$z_{b,up}$(m)	$z_{b,low}$(m)	Δz(m)	u_*(m/s)	Br(-)	θ(-)	r(-)	τ_b(Pa)
0.0	0.7	0.1517	0.0032	-0.0194	0.0083	0.09	7.52	0.285	0.839	8.1
	0.9	0.1483	0.0032	-0.0178	0.0075	0.07	11.65	0.173	**0.742**	4.9
	1.1	0.1444	-0.0007	-0.0191	0.0085	0.093	7.3	0.305	1.016	8.649
	1.3	0.1455	0.0073	-0.0168	0.0083	0.09	7.75	0.285	0.753	8.1
0.2	0.7	0.1162	0.0197	-0.0086	0.0094	0.122	6.75	0.524	0.886	14.884
	0.9	0.1271	0.0152	-0.0054	0.0088	0.103	8.85	0.374	0.923	10.609
	1.1	0.1331	0.0118	-0.0106	0.0099	0.142	3.52	0.710	1.209	20.164
	1.3	0.1350	0.0155	-0.0091	0.0096	0.13	4.7	0.595	0.921	16.9
0.5	0.7	0.0751	0.0212	-0.0011	0.0060	0.045	37.55	0.071	0.775	**2.025**
	0.9	0.0896	0.0182	-0.0061	0.0084	0.092	12.3	0.298	0.917	8.464
	1.1	0.1042	0.0120	-0.0044	0.0084	0.092	12.45	0.298	**1.254**	8.464
	1.3	0.1131	0.0084	-0.0090	0.0090	0.108	7.35	0.411	1.192	11.664
1.0	0.7	-	-	-	-	-	-	-	-	-
	0.9	0.0557	0.0237	0.0017	0.0083	0.0875	20.65	0.270	0.771	7.656
	1.1	0.0742	0.0199	0.0032	0.0080	0.082	18.8	0.237	1.118	6.724
	1.3	0.0879	0.0212	-0.0009	0.0085	0.095	12.3	0.318	1.177	9.025
1.5	0.7	-	-	-	-	-	-	-	-	-
	0.9	-	-	-	-	-	-	-	-	-
	1.1	0.0518	0.0227	0.0007	0.0104	0.165	8.95	0.959	0.847	27.225
	1.3	0.0662	0.0227	-0.0014	0.0107	0.18	6.05	1.142	0.860	**32.4**

Table 5.1: Evolution of the variables needed in the velocity distribution study and determination of r and τ_b - The empty cells correspond to times and spaces where the flow is not yet present or very next to the front (The relative graphs for each position are shown on Appendix C)

This ratio r is between 0.742 and 1.254 showing that the theoretical velocity profile is, at every time, relatively close to the position of the upper limit of the sheet-flow layer $z_{b,up}$. However, it must be kept in mind that, as explained in subsection 4.2, $z_{b,up}$ is the upper limit of the sheet-flow layer, which is a cloud so it's difficult to manually determine a precise value of this level.

The last column displays the calculated shear stress $\tau_b = \rho u_*^2$ which was the first objective of our Master's thesis. We find values between 2.025 Pa and 32.4 Pa.

The couples (Δz, $\theta(u_*)$) obtained with this method are shown on the graph ($\frac{\Delta z}{d_{50}} - \theta$) of Sumer et al. in figure 5.8.

This method gives us values of the bed shear stress τ_b that have the same magnitude as the values found in the Ilaria Fent's thesis as we showed in subsection 2.6.1, where she found τ_b between 5 and 15 Pa. It's good news to find similar values with a different method than hers. However, our method is based on the relation between Δz and $\theta(u_*)$ found by Sumer et al. working on a steady flow. So, it could be too big a step to consider that the curve of their equation 5.3 is applicable on

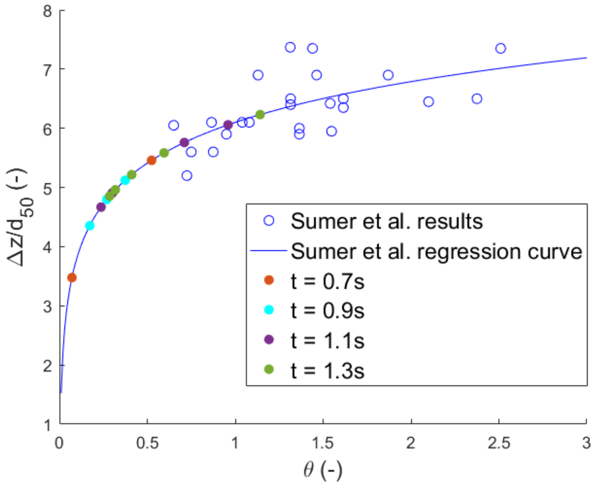

Figure 5.8: Experimental level of the theoretical bed Δz as a function of θ + Results of Sumer et al. (1996) figure 5.6

our analysis.

In order to see if it is an over-estimation, we now compare these results with other methods.

5.3 Clauser method (using parametric optimization)

Instead of using the experimental results of Sumer et al. to limit our choices of u_* and Δz, it is possible to freely optimize the parameters u_* and Δz to best fit the equation of the profile of Sumer et al. (equation 5.5) to the experimental data.

$$u = \frac{u_*}{\kappa} \ln\Big(z - z_{b,low} - \Delta z\Big) + u_*\Big(B_r - \frac{1}{\kappa}\ln(k_s)\Big) \tag{5.5}$$

The idea is to find the values of A, B and C that optimize the following equation in terms of the least squares criterion:

$$u = A\ln(z' - B) + C \tag{5.6}$$

where $z' = z - z_{b,low}$, $A = \frac{u_*}{\kappa}$, $B = \Delta z$ and $C = u_*\Big(B_r - \frac{1}{\kappa}\ln(k_s)\Big)$

This idea did not work, probably due to the logarithm that does not admit negative values. This can block the iterations for Δz. An upper bound for the parameter B could probably be specified in the algorithm to fix this problem.

We almost gave up on this idea until we noticed that Ferreira et al. (2012) used another formulation: the equivalent differential equation.

$$u_* \left(\frac{du}{dz}\right)^{-1} = \kappa(z' - \Delta z) \tag{5.7}$$

The idea is then to find the values of A and B that optimize the following equation in terms of the least squares criterion:

$$\frac{du}{dz} = \frac{A}{\kappa(z' - B)} \tag{5.8}$$

where $A = u_*$ and $B = \Delta z$

Ferreira et al. (2012) only optimized one of the two parameters (Δz) because they used the Slope method to determine u_* but it is worth wondering if they could have optimized both at the same time.

At first, this formulation looked particularly interesting for several reasons. First, this formulation does not require the knowledge of k_s and B_r. Furthermore, the equation does not have any logarithm. The algorithm can run without the specification of any bound. Also note that it is not a 3-variable optimization but a 2-variable optimization.

The first step is to calculate the derivative of the velocity $\frac{du}{dz}$. This is done in two different ways:

- Using the Explicit Euler Method:

$$\frac{dy(x)}{dx} = \frac{y(x+h) - y(x)}{h} \tag{5.9}$$

- Using the centered differencing formula:

$$\frac{dy(x)}{dx} = \frac{y(x+h) - y(x-h)}{2h} \tag{5.10}$$

The two concavities we can observe on the red line (figure 5.9 on the left) and the peak of the derivative (figure 5.9 on the right) prove that there is an inflection point, leading to the conclusion that the profile designed by Ilaria Fent based on the analysis of Sumer et al. (1996) (figure 2.4) should be adapted for our case as

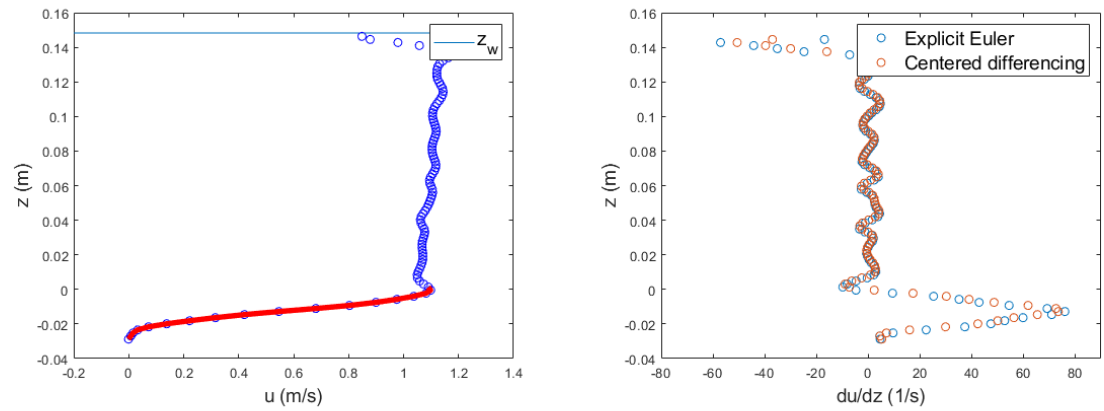

Figure 5.9: On the left : Experimental velocity profile for time $t = 0.9s$ at the position of the gate $x = 0m$
On the right: Derivative of the velocity calculated using two methods

can be seen in figure 5.10, in green. Note that the profile could also be adapted to consider the fact that the velocity drops near the water level due to the effects of air friction.

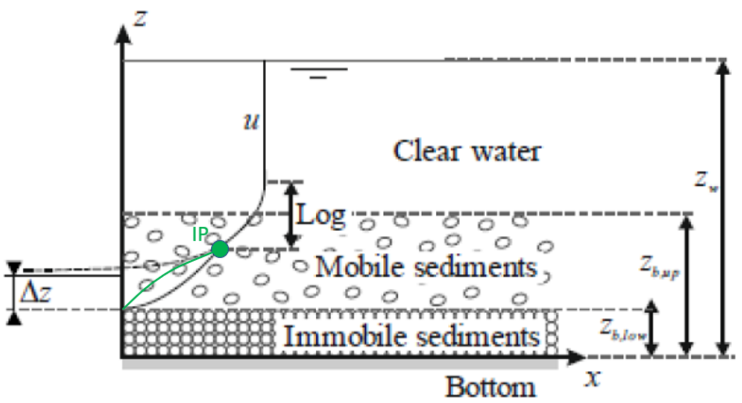

Figure 5.10: Adaptation of the general velocity profile to take the inflection point into account

This inflection point is particularly interesting. It could mean that right after the maximum of the derivative $\frac{du}{dz}$, begins the logarithmic part of the profile, as represented in yellow in figure 5.11. If it is actually the case, this would be helpful to easily find the part of the experimental profile that will be used during the optimization. As explained earlier, finding the portion that is actually logarithmic is decisive.

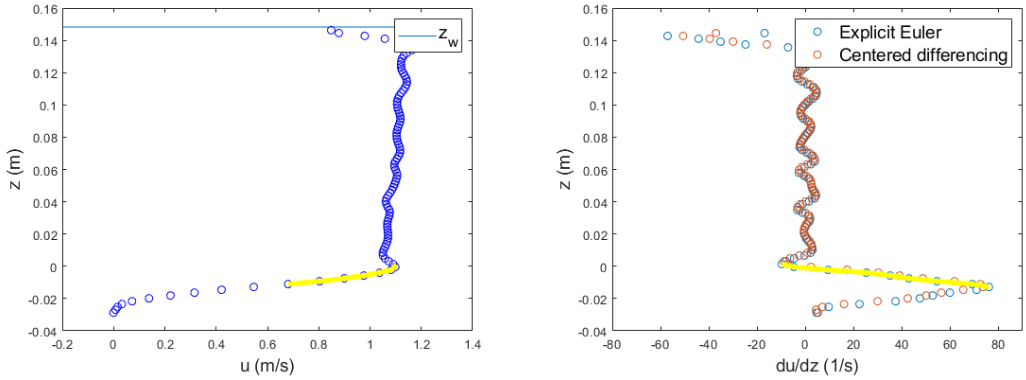

Figure 5.11: In yellow, the part of the derivative right after the maximum (8 points).

We use a least-squares algorithm with a termination tolerance on the function value $(\frac{du}{dz})$ equal to 10^{-6}. Trying to fit equation 5.8 to this part of the derivative profile leads to $u_* = 1.8 * 10^{-5} m/s$ and $\Delta z = 0.0085$ using the Explicit Euler definition and to $u_* = 9.64 * 10^{-4} m/s =$ and $\Delta z = 0.0084$ using the Centered differencing definition. These results are aberrant as can be seen graphically in figure 5.12.

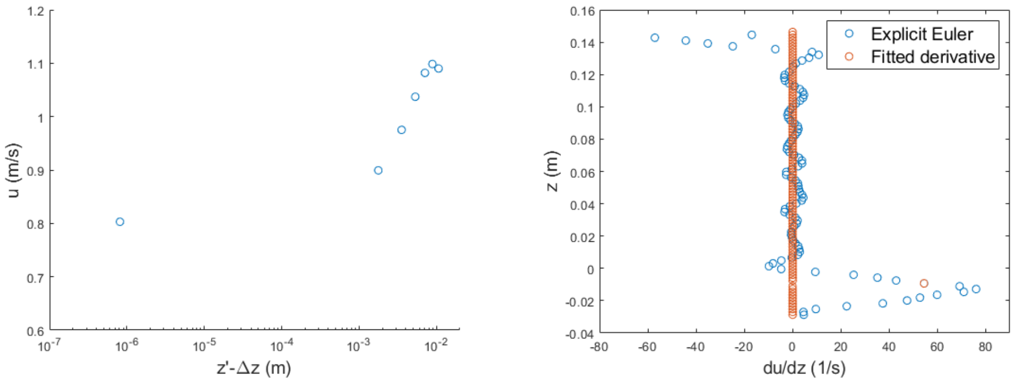

Figure 5.12: First try with the Explicit Euler method. - On the left : Experimental velocity profile of the points that are in the yellow part of figure 5.11. On the right: Comparison between the fitted derivative (equation 5.8) and the derivative calculated using the Explicit Euler method

Note that in the left figure, as the x-axis is logarithmic, the points with $z' - \Delta z \leq 0$ cannot be displayed. Only one point is affected by this problem here. This is why there are only 7 points in figure 5.12 instead of 8.
The left figure is particularly useful: if we remember equation 5.1, the representation of the logarithmic part in a semi-logarithmic graph with abscissa $z' - \Delta z$ should

be a line. It is clearly not the case, so it means that some extreme points are not on the logarithmic part of the profile and should not be taken into account in the optimization. Unfortunately, it also means that our assumption that the yellow part of figure 5.11 corresponds to the logarithmic part is not verified. In figure 5.12 on the right, we expect the fitted derivative to look like the yellow part of figure 5.11. This is clearly not the case.

After that first attempt, we decide to keep successively 5, 4 and 3 out of the 8 points to observe the variability of the results (cf. figure 5.13).

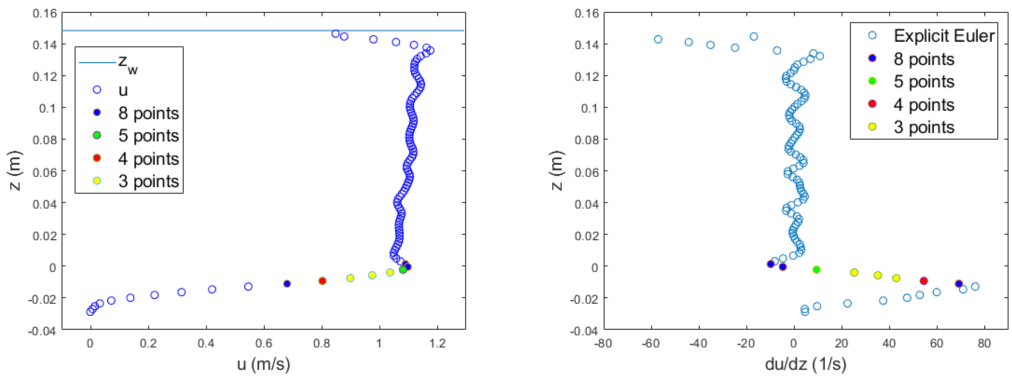

Figure 5.13: The points we will keep for the example optimization. The figure on the right could also be obtained for the Centered differencing method.

The result obtained with 5 points is illustrated in figure 5.14. The left graph shows that the five points seem much more aligned and the right graph shows that the fitted derivative follows much more the falling part of the explicit Euler derivative than in figure 5.12.

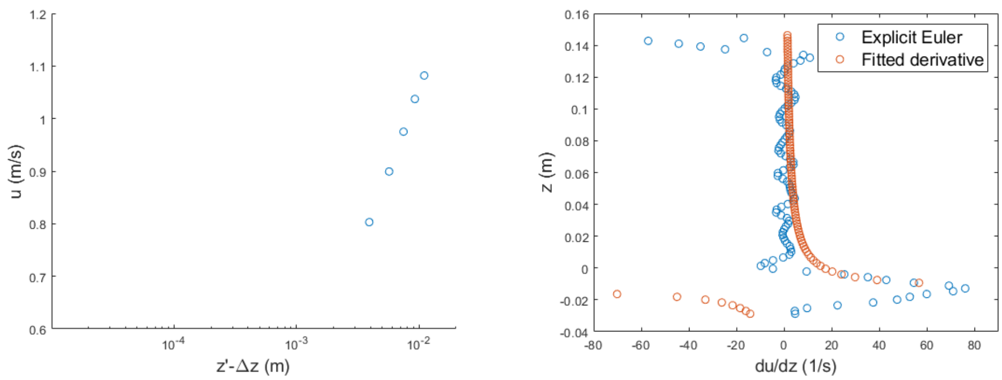

Figure 5.14: Example using 5 points. - On the left : The experimental velocity profile looks linear. - On the right: On the previously yellow portion, the fitted derivative looks more like the Explicit Euler derivative than in figure 5.9

The results obtained with the other numbers of points are shown in the following table and the corresponding graphs are available in Appendix D.

	Explicit Euler		Centered differencing	
Points	u_*	Δz	u_*	Δz
8 points	$1.8 * 10^{-5}$	0.0085	$9.64 * 10^{-4}$	0.0084
5 points	0.09	0.0046	0.116	0.004
4 points	0.1217	0.0031	0.01413	0.0029
3 points	0.1005	0.0046	0.12	0.0042

Table 5.2: Results of the parametric optimization for several choices of number of points and for the two derivative calculation method. (Cf. figures illustrated in Appendix D for all these profiles)

We can also make a quick analysis of the sensitivity of the process. We keep the values found with the Explicit Euler method with three points and we note them $(u_*^\circ, \Delta^\circ z)$. In table 5.3, we slightly modify u_*° or $\Delta^\circ z$ and see how the other parameter adapts to this change in an optimization (in **bold**, the adapted value):

	u_*	Δz
$u_*^\circ, \Delta^\circ z$	0.1005	0.0046
$u_*^\circ + 0.001, \Delta^\circ z$	0.1015	**0.0045**
$u_*^\circ + 0.01, \Delta^\circ z$	0.1105	**0.0039**
$u_*^\circ + 0.1, \Delta^\circ z$	0.2005	**-0.0021**
$u_*^\circ, \Delta^\circ z + 0.0001$	**0.0989**	0.0047
$u_*^\circ, \Delta^\circ z + 0.001$	**0.0852**	0.0056
$u_*^\circ, \Delta^\circ z + 0.01$	**-0.0124**	0.0146

Table 5.3: Quick sensitivity analysis

We start to feel than even if we find one of the two values with another method, the method will have to be reliable for the second value to be accurate.
This sensitivity would definitely be less important with more experimental velocity points on the logarithmic portion.

We can conclude by saying that the perfect couple (u_*,Δz) is difficult to find by optimization as it depends on the choice of the points used for the optimization, which is difficult to make perfectly.
This is probably the reason why Sumer et al. (1996) and Ferreira et al. (2012), for example, both fixed u_* using the Slope method before fixing Δz by parametric optimization.

It is also normal to have such differences between the Explicit Euler method and the Centered differencing because we use very few points for the derivative calculations.

We make a few recommendations in the Conclusion section if the next generations want to work on this method with new ideas.

5.4 Slope method

The slope method presented previously in subsection 1.7.2 is applied in this section with our experimental data. As a reminder, the formula we use in order to find the bed shear stress is

$$\tau_b = \gamma R S_f \tag{5.11}$$

where $\gamma = 9810 N/m^3$, R is the hydraulic radius and S_f is the friction slope.

5.4.1 Determination of the hydraulic radius R

In the case of our experiments, given that we use smooth glass for the vertical walls, we make the assumption that the friction on these walls can be neglected: it means that the Manning coefficients related to the walls $n_w = 0$ (even though they are not perfectly frictionless). Therefore, we can assume that the only Manning coefficient n that remains is the bed one that corresponds, for our kind of sediments, to $n_b = 0.0165$ (based on other experiments made with the same sand). Therefore we use the bed hydraulic radius R_b in equation 5.11. This is summarized in the following figure.

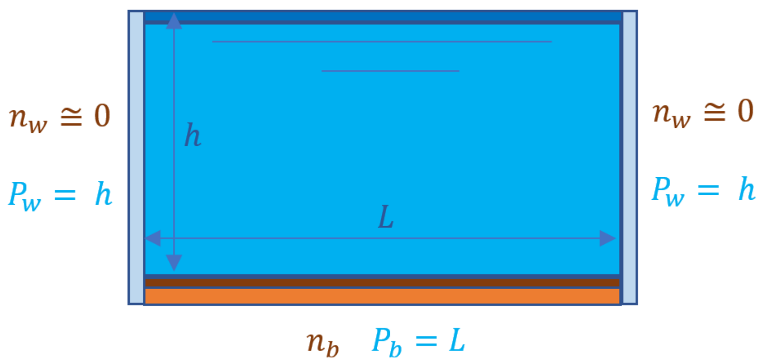

Figure 5.15: Rectangular cross-section of a flume

Moreover, based on equations 1.16 and 1.18 seen in section 1.3 and adapted for rectangular flume with frictionless vertical walls, we have :

$$n = \left(\frac{n_b^{3/2} P_b}{P}\right)^{2/3} = n_b \left(\frac{P_b}{P}\right)^{2/3} \quad \rightarrow \quad \frac{n_b}{n} = \left(\frac{P}{P_b}\right)^{2/3} \tag{5.12}$$

and

$$R_b = R\left(\frac{n_b}{n}\right)^{3/2} \tag{5.13}$$

By joining these two equations, we have :

$$R_b = R\frac{P}{P_b} = \frac{A}{P}\frac{P}{P_b} = \frac{A}{P_b} = \frac{Lh}{L} = h \tag{5.14}$$

This way, the bed hydraulic radius R_b is approximately equal to the flow depth h and equation 5.11 becomes

$$\tau_b = \gamma h S_f \tag{5.15}$$

5.4.2 Experimental analysis of the friction slope S_f

Now let us introduce the way we find S_f. As seen in subsection 1.7.2, different authors determined S_f with specific hypotheses:

$$S_{f,Manning} = U^2 n^2 R^{-4/3} \tag{5.16}$$

$$S_{f,unsteady} = -\frac{\partial \mathcal{H}}{\partial x} + \frac{1}{U}\frac{\partial H}{\partial t} \tag{5.17}$$

$$S_{f,MOM} = -\frac{1}{gh}\frac{\partial q}{\partial t} - \frac{U^2}{gh}\frac{\partial h}{\partial x} - 2\frac{U}{g}\frac{\partial U}{\partial x} - \frac{\partial z_w}{\partial x} \tag{5.18}$$

$$S_{f,SG} = -\frac{1}{gh}\frac{\partial q}{\partial t} + 2\frac{U}{gh}\frac{\partial h}{\partial t} + \frac{U^2}{gh}\frac{\partial h}{\partial x} - \frac{\partial z_w}{\partial x} \tag{5.19}$$

$$S_{f,ML} = -\frac{1}{gh}\frac{\partial q}{\partial t} + 2\frac{U}{gh}\frac{\partial z_w}{\partial t} + \frac{U^2}{gh}\frac{\partial h}{\partial x} - \frac{\partial z_w}{\partial x} \tag{5.20}$$

$$\begin{aligned} S_{f,SS} = -\frac{1}{gh}\Bigg[&\frac{\partial q}{\partial t} + 2Uh\frac{\partial U}{\partial x} + U^2\frac{\partial h}{\partial x} + gh\frac{\partial z_w}{\partial x}\left(\left(\frac{\partial z_b}{\partial x}\right)^2 + 1\right)^{-1} \\ &-gh^2\frac{\partial z_b}{\partial x}\frac{\partial^2 z_b}{\partial x^2}\left(\left(\frac{\partial z_b}{\partial x}\right)^2 + 1\right)^{-2}\Bigg] \end{aligned} \tag{5.21}$$

$$S_{f,CH} = -\frac{1}{gh}\left[\frac{\partial q}{\partial t} + 2Uh\frac{\partial U}{\partial x} + U^2\frac{\partial h}{\partial x} + gh\frac{\partial z_w}{\partial x} + 2Uh\left(\frac{\varepsilon_1}{2} + \frac{\varepsilon_2}{3}\right)\frac{\partial U}{\partial x}\right.$$
$$\left. +U^2\left(\frac{\varepsilon_1}{2} + \frac{\varepsilon_2}{3}\right)\frac{\partial h}{\partial x} + U^2 h\left(\frac{1}{2}\frac{\partial \varepsilon_1}{\partial x} + \frac{1}{3}\frac{\partial \varepsilon_2}{\partial x}\right) + \frac{1}{2}U^2(2\varepsilon_1 + \varepsilon_2)\frac{\partial z_b}{\partial x}\right] \quad (5.22)$$

The friction slope S_f is a parameter that varies with time and space. Therefore, to calculate these formulas, we need to know, at each time and everywhere, different values like the average velocity U, the water level z_w and the bed level z_b (the other parameters $\mathcal{H}$, h, q, H, $\varepsilon_{1,2}$ are functions of them).

Thanks to the high-speed camera available in the laboratory, both Ilaria Fent and us collected experimental data. Figures 5.16, 5.17 and 5.18 represent the required characteristics of the flow for a sample of our data at time $t = 0.9s$. As the camera only captures a small part of the channel during an experiment, it is important to remind that we made these graphs by juxtaposing the results of several experiments, assuming the repeatability of the experiment. As explained in subsection 4.2, it is also good to remind that the values $z_{b,low}$, $z_{b,up}$ and z_w were detected manually and can comport some little inaccuracies.

Thanks to these values, we can now compute the different friction slopes S_f. As we can see in equations 5.16 to 5.22, only the first equation $S_{f,Manning}$ is easy to compute as this equation does not include any derivative. The other equations require the calculation of the numerical derivatives of the experimental data. As explained in subsection 4.4, we use moving averages to smooth our experimental data in order to make the derivatives more regular.

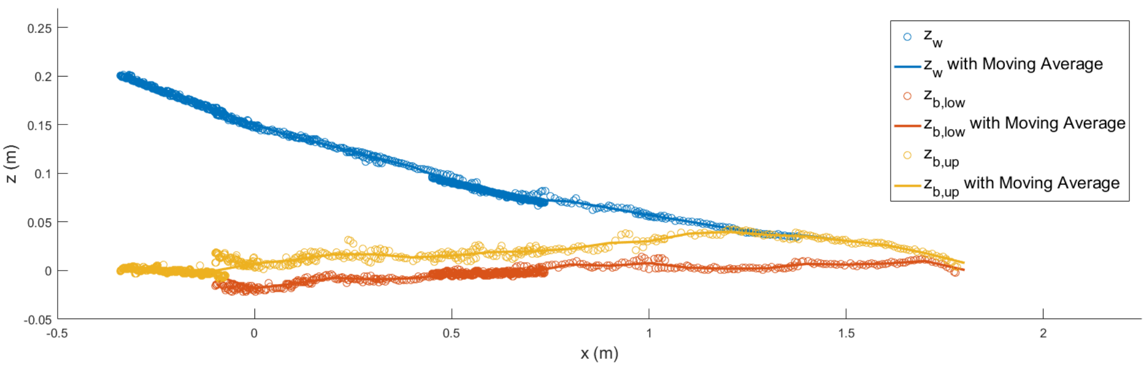

Figure 5.16: Experimental data z_w, $z_{b,low}$, $z_{b,up}$ and their moving average as a function of x at time $t = 0.9s$

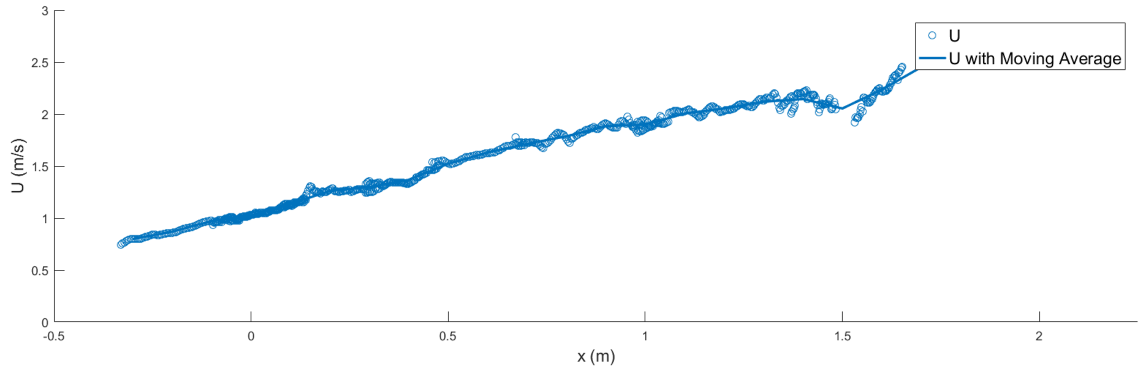

Figure 5.17: Experimental data U and its moving average as a function of x at time $t = 0.9s$

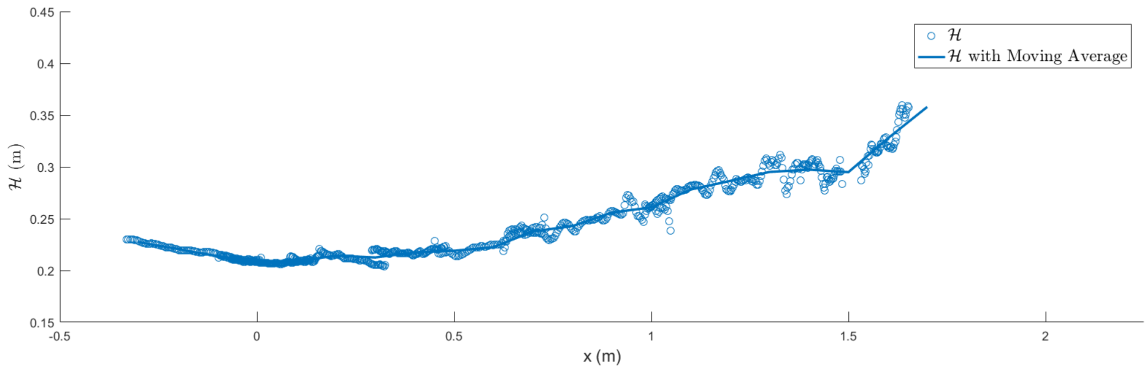

Figure 5.18: Experimental data $\mathcal{H}$ and its moving average as a function of x at time $t = 0.9s$

We use central differencing to make the numerical derivatives. So the derivative terms in equations 5.17 to 5.22 become :

$$\frac{\partial F(x,t)}{\partial x} = \frac{F(x+\Delta x,t) - F(x-\Delta x,t)}{2\Delta x} \tag{5.23}$$

$$\frac{\partial F(x,t)}{\partial t} = \frac{F(x,t+\Delta t) - F(x,t-\Delta t)}{2\Delta t} \tag{5.24}$$

$$\frac{\partial^2 F(x,t)}{\partial x^2} = \frac{F(x+\Delta x,t) - 2F(x,t) + F(x-\Delta x,t)}{(\Delta x)^2} \tag{5.25}$$

$$\frac{\partial^2 F(x,t)}{\partial t^2} = \frac{F(x,t+\Delta t) - 2F(x,t) + F(x,t-\Delta t)}{(\Delta t)^2} \tag{5.26}$$

$$\frac{\partial^2 F(x,t)}{\partial t \partial x} = \frac{F(x+\Delta x, t+\Delta t) + F(x,t) - F(x+\Delta x, t) - F(x, t+\Delta t)}{\Delta t \Delta x} \quad (5.27)$$

where F is used to denote every kind of flow characteristic.

We use $\Delta x = 0.05m$ and $\Delta t = 0.02s$ (which corresponds to 100 images). This choice gave us the results with the most stable trend as smaller steps give more numerical oscillations.

The different values of S_f as a function of x for time $t = 0.9s$ are shown in figure 5.19. We can observe that:

- Only $S_{f,Manning}$ has a regular shape.
- $S_{f,unsteady}$ is totally different from the others.
- The other values of S_f looks irregular, due to the calculation of the derivatives which compose them, but these values of S_f seem to oscillate around $S_{f,Manning}$ and they have the same order of magnitude.

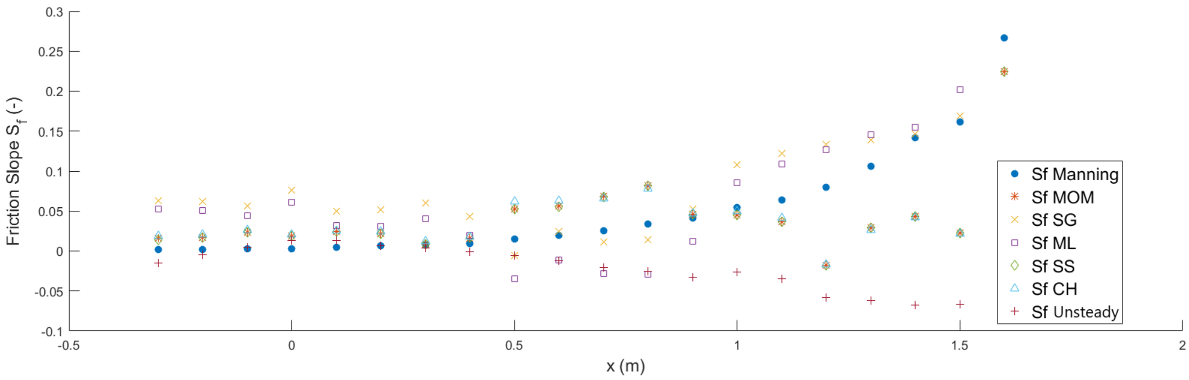

Figure 5.19: Experimental S_f as a function of x for time $t = 0.9s$

At that stage, we cannot make any conclusion about which value of S_f we have to take to compute the equation 5.11, but in the next subsections, we try to analyze these S_f formulas on analytical and numerical data in order to have a better understanding and to test our methods on data with no experimental error.

5.4.3 Comparison with Ritter's analytical solution

As presented in Section 2.5, Ritter (1982) gave the first analytical solution of the dam-break problem over frictionless bed by solving the shallow water equations (equations 1.24 and 1.25) on frictionless bed.

The analytical solution is given by:

$$\frac{U(x,t)}{c_0} = \frac{2}{3}\Big(1 + \frac{x}{c_0 t}\Big) \tag{5.28}$$

$$\frac{c(x,t)}{c_0} = \frac{\sqrt{gh}}{\sqrt{gh_0}} = \sqrt{\frac{h}{h_0}} = \frac{2}{3}\Big(1 - \frac{1}{2}\frac{x}{c_0 t}\Big) \tag{5.29}$$

Equation 5.29 shows that if we choose a time t and an initial water depth in the reservoir h_0 (in the case of our experiments $h_0 = 0.325m$), we can obtain the flow depth h ($= z_w$ since $z_b = 0$) and the average velocity U. The total head $\mathcal{H}$ can also be obtained from h and U using equation 1.4, assuming $\alpha = 1$.

By then, we have everything we need to calculate the friction slope S_f and to test our methods. Note that in this analytical case, we can use the analytical derivatives and therefore obtain continuous values of S_f.

It may seem pointless to want to calculate S_f with this analytical solution as the initial assumption is that the bed is frictionless, leading to a friction slope S_f equal to zero. But we decided to give it a try in order to see if, indeed, all the methods of calculation of S_f were well-designed. This way, if a method gives us a friction slope S_f different from zero, this will mean that it was poorly-designed and that we will have to reject it for our analysis.

In figure 5.20 we can clearly see that all S_f methods are equal to zero except $S_{f,unsteady}$. This way, we decide to reject this method.

As the other methods (except $S_{f,Manning}$) are derived from the shallow-water equations, it is not surprising, but reassuring, that they lead to $S_f = 0$. Obviously, $S_{f,Manning} = 0$ since the frictionless bed assumption is equivalent to the use of $n = 0$. Rejecting $S_{f,unsteady}$ is comforting given that experimental $S_{f,unsteady}$ had a different shape than the other S_f in figure 5.19.

Unfortunately, after trying to find a physical reason why this $S_{f,unsteady}$ was not

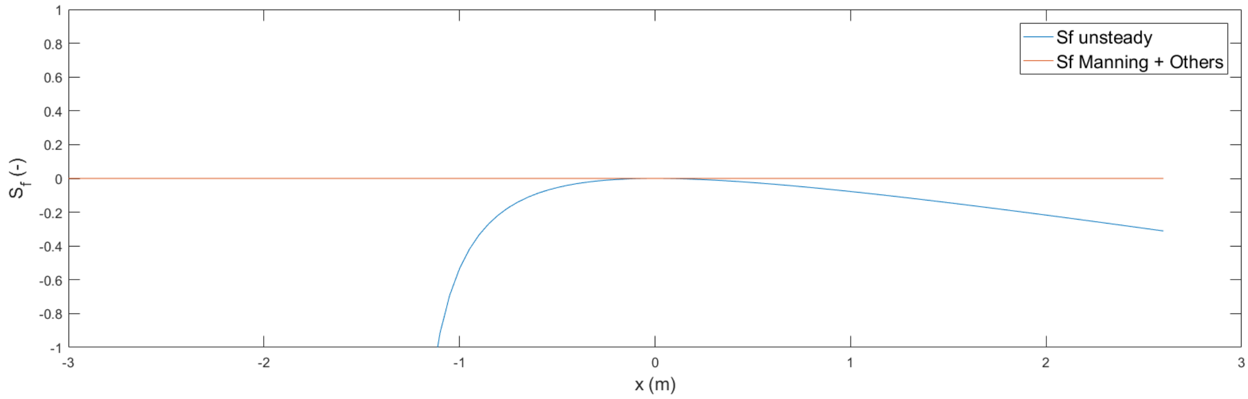

Figure 5.20: Analytic S_f as a function of x for time $t = 0.9s$

equal to zero, we did not manage to find a good one.
However, we did notice that the $S_{f,unsteady}$ curve tended to flatten with time.

5.4.4 Comparison with numerical simulations

Still with the aim of testing our methods to calculate the friction slope S_f on data with no experimental error, we were provided with the SVE2DBF code in order to realize numerical simulations of our dam-break flow. This software is a finite-volume model developed by Pr. Sandra Soares Frazao and improved by many students after her.

The simulation uses the Saint-Venant-Exner (SVE) model: a coupling of the shallow-water equations and the Exner equation. We explained this combination in section 1.6, but as a reminder, the shallow-water equations are the continuity equation (equation 1.24) and the momentum equation (equation 1.25), while the Exner equation (equation 1.26) is a continuity equation that includes the impact of the presence of sediments.

The solid discharge is modeled with the formulation of Meyer-Peter and Müller (MPM). The model (through the Exner equation) uses the bed level z_b as a line, not as a moving transport layer. During the first comparisons, we will be satisfied if the simulated z_b lies between our experimental $z_{b,low}$ and $z_{b,up}$.

The mesh was made with the Gmsh software using a characteristic size of the cells of 0.015 m and a Manning coefficient of 0.165. The upstream and downstream boundaries were treated as transmissive boundaries.

The initial conditions are the same as the real experiment: a 10 cm bed on which 32.5cm of water rests.

We first compared numerical data with our experimental data. The comparisons are shown in figures 5.21 and 5.22 for time $t = 0.9s$.

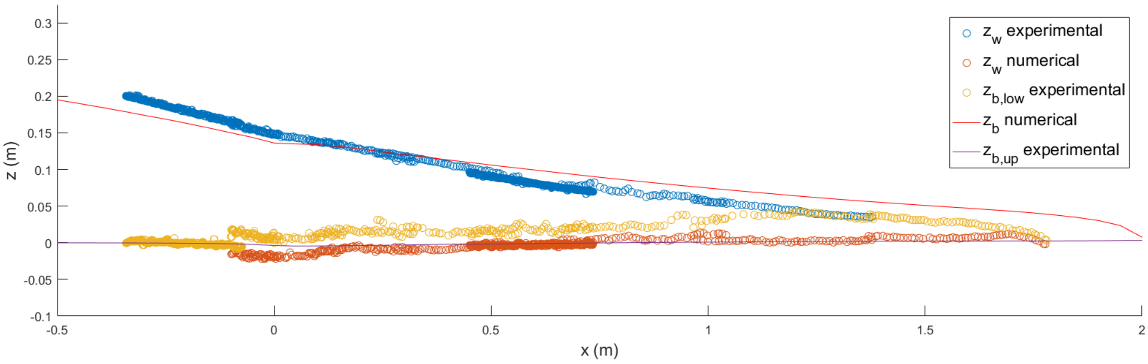

Figure 5.21: Comparison between experimental data z_w, $z_{b,low}$, $z_{b,up}$ and numerical data z_w and z_b as a function of x at time $t = 0.9s$

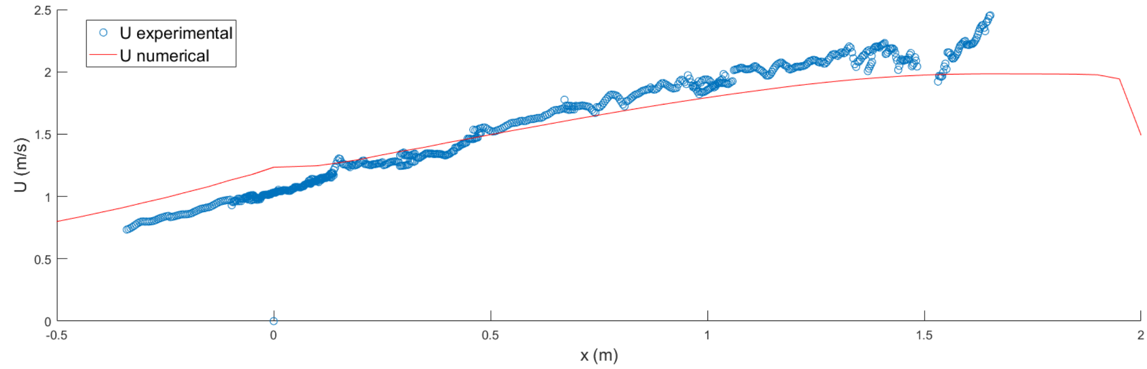

Figure 5.22: Comparison of average velocity U between experimental data and numerical data as a function of x at time $t = 0.9s$

These results are not satisfactory at first sight because it seems that there is a temporal shift between the numerical results and the experimental data. Indeed, if we look at the wavefront, we can observe a 20 centimeters horizontal shift and, for the velocity, the two parts of the comparison are not really superimposed.

Indeed, it is possible that there is a delay between the experimental data and the numerical results that can be explained by the "almost instantaneous triggering" device that links the beginning of the shooting, to the descent of the gate. As we saw in section 3, this delay is not caused by the time the door disappears, because we saw that it can be considered instantaneous.

Then we decided to compare the experimental data with numerical ones but this time, with different temporal shifts (-0.25s, -0.20s, -0.15s, -0.10s, -0.05s and -0.00s) for different times in order to determine the correct time shift, hoping that it would be the same over time.

We chose three criteria to determine the best shift:

- the Root Mean Square Error (RMSE) of the velocities:

$$RMSE_U = \sqrt{\overline{(U - U_{num})^2}} \tag{5.30}$$

  where U is the experimental average velocity and U_{num} the simulated average velocity.

- the Root Mean Square Error (RMSE) of the water levels:

$$RMSE_{z_w} = \sqrt{\overline{(z_w - z_{w,num})^2}} \tag{5.31}$$

  where z_w is the experimental water level and $z_{w,num}$ the simulated water level.

- The wavefront position deviation $|x - x_{num}|$

The results are summarized in the following tables.

t	$t_{num} = t - 0.25$	$t_{num} = t - 0.2$	$t_{num} = t - 0.15$	$t_{num} = t - 0.1$	$t_{num} = t - 0.05$	$t_{num} = t$
0.7	0.1255	0.0981	**0.0893**	0.0956	0.1099	0.1266
0.9	0.1155	0.0974	**0.0887**	0.0892	0.0966	0.1081
1.1	0.4513	0.1253	**0.0856**	0.0876	0.0944	0.1041
1.3	0.0995	0.0871	0.0775	0.0714	**0.0691**	0.0706

Table 5.4: Root Mean Square Error (RMSE) of the velocities $RMSE_U$

t	$t_{num} = t - 0.25$	$t_{num} = t - 0.2$	$t_{num} = t - 0.15$	$t_{num} = t - 0.1$	$t_{num} = t - 0.05$	$t_{num} = t$
0.7	0.0128	**0.0120**	0.0128	0.0148	0.0176	0.0209
0.9	0.0119	**0.0105**	0.0106	0.0118	0.0140	0.0169
1.1	0.0012	0.0091	**0.0082**	0.0086	0.0107	0.0129
1.3	0.0059	**0.0052**	0.0055	0.0066	0.008	0.0094

Table 5.5: Root Mean Square Error (RMSE) of the water levels $RMSE_{z_w}$

t	$t_{num} = t - 0.25$	$t_{num} = t - 0.2$	$t_{num} = t - 0.15$	$t_{num} = t - 0.1$	$t_{num} = t - 0.05$	$t_{num} = t$
0.7	0.19	0.04	**0.01**	0.06	0.26	0.36
0.9	0.18	0.08	**0.02**	0.12	0.17	0.22
1.1	0.175	0.125	**0.025**	0.125	0.225	0.325

Table 5.6: Wavefront position deviation $|x - x_{num}|$
Note that we don't see the front at t = 1.3s and t = 1.5s

We have bolded out the minimum values for the three criteria. Even if a time shift of -0.2s gives better (but very close to -0.15s) comparisons for the water levels z_w, we decide to keep -0.15s as it is the best in the two other criteria and the second best in the z_w criterion. Such an analysis shows us that the experimental data at time t match with the numerical results at time $t_{num} = t - 0.15s$ (for example, if $t = 0.9s$, $t_{num} = 0.75s$). It's necessary to keep in mind that this delay is not really important in our methods to find S_f, it is just interesting to have a better match in order to compare things that are comparable.

After finding the best shift, we can apply it on the numerical data to compare them with the experimental data. As presented in figures 5.23 and 5.24, the experimental results are very close to the numerical ones what is reassuring regarding the execution and measurement of our experiment.

Now we can calculate the different S_f thanks to numerical data and compare them with the experimental S_f previously found.

Regarding figure 5.25, we clearly see that all S_f have the same shape and the same order of magnitude as $S_{f,Manning}$ (except $S_{f,CH}$ next to the gate $x = 0$ due to irregularities of second and third derivatives).

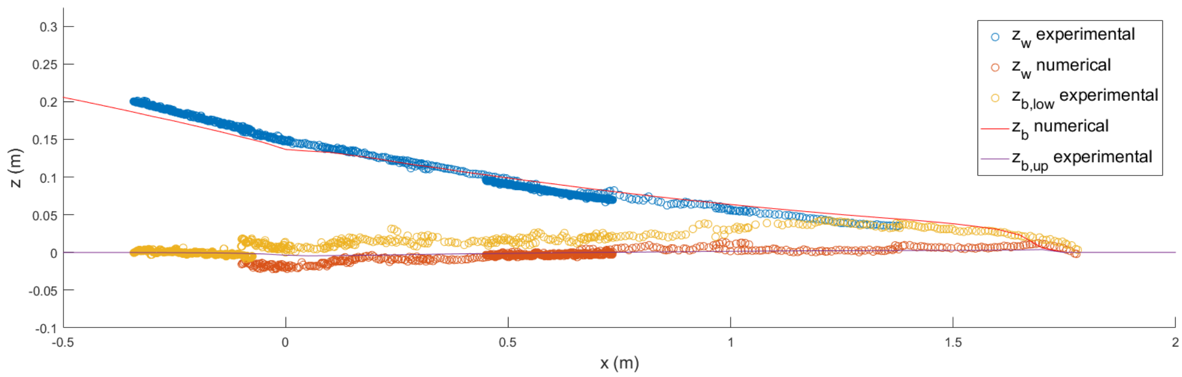

Figure 5.23: Comparison between experimental data z_w, $z_{b,low}$, $z_{b,up}$ at time $t = 0.9s$ and numerical data z_w and z_b at time $t = 0.9 - 0.15 = 0.75s$

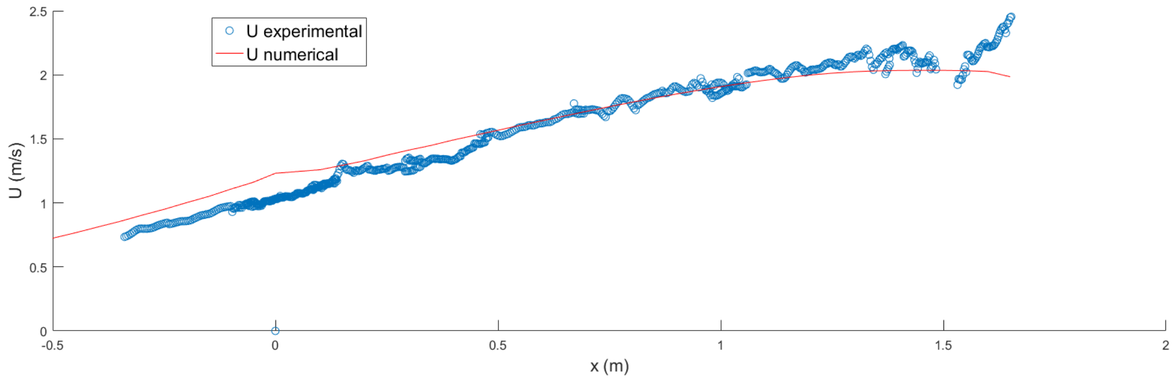

Figure 5.24: Comparison of average velocity U between experimental data at time $t = 0.9s$ and numerical data $t = 0.9 - 0.15 = 0.75s$ as a function of x

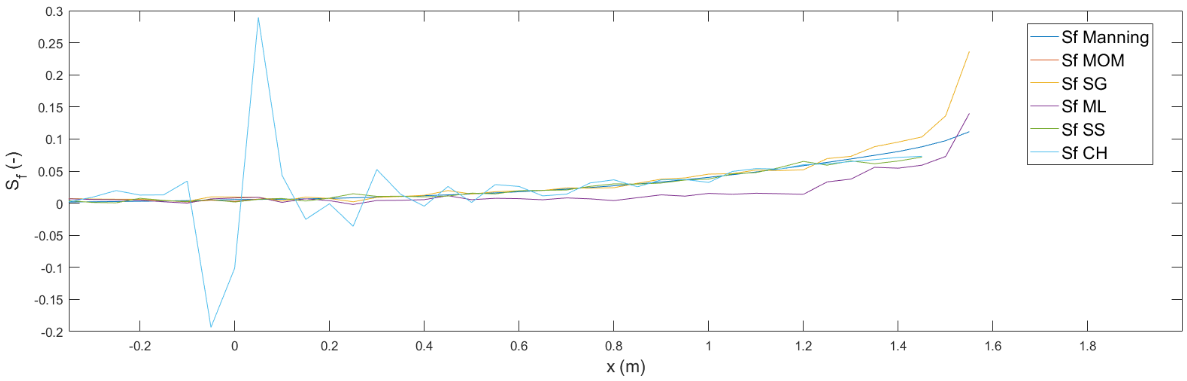

Figure 5.25: Numerical S_f $(t = 0.75s)$ as a function of x

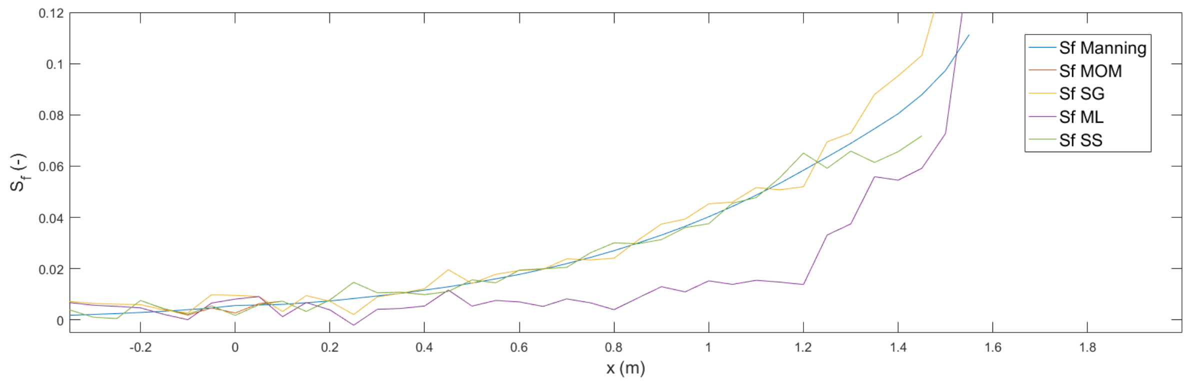

Figure 5.26: Closer look at the numerical S_f $(t = 0.75s)$ as a function of x (removing deliberately $S_{f,CH}$)

If we take a closer look at the numerical S_f values (cf. figure 5.26), we can see that this is not an effect of the scale: the $S_{f,SG}$, $S_{f,SS}$ and $S_{f,MOM}$ (which follows $S_{f,SS}$) curves really stick to the $S_{f,Manning}$ curve by oscillating slightly around it. Note that it is also the case of $S_{f,CH}$ which we have removed here because of the big oscillations around the position of the gate.
This similarity between the curves in the numerical analysis proves us that, in the experimental S_f analysis (figure 5.19), the irregularities of the different S_f around $S_{f,Manning}$ are actually due to experimental errors and that in reality, the different experimental ways to find S_f give similar values to $S_{f,Manning}$.

The conclusion we make is that it seems to be a good approximation to take the experimental value $S_{f,Manning}$ in order to calculate $\tau_b = \gamma R S_{f,Manning}$, and it's what we finally do in our calculations.

5.4.5 Final results of the Slope method

Now, we have everything to be able to calculate $\tau_b = \gamma R S_f$. As can be seen in table 5.7 we found values of the shear stress τ_b between 4.89 and 31.144 Pa.

x(m)	**t(s)**	$\mathbf{z_w}$**(m)**	$\mathbf{z_{b,up}}$**(m)**	$\mathbf{z_{b,low}}$**(m)**	$\mathbf{\Delta z}$**(m)**	$\mathbf{u_*}$**(m/s)**	**Br(-)**	θ**(-)**	**r(-)**	τ_b**(Pa)**
0.0	0.7	0.1517	0.0032	-0.0194	0.0105	0.070	11.6	0.172	0.839	**4.89**
	0.9	0.1483	0.0032	-0.0178	0.007	0.073	10.7	0.190	0.826	5.39
	1.1	0.1444	-0.0007	-0.0191	0.010	0.0729	10.85	0.187	1.016	5.308
	1.3	0.1455	0.0073	-0.0168	0.009	0.074	10.45	0.191	**0.753**	5.429
0.2	0.7	0.1162	0.0197	-0.0086	0.0125	0.090	11.65	0.285	0.886	8.08
	0.9	0.1271	0.0152	-0.0054	0.010	0.084	12.2	0.247	0.923	6.999
	1.1	0.1331	0.0118	-0.0106	0.015	0.081	11.2	0.234	1.209	6.635
	1.3	0.1350	0.0155	-0.0091	0.0132	0.080	11.5	0.226	0.921	6.415
0.5	0.7	0.0751	0.0212	-0.0011	-0.006	0.141	7.1	0.071	0.775	19.889
	0.9	0.0896	0.0182	-0.0061	0.006	0.119	8.00	0.495	0.917	14.058
	1.1	0.1042	0.0120	-0.0044	0.007	0.107	9.7	0.404	**1.254**	11.458
	1.3	0.1131	0.0084	-0.0099	0.0093	0.096	8.8	0.327	1.192	9.28
1.0	0.7	-	-	-	-	-	-	-	-	-
	0.9	0.0557	0.0237	0.0017	0.0045	0.165	27.266	0.961	0.771	27.266
	1.1	0.0742	0.0199	0.0032	0.0045	0.136	8.87	0.655	1.118	18.601
	1.3	0.0879	0.0212	-0.0009	0.0074	0.124	8.2	0.543	1.031	15.404
1.5	0.7	-	-	-	-	-	-	-	-	-
	0.9	-	-	-	-	-	-	-	-	-
	1.1	0.0518	0.0227	0.0007	0.010	0.176	7.95	1.097	0.847	**31.144**
	1.3	0.0662	0.0227	-0.0014	0.0115	0.15	8.2	0.798	0.860	22.64

Table 5.7: Evolution of the variables needed in the velocity distribution study and determination of r and τ_b - The empty cells correspond to times and spaces where the flow is not yet present or very next to the front (The relative graphs for each position are shown on Appendix E)

Once we have τ_b, we can find $u_* = \sqrt{\tau_b/\rho}$ and then, by fitting the experimental velocity profile with the theoretical one (as shown in figure 5.27 at gate position $x = 0$ for times 0.7s, 0.9s, 1.1s and 1.3s) we can find the corresponding Δz and B_r.

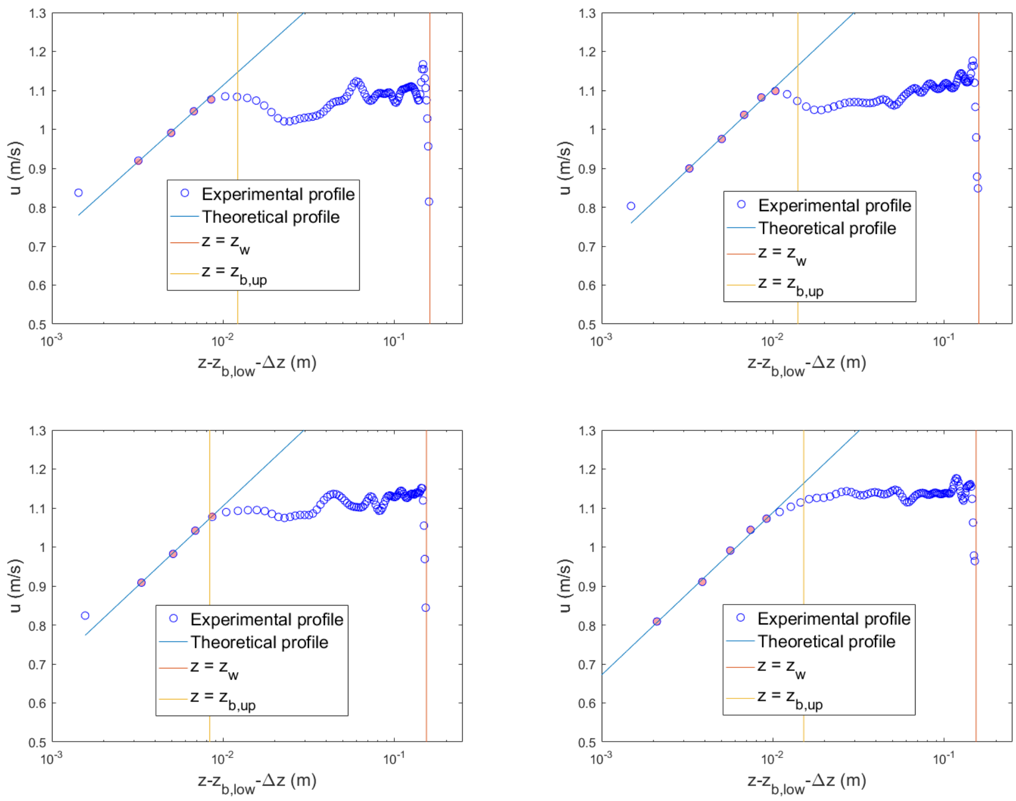

Figure 5.27: Theoretical velocity profiles fitted on the experimental ones for times t = 0.7s (on the top left), t = 0.9s (on the top right), t = 1.1s (on the lower left) and t = 1.3s (on the lower right) at the gate's position x = 0 m

The different parameters found for all these times at positions $x = 0.0,\ 0.2,\ 0.5,\ 1.0$ and $1.5m$ are shown in table 5.7.

The previously defined ratio r is found to be between 0.753 and 1.254. It shows that the end of the logarithmic portion of the velocity profile is every time relatively near to the position of $z_{b,up}$ $(1 \pm 25\%)$ which corresponds to the upper limit of the sheet-flow layer. This discovery could be interesting in the case it is confirmed because it could more easily lead to the position of the last point of the logarithmic profile for other experiments.

In order to compare some of the results of the Slope method to the starting step of the application of the Clauser method in section 5.2, we added the couples Δz and $\theta(u_*)$ obtained with the slope method on the graph $(\frac{\Delta z}{d_{50}} - \theta)$ proposed by Sumer et al. (1996) in figure 5.28.

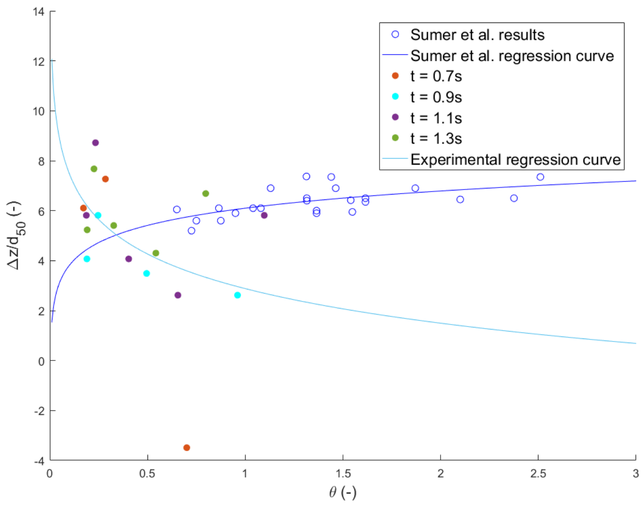

Figure 5.28: Experimental level of the theoretical bed Δz as a function of θ + Results of Sumer et al. (1996) figure 5.6

We can see that the couples $\frac{\Delta z}{d_{50}} - \theta$ we found with the slope method do not really have the same trend as the couples found by Sumer et al. The trend seems rather be the opposite and we found, for our experiments, the logarithmic regression equation:

$$\frac{\Delta z}{d_{50}} = -1.998 \ln(\theta) + 2.8804 \tag{5.32}$$

The fact that the trend is opposite to the Sumer et al.'s ones is not necessarily shocking, given that the experimental flow is not the same. This result (equation 5.32) could be specific to the dam-break flow.

The Slope method we have explained in this section is, for us, the most interesting and the most stand-alone one as we are not influenced by previous results found by other authors (in contrast with the Clauser method explained in section 5.2). Moreover, our final results are coherent with those found by Ilaria Fent who used an other method.

Conclusion

The quest to determine the shear stress in a flow following a dam failure is not over, but it made some progress.

We reanalyzed the results of our predecessors. We explored new ideas. Some of them were left open such as the Clauser method with parametric optimization, others were eliminated such as the Slope method using a friction slope based on the total head ($\mathcal{H}$) definition ($S_{f,unsteady}$).

The two methods that gave concrete results are the Clauser method using the $\Delta z - u_*$ relation proposed by Sumer et al. and the Slope method.
The Clauser method uses the vertical profile $u(z)$ while the Slope method uses the longitudinal profile of the average velocity $U(x)$. The fact that these two different methods give similar results is comforting.
The conclusions of the use of the Slope method were improved after the use of a numerical simulation free of experimental errors.

The final shear stress values τ_b that we found by using the Clauser method ($\tau b = [2.025 \;\; 32.4] Pa$) and the Slope method ($\tau b = [4.89 \;\; 31.144] Pa$) have both the same order of magnitude that the values found by Ilaria Fent in her thesis ($\tau b = [5 \;\; 15] Pa$). That similitude between these three sets of final values, using different calculation ways, led us to believe that our analysis is on the good way.

Moreover we found with each method that the theoretical velocity profile is every time relatively near to the position of $z_{b,up}$ ($\pm 25\%$) that corresponds to the upper limit of the sheet-flow layer.

The slope method seems to be the best option if it is valid but for now it needs to be confirmed by an additional approach to prove the validity of these results. If so, it could prove that calculating the friction slope with a typical Manning equation would give quick and satisfying results. We show that the reason why our predecessors eliminated this Manning option can be challenged, so the hope

remains.
In our view, this confirmation could be played out in the use of the Clauser method with parametric optimization, even if it was not convincing in our work. Among other things, we propose several ideas in this conclusion to make this method functional.

Here are some ideas that we suggest to our successors to exploit in their research.

- To make the parametric optimization work better, we recommend changing the eroded material.
  The choice of eroded material can be made from the Shields diagram. The aim is to take a material whose grains are lighter (smaller γ_s) in order to have a bigger sheet flow layer and to better determine the logarithmic portion of the profile because there will be more points to analyze.
  This could lead to a reduction of the sensitivity of u_* and Δz and make the calculation of the derivative $\frac{du}{dz}$ more accurate in a parametric optimization.
  Beside that, it could expand the database in order to better characterize the terms k_s and B_r that we put a bit aside, because they more than probably depend on the median sediment diameter d_{50}.

- Also in order to improve the parametric optimization, a lower bound for $z - z_{b,low} - \Delta z$ could be imposed so that the inside of the logarithm in the profile equation is never negative. This way, the differential formulation would not be necessary. Nevertheless, the values of k_s and B_r would have to be fixed.

- We no longer had access to the computer on which the software DaVis 8 (LaVision) was installed during the lockdown related to the coronavirus crisis, but it seems that there is a way to have more points of the velocity profile.
  If this is indeed possible, it would help for all the methods we use, especially for parametric optimization.

- We decided to work with the Manning coefficient related to the bed $n_b = 0.165 s/m^{1/3}$. Ilaria Fent experimentally found other values of the Manning coefficient that take into account turbulent and transient effects not present in experiments of Sumer et al. (1996) and Ferreira et al. (2012).
  We wanted to remain general and were not convinced by this approach but Ilaria Fent found it interesting before doing her numerical simulations.
  We would not bet on it, but this decision could be challenged.

- In order to use the slope method, we used the assumptions of a uniform flow and neglected the friction on the vertical walls. Ferreira et al. (2012)

suggested several methods made by other authors to improve the hydraulic radius value to consider the impact of the walls.

- Even if we were not convinced by it, the automatic detection of the water level z_w and the two bed levels $z_{b,up}$ and $z_{b,low}$ does exist and could be improved.

- We talked about the Reynolds Stress Method Method to find the bed shear stress τ_b but we did not use it. We were not satisfied by Ilaria Fent's method when she tried it but we saw that Ferreira et al. (2012) also used it so it might be worth trying this method again for confirmation as it gives values of τ in a very different way.

- When we tried the Clauser method using the $\Delta z - u_*$ relation proposed by Sumer et al. (section 5.2), and the Slope method (section 5.4), we decided to fix the bed roughness

$$k_s = d_{50} \tag{5.33}$$

  and then we modified the B_r term to find a good fitting.

  It is important to keep in mind, on the one hand, that there are other relations for k_s and that this value is maybe not correct and, on the other hand, that Sumer et al. (1996), for example, fixed the B_r term and modified the k_s term to find a good fitting.
  Our approach is not a problem for finding the shear velocity u_* and the shift Δz because these terms k_s and B_r compensate each other in the profile equation so their values do not impact the interesting result. It is as if we do not pay attention to the values of k_s and B_r. It means that they could be further studied.

References

Aleixo, R., Soares-Frazão, S. and Zech, Y. (2011). *Velocity-field measurements in a dam-break flow using a PTV Voronoï imaging technique.* Experiments in fluids, 50(6), 1633-1649

Aleixo, R. (2013). *Experimental study of the early stages of a dam-break flow over fixed and mobile beds.* PhD thesis, Université catholique de Louvain, Louvainla-Neuve

Beck, S. and Collins, R. (2008). *Moody Diagram.* University of Sheffield, Sheffield

Behets-Wydemans N. and Jacques F. (2016). *Mesures de profils de vitesses dans un écoulement transitoire (rupture de barrage) par imagerie digitale sur lit mobile.* Travail de fin d'études, UCL, Louvain-la-Neuve

Camacho, D. and Radelet, P. (2019). *Mesure du profil de vitesse dans un écoulement consécutif à une rupture de barrage sur lit de sédiment.* Master's thesis, UCL, Louvain-la-Neuve

Cao, Z. et al. (2004). *Computational dam-break hydraulics over erodible sediment bed.* Journal of Hydraulic Engineering, ASCEASCE, 130(7), 689–703

Castro-Orgaz, O. and Hager, W. H. (2013). *Unsteady Boussinesq-type flow equations for gradually-eroded beds: application to dike breaches.* Journal of Hydraulic Research, 51(2), 203-208

Coles, D. (1956). *The law of the wake in the turbulent boundary layer.* Journal of Fluid Mechanics, 1(2), 191-226

Fent, I. (2018). *Dam break over mobile bed : experimental and numerical study.* PhD thesis, UCL, Louvain-la-Neuve

Ferreira, R. M. L. et al. (2012). *Flow over rough mobile beds: Friction factor and vertical distribution of the longitudinal mean velocity.* Water Resources Research

Garcia, M.H. (2008). *Sediment transport and morphodynamics.* In M.H. Garcia ed., Sedimentation Engineering Processes, Measurements, Modeling and Practice. ASCE Manuals and Reports on Engineering Practice, ASCE, (Reston), VA, 110, 21–163.

Gunt (2018). *Flow conditions from left to right: laminar flow, transition from laminar to turbulent flow, turbulent flow.* 09/04/2020. https://www.gunt.de/images/datasheet/548/HM-150.01-Pertes-de-charge-linaires-en-coulement-laminaire–turbulent-gunt-548-pdf1fr-FR.pdf

Graf, W. H. and Altinakar, M. S. (1998). *Fluvial hydraulics.* Wiley

Keulegan G.H. (1938). *Laws of turbulent flow in open channels (Vol. 21, pp. 707-741).* US: National Bureau of Standards

Nikuradse, J. (1933). *Laws of flow in rough pipes.* In VDI Forschungsheft

Qu, Z. (2003). *Unsteady open-channel flow over a mobile bed.* Doctoral dissertation No. 2688, Laboratoire de Recherches Hydrauliques, Ecole Polytechnique Fédérale, Lausanne, Switzerland

Rathore, V. et al. (2019). *Computation of bed shear stress from velocity measurements in a gradually varying roughness bed.* IAHR World Congress

Ritter, A. (1892). *Die fortpflanzung der wasserwellen.* Zeitschrift Verein Deutscher Ingenieure, 36, 947–954

Savage, S. B. and Hutter, K. (1989). *The motion of a finite mass of granular material* down a rough incline. Journal of Fluid Mechanics, 199, 177–215

Soares-Frazão, S. (2018). *LGCIV2051 - Applied hydraulics open-channel flows*

Soares-Frazão, S. (2018). *LGCIV2053 - Hydraulique Fluviale*

Soares-Frazão, S. (2018). *LGCIV2054 - Numerical simulation of transient flows*

Song, T. and Graf, W. H. (1996). *Velocity and turbulence distribution in unsteady open-channel flow.* Journal of Hydraulic Engineering, 122(3), 141–154

Spinewine, B. and Capart, H. (2013). *Intense bed-load due to a sudden dambreak.* Journal of Fluid Mechanics, 731, 579–614

Sumer B. M. et al. (1996). *Velocity and concentration profiles in sheet-flow in movable bed.* Journal of Hydraulic Engineering (Reston), 122(10), 549-558

Tu, H. (1991). *Velocity distribution in unsteady flow over gravel beds.* Ph.D. Thesis, No 911, Ecole Polytechnique Fédérale (EPFL), Lausanne, Switzerland

Tu, H. and Graf W. H. (1992). *Velocity distribution in unsteady open channel flow over gravel beds.* Journal of Hydroscience and Hydraulic Engineering, 10(1), 11-25

Vandenhoeck, A. (2015). *Product-Manual Flowmaster.* Göttingen, Allemagne

Zech, Y., Soares-Frazão, S., Spinewine, B., Savary, C. and Goutière, L. (2009). *Inertia effects in bed-load transport models.* This paper is one of a selection of papers in this Special Issue in honour of Professor M. Selim Yalin (1925-2007). Canadian Journal of Civil Engineering

Appendices

Appendix A

Experimental steps

This checklist comes directly from the Master's thesis of Donifan Camacho and Pauline Radelet. We conserved the original French-language version of this checklist in order to facilitate the understanding for our successors.

1. Allumer le compresseur (toujours s'assurer que la pression se trouve à 8 bars avant le début d'un essai, pour assurer une même vitesse de descente à la porte lorsque l'expérience est recommencée).

2. Préparer la solution avec le traceur:

   - 1 petite dose de savon liquide
   - 1 bouchon de pliolite
   - Remplir d'eau le reste d'une bouteille de 1,5L

3. Placer le tamis dans le bac aval pour éviter que les sédiments érodés ne finissent tous dans l'eau que nous récupérons dans le bac, ou le nettoyer si une expérience vient d'être faite.

4. Mettre le trépied de la caméra rapide à niveau par rapport au sol, et entourer à la craie l'emplacement exact de ses pieds, au cas où la caméra devrait être bougée par la suite, ou si celle-ci a accidentellement changé de position.

5. Préparer la caméra rapide et l'ordinateur (Branchement des câbles, lancement du programme d'enregistrement PFV Fastcam, mettre l'objectif, faire le focus caméra).

6. Placer le laser au-dessus de la zone qui nous intéresse dans le canal bleu.

7. Faire la calibration. Pour ce faire, il faut placer la plaque de calibration de type 31 et s'assurer que le plan de celle-ci soit premièrement en phase avec la feuille laser et deuxièmement mis à niveau par rapport au sol en utilisant un niveau à bulle. Il faut ensuite placer 2 portes que nous avons fabriquées et rendues au maximum étanches autour de la plaque pour compartimenter la zone d'enregistrement et pouvoir l'immerger dans l'eau. Une fois que le niveau de l'eau dépasse le dessus de la plaque de calibration, nous pouvons enregistrer des images qui serviront à la calibration en éclairant au mieux la plaque à l'aide d'une lampe.

8. Tasser et compacter les sédiments le plus régulièrement possible à l'aide d'une masse.

9. Saturer les sédiments à l'aval de la porte en utilisant un jet d'eau léger

10. Remplir le réservoir amont du canal bleu avec de l'eau en utilisant un tube percé pour éviter de trop remuer les sédiments tassés avec un jet d'eau trop puissant. Si une expérience a déjà été réalisée dans la journée et que le bac à l'aval est rempli d'eau, nous pouvons réutiliser cette eau au moyen d'une pompe vide-cave.

11. Verser la solution avec le traceur dans le réservoir amont et touiller.

12. Activer le trigger sur le programme PFV Fastcam

13. Éteindre les lumières, placer une boîte en carton sur l'automate pour cacher la lumière émise par ses boutons, placer un voile sur l'écran de l'ordinateur pour aussi cacher la lumière qu'il émet, allumer le laser.

14. Lancer la descente de la porte.

15. Enregistrer les images en .bmp! (Attention dernière étape et non la moindre, car enregistrer les images en un autre format compresserait les données, et rendrait inutilisable ces images dans le programme DaVis, il faut alors recommencer toute l'expérience...)

Appendix B

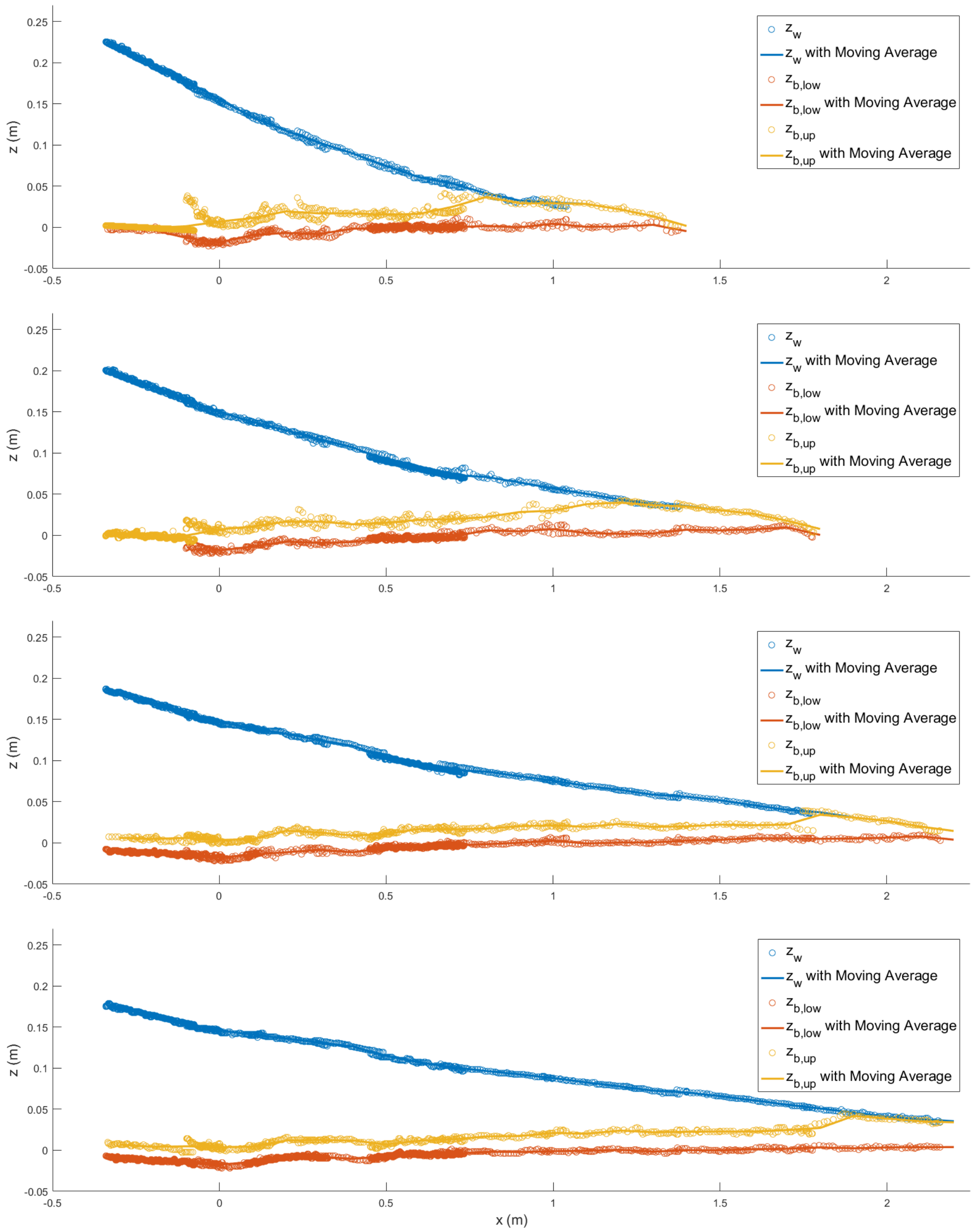

Figure 5.29: Experimental data z_w, $z_{b,low}$, $z_{b,up}$ and their moving average as a function of x at time $t = 0.7s$, $0.9s$, $1.1s$ and $1.3s$ in this order

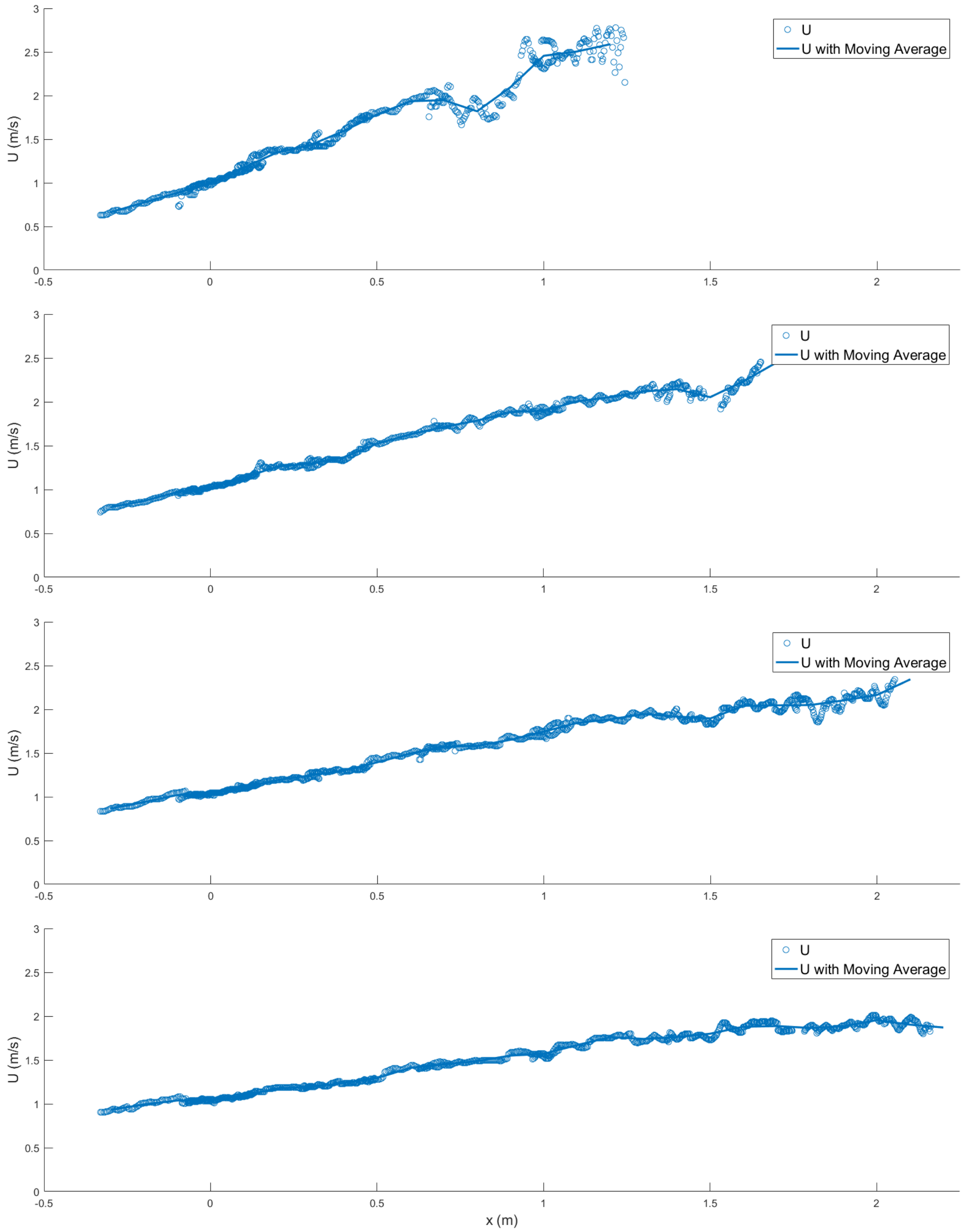

Figure 5.30: Experimental data U and its moving average as a function of x at time $t = 0.7s$, $0.9s$, $1.1s$ and $1.3s$ in this order

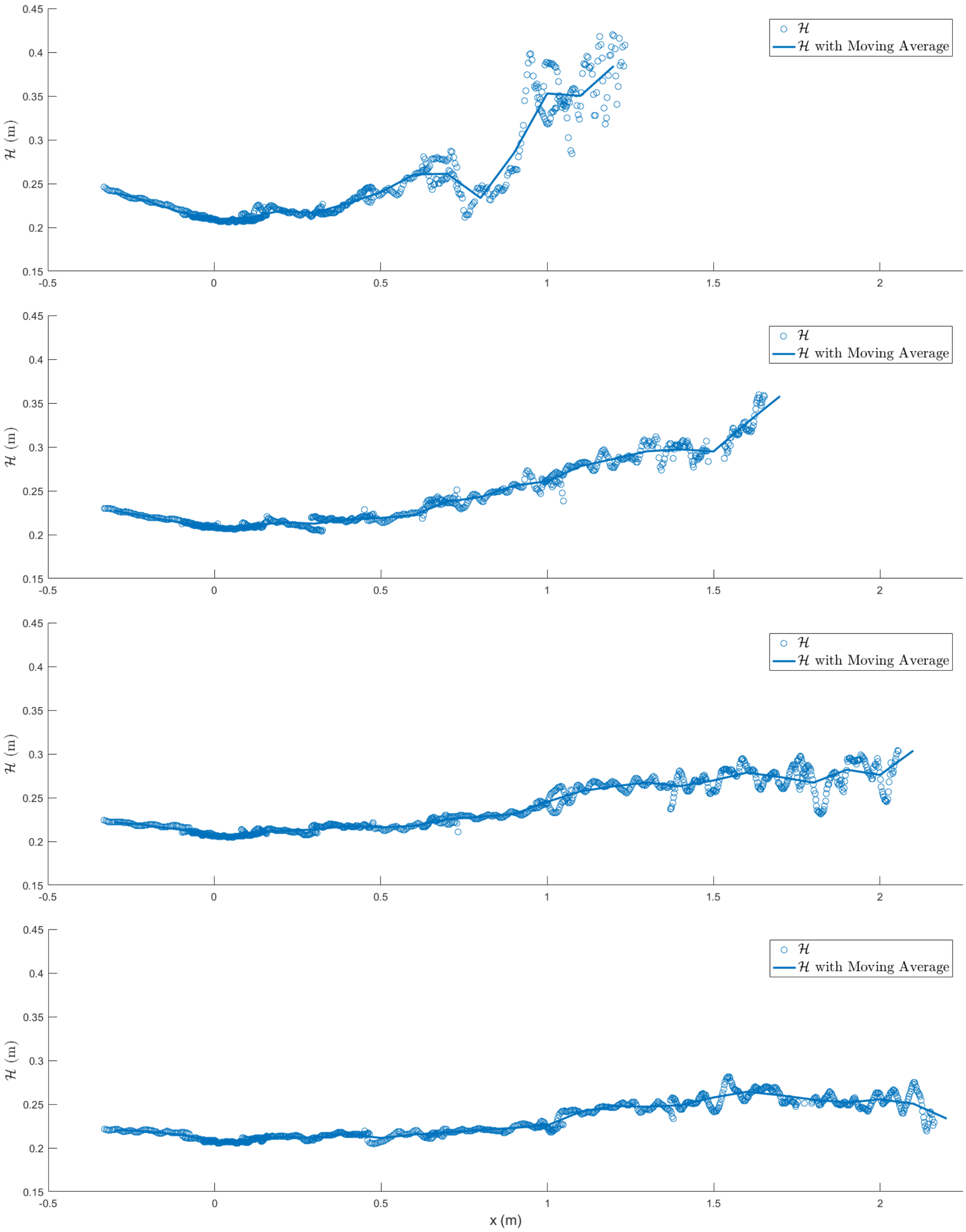

Figure 5.31: Experimental data $\mathcal{H}$ and its moving average as a function of x at time $t = 0.7s$, $0.9s$, $1.1s$ and $1.3s$ in this order

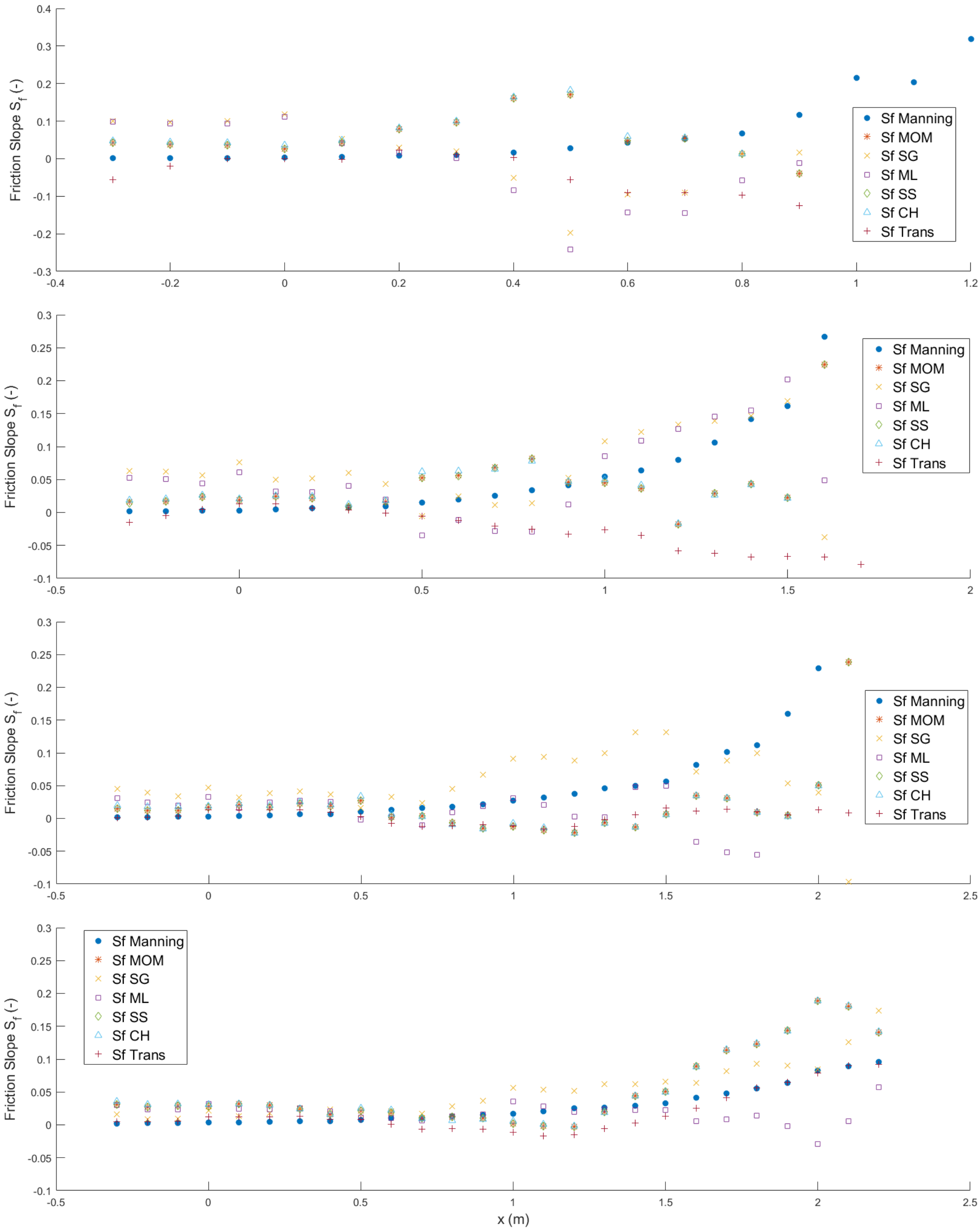

Figure 5.32: Experimental data S_f and its moving average as a function of x at time $t = 0.7s$, $0.9s$, $1.1s$ and $1.3s$ in this order

Appendix C

Clauser method fittings

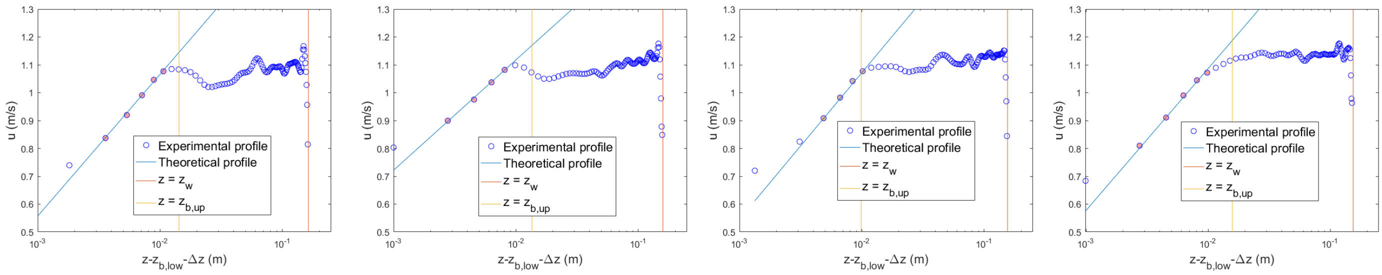

Figure 5.33: Theoretical velocity profiles fitted on the experimental ones for times $t = 0.7s$, $0.9s$, $1.1s$ and $1.3s$ (from left to right) at position $x = 0m$

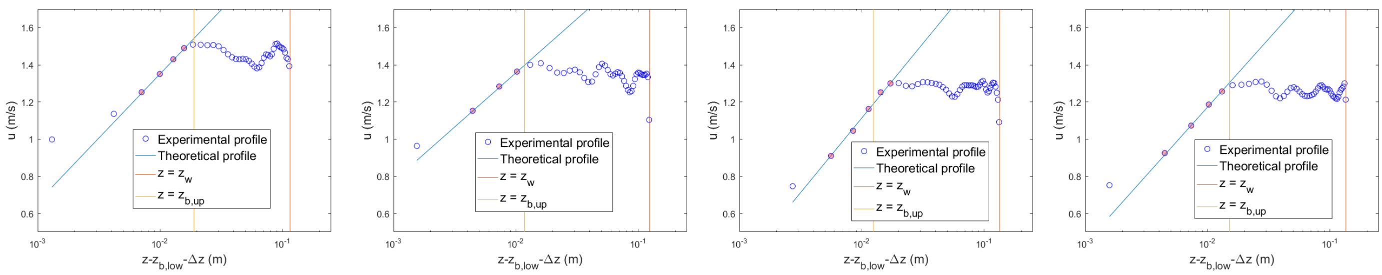

Figure 5.34: Theoretical velocity profiles fitted on the experimental ones for times $t = 0.7s$, $0.9s$, $1.1s$ and $1.3s$ (from left to right) at position $x = 0.2m$

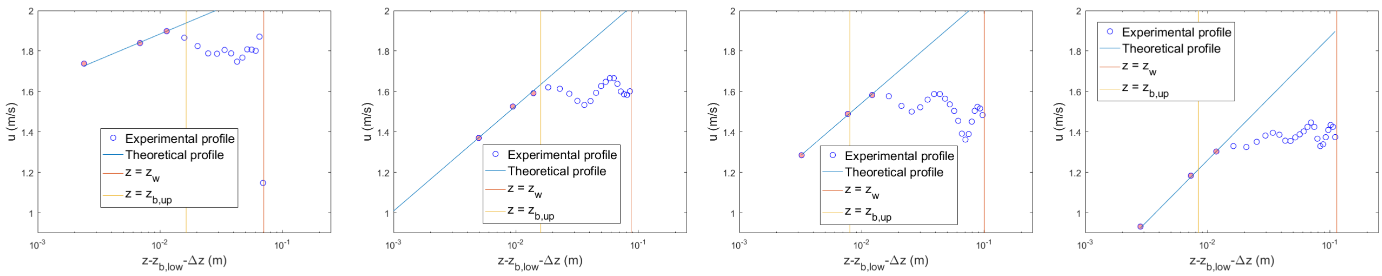

Figure 5.35: Theoretical velocity profiles fitted on the experimental ones for times $t = 0.7s$, $0.9s$, $1.1s$ and $1.3s$ (from left to right) at position $x = 0.5m$

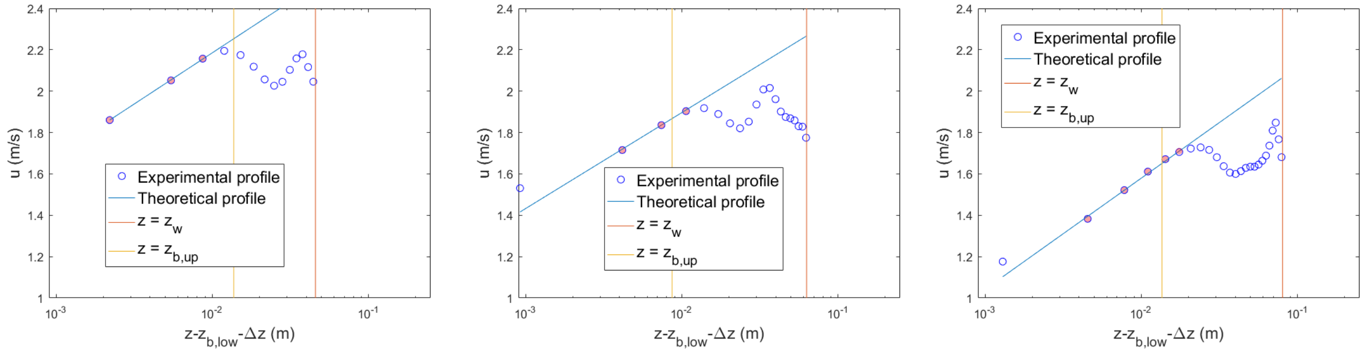

Figure 5.36: Theoretical velocity profiles fitted on the experimental ones for times $t = 0.9s$, $1.1s$ and $1.3s$ (from left to right) at position $x = 1.0m$ Velocity at time $t = 0.7$ at that position is very next to the wave front thus DaVis8 couldn't give interesting data

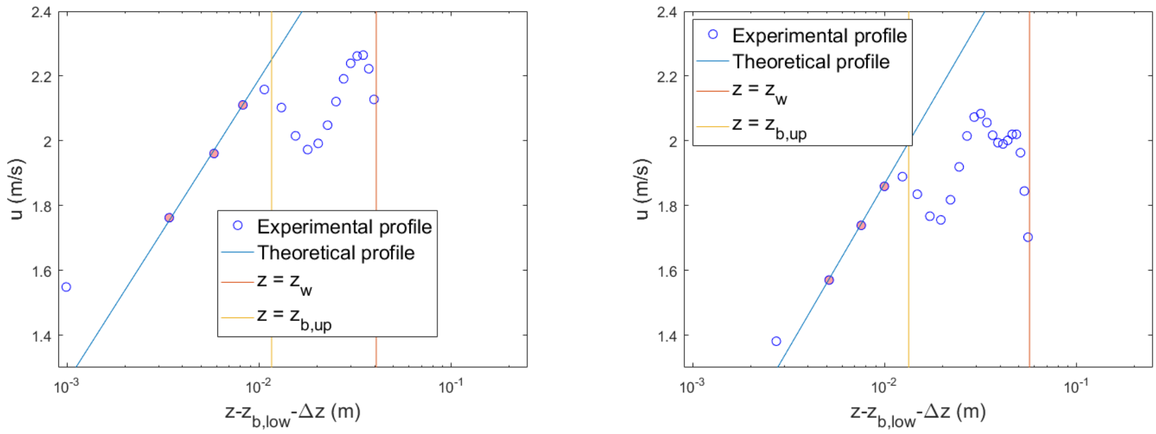

Figure 5.37: Theoretical velocity profiles fitted on the experimental ones for times $t = 1.1s$ and $1.3s$ (from left to right) at position $x = 1.0m$ Velocity at time $t = 0.7$ and $0.9s$ at that position is very next to the wave front thus DaVis8 couldn't give interesting data

Appendix D

Clauser method fittings with parametric optimization

The figures on the left are the experimental velocity profiles. The figures on the right are the derivatives found by parametric optimization.

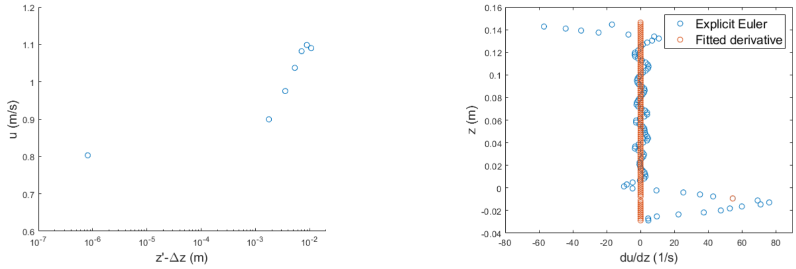

Figure 5.38: Using 8 points and the Explicit Euler derivative.

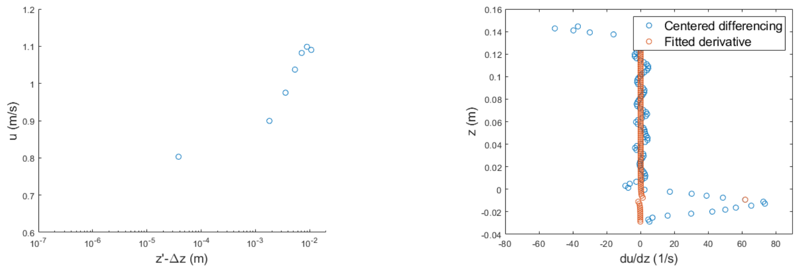

Figure 5.39: Using 8 points and the Center differencing derivative.

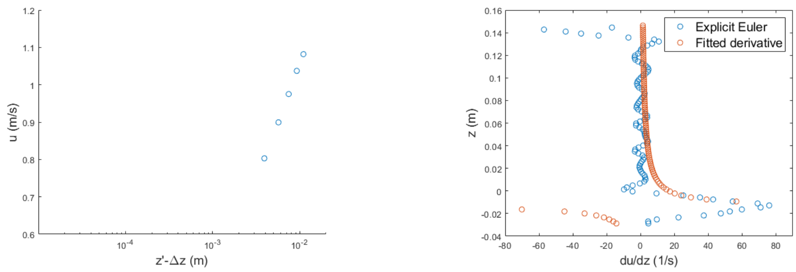

Figure 5.40: Using 5 points and the Explicit Euler derivative.

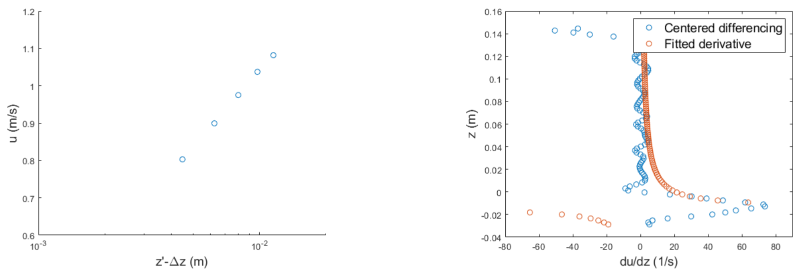

Figure 5.41: Using 5 points and the Center differencing derivative.

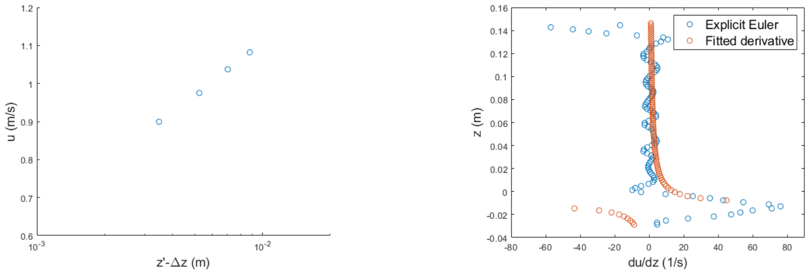

Figure 5.42: Using 4 points and the Explicit Euler derivative.

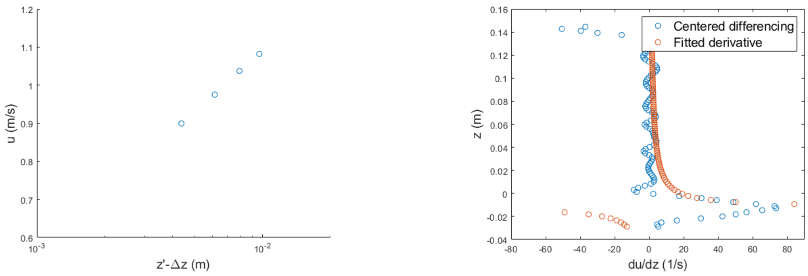

Figure 5.43: Using 4 points and the Center differencing derivative.

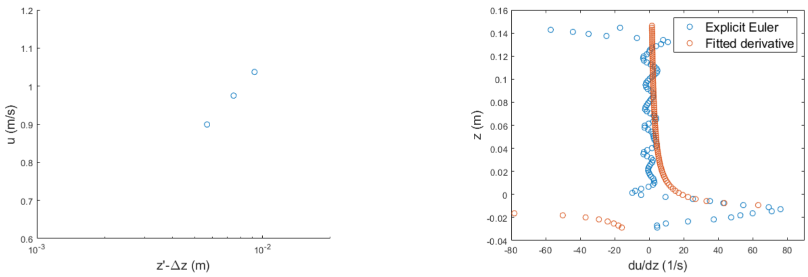

Figure 5.44: Using 3 points and the Explicit Euler derivative.

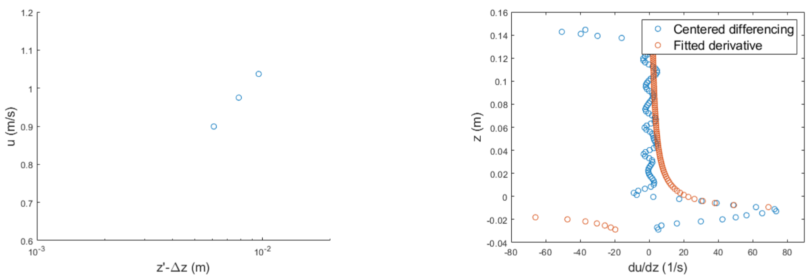

Figure 5.45: Using 3 points and the Center differencing derivative.

Appendix E

Slope method fittings

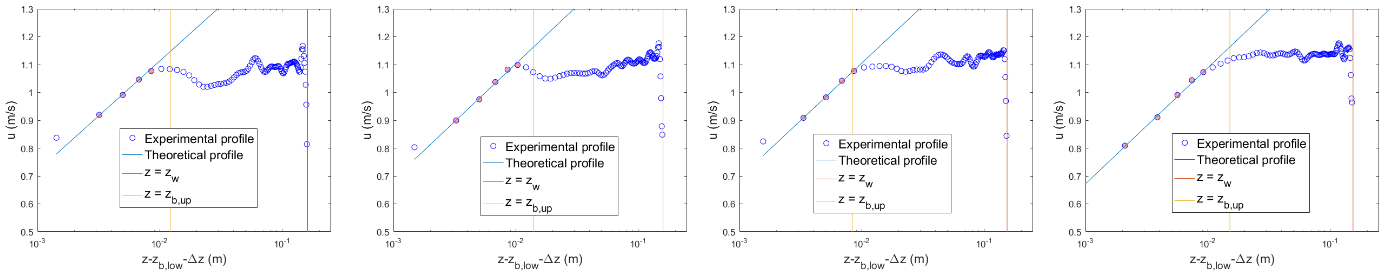

Figure 5.46: Theoretical velocity profiles fitted on the experimental ones for times $t = 0.7s$, $0.9s$, $1.1s$ and $1.3s$ (from left to right) at position $x = 0m$

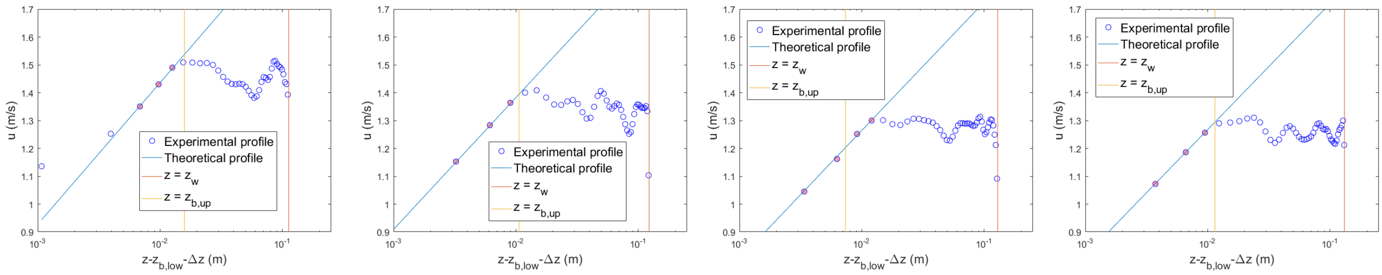

Figure 5.47: Theoretical velocity profiles fitted on the experimental ones for times $t = 0.7s$, $0.9s$, $1.1s$ and $1.3s$ (from left to right) at position $x = 0.2m$

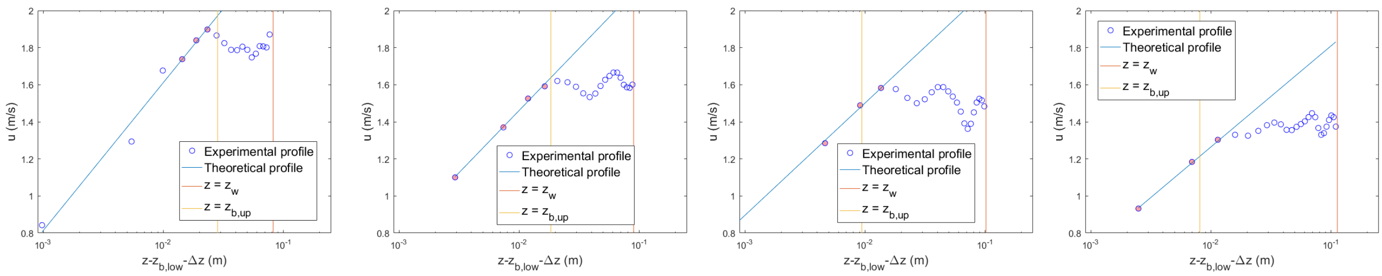

Figure 5.48: Theoretical velocity profiles fitted on the experimental ones for times $t = 0.7s$, $0.9s$, $1.1s$ and $1.3s$ (from left to right) at position $x = 0.5m$

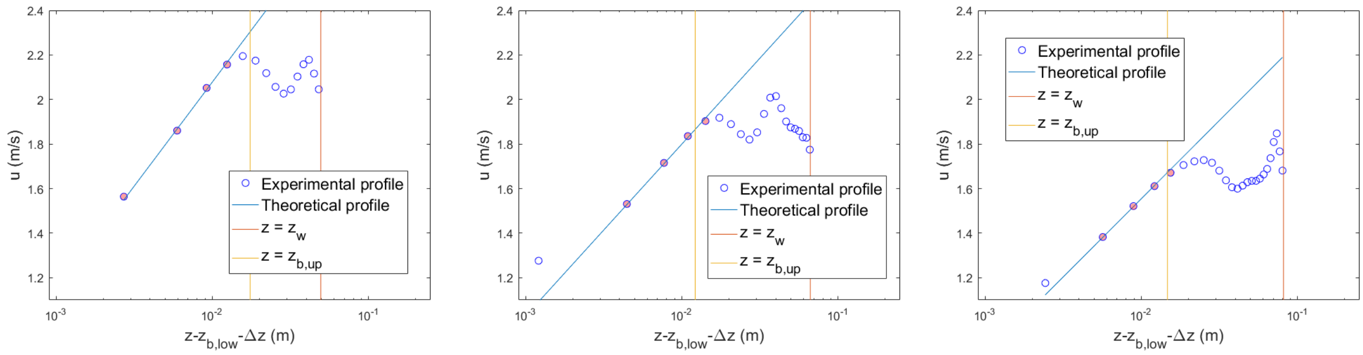

Figure 5.49: Theoretical velocity profiles fitted on the experimental ones for times $t = 0.9s$, $1.1s$ and $1.3s$ (from left to right) at position $x = 1.0m$ Velocity at time $t = 0.7$ at that position is very next to the wave front thus DaVis8 couldn't give interesting data

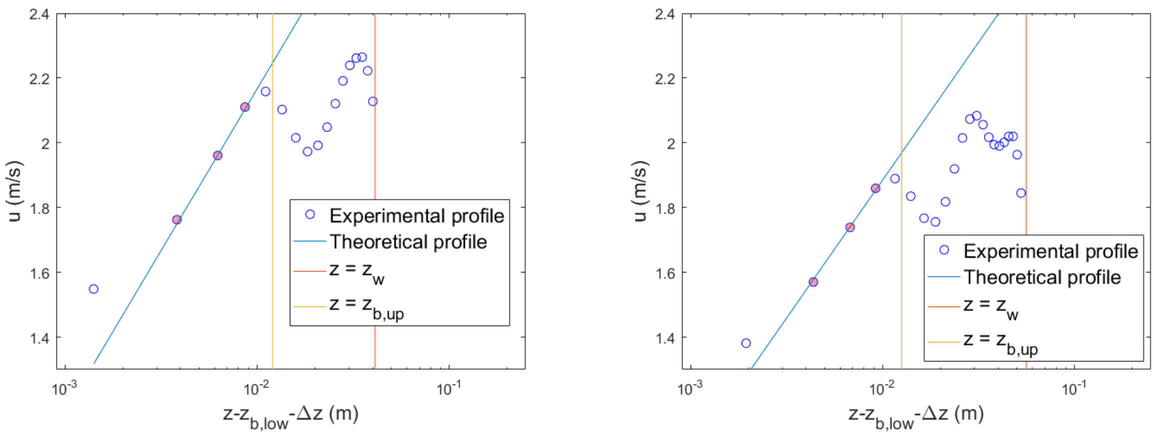

Figure 5.50: Theoretical velocity profiles fitted on the experimental ones for times $t = 1.1s$ and $1.3s$ (from left to right) at position $x = 1.0m$ Velocity at time $t = 0.7$ and $0.9s$ at that position is very next to the wave front thus DaVis8 couldn't give interesting data

Appendix F

Digital appendix

Here is enumerated a list of the documents that we transmit in our digital appendix:

- A folder with with the records of our 2 personal experiments
- Folders with all the records of Ilaria Fent that we used for our analyses and the all the records of Donifan Camacho-Fernandes and Pauline Radelet
- The Powerpoint presentations from our weekly meetings
- The Master's thesis (.pdf file)
- Excel sheets of the data base we made to analyse our experiments:
  - DataBaseOfficial.xlsx
  - FittingU.xlsx
- Matlab codes:
  - exe_SfCalc_Canal.m
  - exe_SfCalc_Ritter.m
  - exe_SfCalc_Simu.m
  - exe_fitdudz.m
  - exe_Profile_extraction_2020.m
  - exe_Profile_extraction.m
  - Other functions that are used within those we have just mentioned.
- The files provided by Robin Meurice to run the numerical simulations
  - A quick-run guide (.docx)
  - The SVE2DBF model
  - A version of MinGW (to use with Code::Blocks)
  - The results of several simulations

UNIVERSITÉ CATHOLIQUE DE LOUVAIN
École polytechnique de Louvain
Rue Archimède, 1 bte L6.11.01, 1348 Louvain-la-Neuve, Belgique | **www.uclouvain.be/epl**